Numerical investigations of heat and mass transport in fractured porous rock masses

Dissertation
zur
Erlangung des Doktorgrades (Dr. rer. nat.)
der
Mathematisch-Naturwissenschaftlichen Fakultät
der
Rheinischen Friedrich-Wilhelms-Universität Bonn

vorgelegt von
Sahar Hamidi
aus
Teheran, Iran

Bonn 2017

Angefertigt mit Genehmigung
der
Mathematisch-Naturwissenschaftlichen Fakultät
der
Rheinischen Friedrich-Wilhelms-Universität Bonn

1. Gutachter: Prof. Dr. Stephen A. Miller
2. Gutachter: Prof. Dr. Andreas Kemna

Tag der Promotion: 25 Januar 2018
Erscheinungsjahr: 2019

Abstract

Fluid flow processes in the subsurface are accompanied by heat and mass transport with several important feedbacks including reactive flow, and precipitation/dissolution processes. Heat and mass transport through fractured rock masses occurs in many natural systems such as the plumbing of volcanic systems, mesothermal ore deposits, and post-seismic fluid flow. Anthropogenically-driven systems, such as fluid-injection in Enhanced Geothermal Systems (EGS), and the injection of waste-water from hydrocarbon extraction also involve heat and mass transport through porous or fractured rocks. Understanding in detail how mass and heat transfer interact in natural or in industrial applications requires numerical models in combination with field and laboratory experiments to determine the dominating factors. This thesis examines the impact of heat and mass transport on high pressure fluid propagation in the subsurface, as well as different numerical approaches of transient heat flow in fractured porous media and the heat exchange between flowing fluid and host rock.

Many fluid-triggered seismic events show a tendency for upward migration of the seismic cloud, generally assumed to reflect a fluid-pressure dependent permeability. In a numerical investigation that combines pressure-dependent permeability with thermal and salinity effects, it is found that over short timescales pressure-dependent permeability does indeed have the strongest influence on asymmetric diffusion. However, it is also demonstrated that over longer timescales, for example the lifetime of a geothermal reservoir, temperature and salinity effects play an increasingly important role.

Assessing the thermal field of a geothermal resource or in a CO_2 sequestration project is essential for proper design and management. Typically, numerical simulations assume that the fluid and solid phases are in thermal equilibrium, an assumption that has to date not been investigated in detail. This assumption is examined in this work by simulating fluid and heat flow in a simple geometry to analyse the influence of site specific parameters on the simulation result. It is shown that the equilibrium model is not sensitive to porosity contrasts, while the non-equilibrium model shows a sensitivity to porosity contrasts, with simulation results diverging more strongly in less permeable zones. In a simulation of a hypothetical geothermal system, the equilibrium model shows higher production temperatures with a divergence of up to 7 % between the approaches, which could impact the economic feasibility of a project.

Finally, a new approach is introduced to determine the heat transfer coefficient h between rock walls and flowing fluid using the non-equilibrium model. Based on a numerical experimental setup with simple geometry and steady state scenario, a dynamic heat transfer coefficient is derived that depends on fracture aperture and flow velocity. This model is based on well-defined physical parameters, it is adaptable to complex geometries, and intrinsically adjusts to spatial heterogeneities and temporal changes in flow and temperature field. A possible extension of this dynamic approach is demonstrated in numerical simulations the reservoir scale.

Contents

Nomenclature

a_{fs}	fluid-solid specific surface area
b	fracture aperture
C	salt concentration
$C_{\mathrm{wp}}(P_{\mathrm{w}})$	capacity coefficient
c_{p}	Specific heat capacity
D	fluid pressure diffusivity
d_{m}	molecular diffusion coefficient
d_{p}	rock particle diameter
$\mathbf{g}$	gravitational acceleration
h	interstitial heat transfer coefficient
h_{fs}	fluid-solid heat transfer coefficient
K	thermal conductivity
k	permeability
k_{r}	relative permeability
$\mathrm{Nu}_{\mathrm{fs}}$	fluid-to-solid Nusselt number
P	fluid pressure
P_{c}	capillary pressure
P_{e}	confining pressure
P_{r}	pressure scaling factor in van Genuchten equations
Q_{h}	heat transfer between fluid and solid phase
Q_{s}	volumetric fluid injection
$\mathbf{q}$	Darcy velocity
Re	Reynolds number
S	specific storativity of matrix
S_{α}	saturation of phase α
S_{ew}	effective water saturation
T	temperature
t	time
$\mathbf{v}$	intrinsic fluid velocity
x, y, z	position coordinates
β	compressibility
$\%\Delta T_{\mathrm{w}}$	dimensionless parameter to evaluate temperature difference between LTE and LTNE assumptions
ε	density coefficient
θ	volume fraction of fluid in REV
μ	dynamic viscosity
ρ	density
σ_{M}	effective mean stress
ϕ	porosity
ϕ_{r}	residual porosity

Subscripts

f	fluid phase
in	input
r	rock
s	solid phase
out	output
w	water
α	liquid or gas phase of fluid
0	reference value

1. Introduction

Fluid circulation in the Earth's crust is accompanied by transportation of heat and chemicals. These strongly coupled processes are an important part of fluid and rock interactions. Studying fluid, heat and mass flow in fractured porous media helps us better understand phenomena such as fluid driven aftershocks ([1, 2]), volcanic activities [2] and earthquake swarms [3] as well as industrial applications like geothermal systems [4] or nuclear waste disposal [5, 6, 7]. This work mainly focuses on fuild flow and mass transport in subsurface and how they affect each other.

1.1. Motivation

Fluid flow in the Earth's crust plays an important role in many natural phenomena. Depending on the depth, fluids in the crust originate from different sources. Deep circulating fluids originate from mantel degassing, dehydration of subduction plates and metamorphic processes while shallow crust fluids come mainly from infiltration of meteoric waters.

Each year about $4 \times 10^4\,\mathrm{km}^3$ of water is percolated in the continental crust [8]. The energy to circulate these fluids in global scale comes from two main sources. First, solar radiation that evaporates over $4 \times 10^5\,\mathrm{km}^3$ of oceanic water per year, and second, the Earth's internal heat generated by the inner core and decay of radioactive isotopes that propels fluids by convection, thermal expansion and chemical reactions [9].

From physical point of view, the main contributers to fluid circulation in the upper crust are pressure and geothermal gradients, which are always present in the Earth's subsurface. Hence, fluid flow is accompanied by and coupled with heat transport and sometimes results in natural activities like hot springs, hydrothermal vents and water convection at mid-ocean ridges.

This combination also appears in industrial applications such as seasonal thermal energy storage (STES), enhanced geothermal systems (EGS), nuclear waste disposal and carbon capture and sequestration systems (CCS). In STES systems, waste heat is stored underground to be used when necessary [10]. The waste heat could come from solar, household, or industrial sources. The energy can be stored underground in aquifer systems (ATES), constructed bore-hole systems (BTES), flooded mines or oil stores (CTES) and be used by means of heat exchangers.

Heat and fluid flow in porous media are also very important in depositing nuclear waste and carbon dioxide. A good assessment of the thermal field is essential since it influences diffusion and leakage of the stored material. Another application of these interactions is in geothermal systems which has made fluid flow and heat transfer particularly in fractured porous media an interesting topic in recent decades. Geothermal power has the potential to be a base-load power source and therefore an attractive choice as an alternative energy source [11].

In exploration of geothermal energy, relatively cold water is injected into a bore-hole in an area of fractured, high permeable rocks and as a result hot water is brought to surface through production bore-holes. There are different types of geothermal systems that extract heat in a wide range of depths: from bore-hole heat exchangers (BHE) that are suitable for depths below 300 m to EGSs that typically operate over 3 km deep. In an EGS the fracture network of the host rock is enhanced during stimulation phase to improve the hydraulic permeability.

Dynamics of the temperature field play a critical role not only in energy production estimation, but also in induced seismic activities during reservoir stimulation of an EGS. An increased micro-seismicity in stimulation phase of a geothermal reservoir is shown when thermal stresses are taken into account [12].

Understanding the dynamics of coupled heat and fluid flow in fractured porous media and fluid-rock interactions during these processes is substantial for explaining all of these natural or industrial phenomena.

1.2. Numerical simulation in hydrothermal systems

The real-world physical processes are commonly explained using mathematical formulation. These formulations are verified with laboratory experiments and measurements and modified afterwards if necessary. In many cases however, real-world measurements and simplified laboratory experiments are not enough to test the mathematical models. For example, in geophysics where complex geometry, extreme pressure and geothermal gradients of real-world cases cannot be reproduced in laboratory scale [13, 14]. Field studies cannot provide a clear picture because they run over a short period of time and do not deliver much information about coupled physical processes.

Numerical simulation is the appropriate tool that complements mathematical models, field and laboratory observations. It reduces complicated situations to simple procedures that can be handled more easily. This make numerical models applicable for complex geological systems that cannot be solved analytically. Another advantage is the flexibility offered by numerical modeling with variable parameters. This allows us to use and test a single model for various scenarios with different geometries, boundary and initial conditions. Depending on computational performance and method, it is also possible to model a scenario in a high temporal and spatial resolutions or over a long period of time. This is specially important for industrial applications mentioned above.

1.2.1. Discretization in numerical modeling of flow in porous media

There are different approaches to mathematically describe fractured porous medium and its petrophysical properties. Each approach makes different assumptions and simplifications that lead to some limitations that affect the results and therefore should be taken into account at interpretation time.

The first approach introduced here is the continuum method where a porous medium is described in terms of representative elementary volume (REV). This volume has to be large compared to pore or grain size to avoid pore-scale oscillations. On the other hand, it must be small enough to describe large scale heterogeneities. In other words, REV is the smallest volume which can represent the entire medium (figure 1.1).

All fluid and rock properties including porosity, permeability, pore size, saturation and thermal properties are averaged over this volume and the values represent medium properties at the continuum scale. As a result, the discrete microscopic scale in which each point is either fluid (liquid or gas) or solid, is transformed to a continuous one. All mechanical, hydraulic, thermal and chemical parameters and variables are considered for the REV [16, 1]. In this representation, single fractures are not described explicitly. Instead, they are expressed by

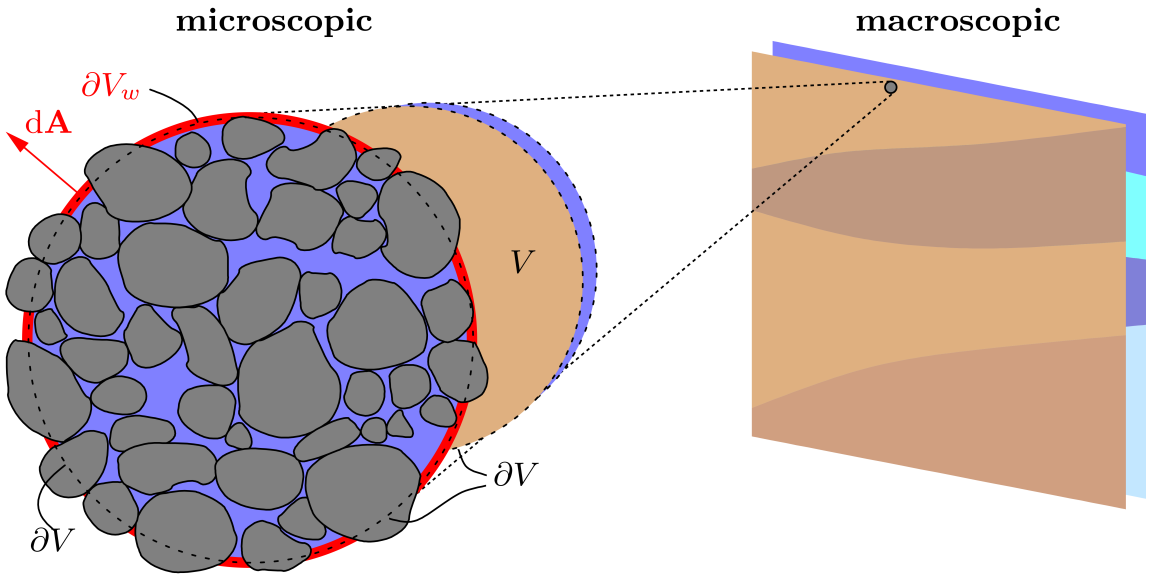

Figure 1.1.: Pore-scale view of a macroscopic volume V with boundary ∂V (dotted line). The microscopic view consists of rock grains with different radii and the pore space which is occupied by a fluid. A detailed distribution of solid and fluid phase is therefore possible for volume V, for instance the fluid phase volume V_w which is blue with the external boundary ∂V_w shown in red. In macroscopic view however, the fluid volume like other petrophysical physical properties are replaced by the local average or effective values. In continuum scale the smallest volume that is representative for the whole medium is called representative elementary volume (REV) [15].

assuming properties related to fractured area, e.g. higher permeability and porosity values for hydraulic processes. These permeability values are mostly exponentially proportional to load and fluid pressure. This exponential relation is confirmed by field observations and the results of laboratory experiments on fractured or intact rock samples [17, 18, 19]. Fracture generation is then introduced to this representation as an abrupt increase in permeability which can reproduce field measurements successfully [20].

In modeling small scales, results from REV representation can deviate from pore-scale description. This deviation grows by decreasing scale particularly near the boundaries.

An alternative to single continuum models which assume different physical properties for fractures and pore-space is the dual porosity representation of multiple media. Dividing simulated medium into pore-space as fluid storage and fracture network as high permeable flowing channels enables us to describe fast and slow flow in fractured reservoirs. This approach assumes that the pore-space domain with high porosity and less permeability interacts with the fracture domain via an exchange term which depends on geometrical considerations [22, 23]. Fractures are not depicted explicitly in this method but in the form of equidistant channels where a matrix rock is embedded as low permeability blocks (figure 1.2). Based on this topological design, single blocks of pore-space are isolated and the interaction between them is only possible via flow in fractures.

Flow dynamics can be described even more precisely when an extension of the aforementioned model, multiple porosity method, is applied. Dual porosity models are widely used in reservoir simulations to describe mass transport in fractured systems, and recently for heat transport [24, 25, 26, 21]. However, the concept of isolated rock blocks in this model,

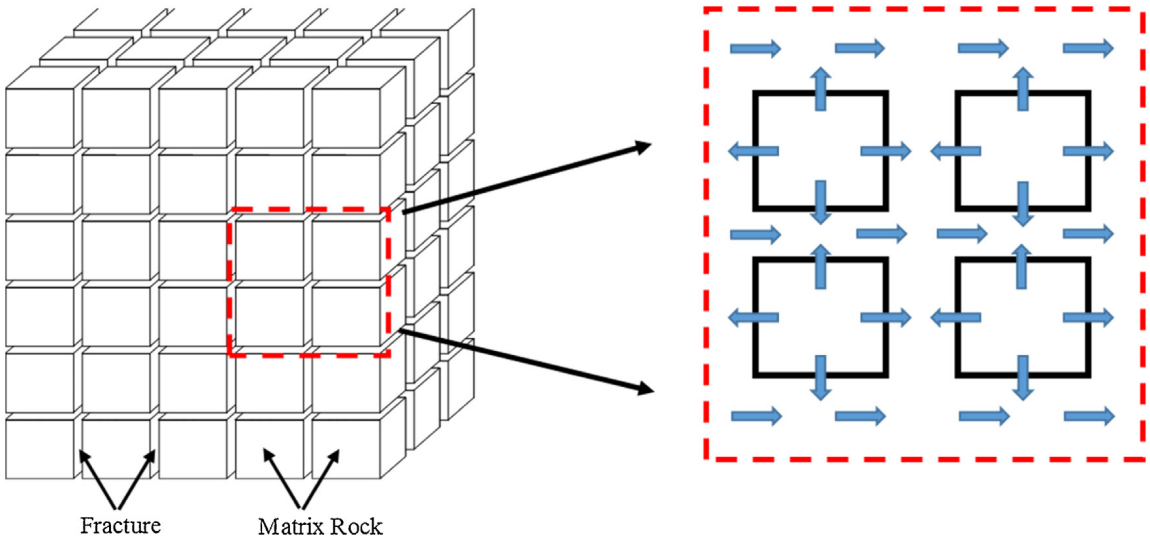

Figure 1.2.: The dual porosity model describes a system as two overlapping domains, a fracture domain and a pore-space one. This way, the fast flow in fractures can be distinguished from the slow one in the less permeable pore-space. These domains are coupled by an exchange term which depends on geometry [21].

leads to an unrealistic representation of the thermal behavior. In modeling geothermal systems for instance, this assumption may result in an extremely rapid reservoir cool-down.

Another way to describe fractured porous media, is using discrete fractured network (DFN) models where each fracture is defined exactly by position, orientation, aperture and other relevant parameters. Thus the interaction between fractures and pore-space can be calculated as well as the interaction among fractures themselves. Using this method, flow and transport model in fractures can be computed accurately. However, due to high computational costs, advective diffusive processes are often simplified to a pure advective one in a channel. The fracture network used in this method can be provided by geological mapping. However, precise mapping of all discontinuities in a field is not feasible. Therefore DFNs are often generated by stochastic models based on geophysical field measurements [27, 28, 29].

In this work, fractured porous media is described in the continuum representation and petrophysical parameters are set in this context. Assumed fracture networks are embedded in REVs and therefore no explicit definition of fracture orientation, length or other properties exist.

1.2.2. Numerical simulation tools

Since the early 1970 s computational methods have been applied in coupled geo-scientific problems. Yet, the development of numerical studies specifically in fractured porous media has been accelerated in the last two decades mainly due to the interest in the investigation of nuclear waste repositories and geothermal power generation. In both cases, long-term performance and safety evaluation demand a highly accurate prediction of the system behavior. Nuclear waste as an enduring heat source affects the surrounding soil and ground-water. Therefore, to keep the repository isolated, it has to be cooled down using fluid flow. This process is coupled with heat and solute transport, and influences mechanical stability. Geothermal systems have similar complexities to deal with.

Hydraulic stimulation by injecting high-pressure cold water into subsurface, alters hydraulic, mechanical, thermal and chemical state of reservoir. Due to high construction costs, this process has to be studied well beforehand, to avoid seismicity triggering and ground-water pollution on one hand and to have a good estimation of long-term power production, on the other hand [4, 30]. Meanwhile, there are many more applications for numerical simulation in geo-sciences.

Many scientific packages are available for simulation of thermo-, hydro-, mechanical-, chemical-processes (THMC) in the subsurface for commercial or academic use. These tools are widely used to describe natural phenomena or to predict behavior and reaction of industrial applications. Some of the most well-known packages are briefly mentioned below.

OpenGeoSys (OGS) is an open source and free software package capable of solving highly complex THMC processes in multiphase systems including phase transition. It is primarily based on the finite element method (FEM) and is applicable in numerical simulation of various geological problems such as CCS, nuclear waste deposition, water resources management and geothermal energy. OGS is platform-independent and its object-oriented design makes this package flexible to be implemented in other codes and scenarios. The graphical-user-interface (GUI) makes visual data management and analysis possible and the powerful post-processing 3D visualization is based on the Visualisation Toolkit (VTK) [31]. Computational parallelization in the framework of OGS is possible using PETSc routines [32, 33].

The TOUGH (Transport Of Unsaturated Groundwater and Heat) family of codes is another excellent simulator developed primarily for geothermal reservoir engineering but now widely applied to multiphase flow of multiple fluids with phase transition. Its implemented equation-of-states (EOS) covers a variety of fluid mixtures of water, air, NaCl and CO_2 [34, 35]. Spatial discretization is done using the integral finite difference (IFD) method and temporal discretization in finite differences. TOUGH is highly modular and therefore, it can be coupled with new packages to simulate different scenarios. TOUGH2 is the basic simulator to deal with multiphase fluid flow under pressure, gravity and viscous forces [36]. TOUGH+ is the object-oriented version, with extended range of thermodynamical water properties and is capable of simulating freezing and thawing processes in permafrost regions. TOUGHREACT is used for chemically reactive non-isothermal flows in fractured porous media [37, 38]. TOUGH can be coupled with the commercial package $FLAC^{3D}$ for TOUGH-FLAC which is a simulator for multiphase fluid flow, heat transport and geomechanics.

PFLOTREAN is also a free and open source software package for simulating multicomponent THC processes in subsurface. The code is object-oriented, written in Fortran and is massively parallelized using PETSc libraries. This solver can simulate coupled multiphase and chemically reactive transport using the finite volume method (FVM) [39, 40, 41].

Another free and open source simulator of multicomponent and multiphase fluid flow in fractured porous media is $DuMu^x$. The code structure is object-oriented and is written in C++ based on FVM. It has successfully simulated CO_2-brine scenarios as well as water uptake in root systems. Using adaptive grid makes $DuMu^x$ more efficient in simulation of infiltration processes [42].

MODFLOW, MT3DMS, SEAWAT and HYDROTHERM are different software packages belonging to U.S. Geological Survey (USGS). HYDROTHERM is a FDM code to solve two-phase solute flow in a range of 0 °C to 1200 °C [43]. SEAWAT is an open source, free and coupled version of MODFLOW and MT3DMS. This package focuses mainly on simulating 3D variable-density, saturated ground-water flow coupled with solute and heat transport using FDM. The code is written primarily in Fortran and is widely used for aquifer simulations [44].

The Complex Systems Modelling Platform, known as CSMP++, is also developed to simulate fluid flow and heat transport in fractured porous media with basic capabilities for geochemical and geomechanical processes. Complex realistic geometries can be represented by CSMP++ through unstructured meshes. The code is highly modular, written in C++ and based on FEM and FVM. The EOS used in CSMP++ covers a wide range of temperature, pressure and salt composition [45, 46, 47].

In addition to the above software packages, commercial softwares are available such as FEFLOW [48], HYDRUS [49] and ECLIPSE by Schlumberger which is one of the most advanced and prominent simulators in oil reservoir simulation. Multi-purpose solvers like COMSOL Multiphysics and several open source computational fluid dynamic (CFD) libraries can be used to simulate fluid flow in porous or fractured porous media.

In spite of all the available state-of-the-art software packages with a wide range of applications, describing heat transport in large scale fractured porous media remains a challenge. These simulators primarily assume immediate thermal equilibrium between fluid and solid phases (LTE) in thermal processes. This may be true in low geothermal gradient zones, but in presence of an intense heat source/sink as in nuclear waste repositories or geothermal systems, this assumption may not hold. The actual local thermal non-equilibrium (LTNE) model is not yet commonly implemented in existing simulators, not only because of its computational costs, but also because it requires more theoretical and experimental tests to reach a well-defined parametrization for the heat exchange between different phases.

Some studies show that using LTNE method, will result in fluid and solid phases to have similar temperatures [50, 51]. However, later studies show some cases where fluid temperature resulted from LTE differs significantly from the one from LTNE [52, 30, 53], indicating that LTE and LTNE have to be studied in parallel.

Even though there have been many recent studies in this area, there is still a lack of information about circumstances where LTE is applicable or the way fluid and solid heat equations are coupled under non-equilibrium conditions. These pieces of knowledge are essential to reach a correct macroscopic characterization of fluid-rock interactions in coupled fluid and heat transport.

1.3. Summary of scientific articles

This work focuses on coupled heat and solute transport to fluid flow in subsurface and consequences of this coupling. In chapter 2 theoretical background of fluid flow, heat and mass transport in porous media is explained in detail. In the next step general impacts of temperature gradients in non-linear groundwater flow is investigated. For this purpose, in chapter 3 a 1D model has been developed to examine the impacts of stress-dependent permeability, geothermal gradients and salinity, on non-symmetric fluid pressure diffusion in depth. Impact of thermal effects in propagation of the pressure front reveals the necessity to account for heat transport in modeling subsurface fluid flow, even if heat transfer itself is of minor interest.

Heat transport in porous media in continuum mechanics is divided to LTE and LTNE, as mentioned above. Chapter 4 compares these two models in a simple 2D macroscopic set-up to determine the sensitivity of these models to petrophysical properties of the system. Afterwards, a typical geothermal system is simulated in production phase under LTE and LTNE assumptions. The simulation results show higher fluid temperature under LTE assumption. In this case, LTNE provides us with the lower bounds of long-term heat flow which is essential for assessing investment risk and financial feasibility of a geothermal system. The major problem in LTNE is the absence of a physical model for the heat exchange term between different phases and components in a fractured porous medium. Chapter 5 addresses this problem and introduces a dynamic heat transfer coefficient depending on fracture aperture, flow velocity and thermal parameters.

1.3.1. Numerical study of asymmetric vertical fluid intrusion in deep reservoirs: effects of pressure, temperature and salinity

This manuscript investigates the underground non-linear pressure diffusion to explain asymmetric seismicity that has been observed in many fluid-triggered events. Possible origins for this asymmetry are first, a stress-dependent permeability causing higher flow rates upwards than downwards. Second and third reasons are buoyancy-driven flow due to a thermal or a salinity gradient.

A 1D model is developed to simulate non-linear fluid pressure in a saturated vertical profile as high pressure water is injected in the middle. Stress-dependent porosity and permeability leads to a clear rapid divergence of upward and downward fluid pressure, as expected. A thermal gradient though, influences the system in a more complex way. Fluid density and viscosity are both temperature-dependent and act against each other. Lower viscosity in deeper area causes a higher downward flow at first. The thermal buoyancy effect appears later since temperature diffuses more slowly than pressure, but it overcomes the effect of viscosity and makes higher upward flow in long-term. The thermal impact is tested once while the high pressure fluid has the same temperature as the injection area, once with higher temperature and finally high temperature, high pressure fluid is injected to a system with permeability gradient. The effect of buoyancy is stronger assuming a higher injection temperature. The strongest asymmetry belongs to the scenario where the impact of temperature and stress are

coupled. Density flow due to salinity contrast between high pressure fluid and the system does not influence pressure diffusion significantly.

1.3.2. Critical review of the local thermal equilibrium assumption in fracture networks and geothermal systems: dependence on permeability and porosity contrasts

Following chapter 3, it is clear that a coupled heat and ground-water model is needed, especially in regions with a high thermal gradient. This manuscript focuses on modeling heat transport in porous media while evaluating the standard LTE approach versus the LTNE. In order to do so, a 2D model for coupled fluid flow and heat transport is developed and verified using analytical solutions or experimental data.

Different sensitivity tests are performed on a simple geometry setup consisting of a host rock with an embedded layer in the middle with higher permeability. Impacts of porosity and permeability on LTE and LTNE models are studied by assigning different values to layer and host rock. High pressure cold water is injected into the host rock with higher initial temperature, and the output temperatures of the two models are compared. The results show that LTE is less sensitive to porosity changes. A convergence of the results is observed as the porosity contrast vanishes.

Afterwards, heat production of a generic geothermal system is modeled with a fully coupled heat and fluid flow model. For this purpose, an arbitrary heterogeneous fracture network is introduced with stress-dependent porosity and permeability values. Fluid density and heat capacity are functions of fluid temperature and pressure. High pressure cold water is injected to one corner of a reservoir at three different injection rates while the production well is positioned diagonal to the injection well. After 40 years of production, the difference between the output fluid temperature resulted from LTE and LTNE models is about 4 % while highest difference rises over 7 % in less permeable zones. This amount of uncertainty in heat extraction estimation may lead to undesirable economic consequences over the lifetime of a commercial geothermal system.

1.3.3. A dynamic heat transfer coefficient between fractured rock and flowing fluid

Chapter 4 confirms the importance of a LTNE heat transport model while dealing with heterogeneous porous media. This model however, is based on a heat transfer term between fluid and rock, whose parametrization is shown to be inaccurate by experimental data. The heat exchange term is proportional to the temperature difference and the heat transfer area between phases. Although the proportionality constant, called heat transfer coefficient, is estimated using various methods, resulting values are rather high and constant in time and space.

In this manuscript, a dynamic heat transfer coefficient for a single fractured porous medium is derived depending on fracture aperture, flow velocity and thermal parameters. It

intrinsically adjusts to temporal changes in flow and temperature field as well as spatial heterogeneities of the system. The model is verified with a series of experiments in which fluid flows through a single fracture in a rock specimen. Inflow temperature and velocity as well as fracture aperture and rock temperature are varied over 78 different experiments. The model can closely reproduce the steady state measured output temperatures of these measurements.

An extended version of this model is then used to model a transient heat flow in field scale fractured media. Heat production of a heterogeneous geothermal reservoir over 25 years of production is compared using a dynamic and static heat transfer coefficients. Water density, viscosity and heat capacity are considered to be temperature and pressure-dependent. The temperature breakthrough curve of the simulation with dynamic coefficient shows a more rapid drop compared to the simulations with constant coefficients. The extended dynamic heat transfer coefficient for field scale simulations shows the same evolution as in the laboratory experiments.

2. Theoretical background

The physical processes considered in this work are fluid, mass and heat flow which are highly coupled through velocity field, saturation, porosity and permeability of rock as well as fluid properties like pressure, temperature and concentration dependent density, viscosity, heat capacity and thermal conductivity. Figure 2.1 shows the interaction between these processes in a THC simulator. Based on the representative elementary volume concept (REV), a continuum model is assumed for a porous medium and differential equations describing the physical processes are derived from conservation laws.

2.1. Fluid flow

The fluid flow model considered in this work is at Darcy scale and based on the following assumptions: the solid phase is incompressible and homogeneous and fluid undergoes no thermal expansion or phase transition. Dissolution or evaporation in fluid phase are neglected as well as chemical reactions between fluid and solid phases.

2.1.1. Single phase flow

Fluid flow in a saturated porous medium can be described by the fluid mass balance:

$$\frac{\partial(\phi\rho_{\mathrm{f}})}{\partial t} + \nabla(\rho_{\mathrm{f}}\mathbf{q}) = \rho_{\mathrm{f}} Q_{\mathrm{s}} \ , \tag{2.1}$$

where ϕ is rock porosity, ρ_{f} is fluid density and $\mathbf{q}$ is the macroscopic volume flux of the fluid known as Darcy velocity. $\mathbf{q}$ is not the real fluid velocity but corresponds to the velocity that sustains the given volume flux outside of a porous medium. It is related to the pore water velocity $\mathbf{v}$ as $\mathbf{q} = \phi\mathbf{v}$ [15].
Fluid density depends on pore pressure (P), solute concentration (C) and fluid temperature (T).

The solid matrix is rigid and due to simplification, porosity depends only on pressure and stress. Under these circumstances the first term of the left hand side of equation (2.1) can be written as:

$$\frac{\partial}{\partial t}(\phi\rho_{\mathrm{f}}) = \phi\frac{\partial\rho_{\mathrm{f}}}{\partial t} + \rho_{\mathrm{f}}\frac{\partial\phi}{\partial t} \ . \tag{2.2}$$

Fluid density depends on fluid pressure, temperature and concentration of chemicals. Hence, equation (2.2) can be expanded as:

$$\frac{\partial}{\partial t}(\phi\rho_{\mathrm{f}}) = \phi\frac{\partial\rho_{\mathrm{f}}}{\partial P}\frac{\partial P}{\partial t} + \phi\frac{\partial\rho_{\mathrm{f}}}{\partial C}\frac{\partial C}{\partial t} + \phi\frac{\partial\rho_{\mathrm{f}}}{\partial T}\frac{\partial T}{\partial t} + \rho_{\mathrm{f}}\frac{\partial\phi}{\partial P}\frac{\partial P}{\partial t} \tag{2.3}$$

$$= \phi\frac{\partial\rho_{\mathrm{f}}}{\partial C}\frac{\partial C}{\partial t} + \phi\frac{\partial\rho_{\mathrm{f}}}{\partial T}\frac{\partial T}{\partial t} + \left(\phi\frac{\partial\rho_{\mathrm{f}}}{\partial P} + \rho_{\mathrm{f}}\frac{\partial\phi}{\partial P}\right)\frac{\partial P}{\partial t} \ . \tag{2.4}$$

Using the definition of fluid and pore compressibility respectively:

$$\beta_{\mathrm{f}} = \frac{1}{\rho}\frac{\partial\rho}{\partial P} \ , \tag{2.5}$$

$$\beta_{\phi} = \frac{1}{1-\phi}\frac{\partial\phi}{\partial P} \ , \tag{2.6}$$

and defining the specific storativity of the matrix as:

$$S = \phi\beta_{\mathrm{f}} + (1-\phi)\beta_{\phi} \ , \tag{2.7}$$

one can rewrite the equation (2.1) in the following form:

$$\phi\frac{\partial\rho_{\mathrm{f}}}{\partial C}\frac{\partial C}{\partial t} + \phi\frac{\partial\rho_{\mathrm{f}}}{\partial T}\frac{\partial T}{\partial t} + \rho_{\mathrm{f}}S\frac{\partial P}{\partial t} + \nabla\left(\rho_{\mathrm{f}}\mathbf{q}\right) = \rho_{\mathrm{f}}Q_{\mathrm{s}} \ . \tag{2.8}$$

The Boussinesq approximation is often used in buoyancy-driven fluid dynamics. It assumes that density variations in the fluid mass balance are negligible, except in gravitational terms. Considering this approximation, equation (2.8) is simplified to:

$$S\frac{\partial P}{\partial t} + \nabla\mathbf{q} = Q_{\mathrm{s}} \ . \tag{2.9}$$

According to Darcy's law, which describes fluid flow through a porous medium, the fluid volume flux is proportional to the pressure gradient. Here a generalized Darcy law is adopted assuming a laminar flow, neglecting the inertial effects:

$$\mathbf{q} = -\frac{k}{\mu}\nabla(P - \rho_{\mathrm{f}}\mathbf{g}) \ . \tag{2.10}$$

This yields to the pressure diffusion equation for a saturated porous medium:

$$S\frac{\partial P}{\partial t} + \nabla\cdot\left(-\frac{k}{\mu}\left(\nabla P - \rho_{\mathrm{f}}\mathbf{g}\right)\right) = Q_{\mathrm{s}} \ . \tag{2.11}$$

In a homogeneous medium, where rock permeability and fluid viscosity are constant, this equation is linear. Though, heterogeneity and anisotropy can be implemented in this formulation, considering a variable viscosity and higher a permeability tensor of higher orders.

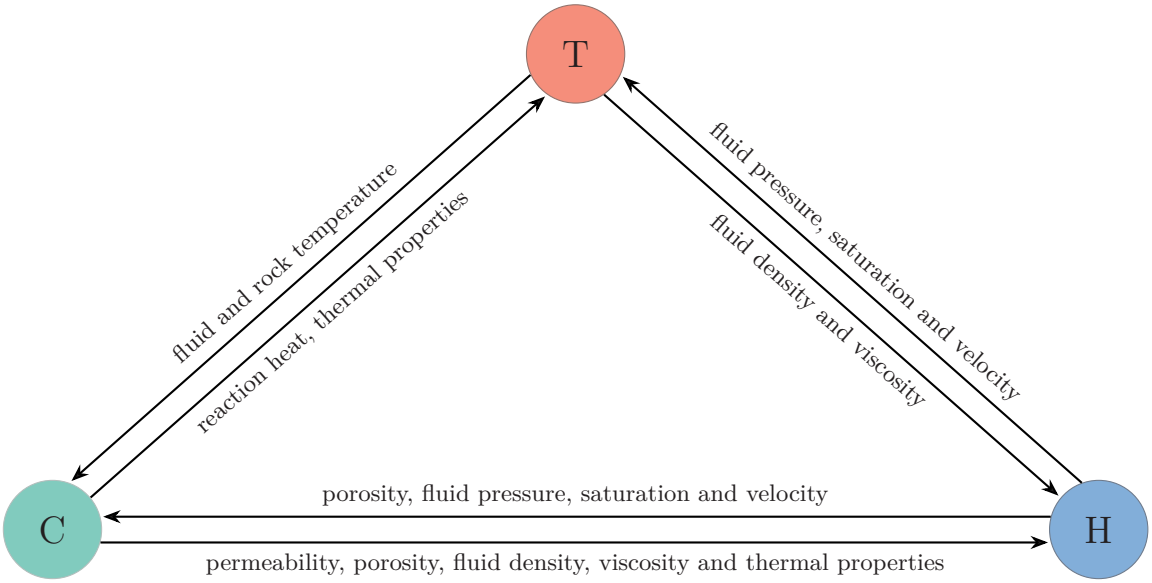

Figure 2.1.: Thermo-, Hydro-, Chemical-processes are coupled via variable fluid and rock properties. There are three modules in a THC simulator to solve the corresponding PDEs and send the required information to modify the simulation parameters and variables.
H-module contains simulation of single and two phase flow with the corresponding Darcy velocity. Porosity and permeability of rock, fluid density, viscosity and heat capacity are pressure dependent. Velocity field is needed for solving advective-diffusive equations of temperature and solute transport and also determining heat transfer between fluid and rock. T-module deals with fluid and rock temperature fields under the LTE or LTNE assumptions. Temperature influences chemical reaction rates, fluid density and viscosity. Chemical reactions and concentrations are contained in C-module. Through these reactions rock properties as porosity and permeability can be changed. Solute concentration affects heat conductivity and capacity as well as viscosity and density of the fluid phase.

2.1.2. Two-phase flow

Governing equations for two-phase flow can be derived in a similar way as described in section 2.1.1 by introducing relative permeability k_α, and saturation S_α of each fluid phase. In the continuum description, porosity can be written as the sum of volume fractions of the wetting phase and the non-wetting phase. For simplicity, in this work the wetting and non-wetting phases are assumed to be water and air, respectively. Then:

$$\phi = \theta_\mathrm{a} + \theta_\mathrm{w} \quad , \tag{2.12}$$

where θ_w and θ_a are the volume fractions of the water and air in the REV. It is more convenient for further formulation to introduce phase saturation, S_α which is the fraction of pore-space filled by water and air, respectively:

$$S_\alpha = \frac{\theta_\alpha}{\phi} \ , \tag{2.13}$$

with α being water (wetting) or air (non-wetting). Equations (2.12) and (2.13) require that the sum of phase-saturations is equal to one:

$$S_\mathrm{w} + S_\mathrm{a} = 1 \ . \tag{2.14}$$

Using equation (2.13) and assuming no source and sink term, the mass conservation law for each fluid phase is written as:

$$\frac{\partial}{\partial t}\left(\rho_\alpha S_\alpha \phi\right) + \left(\rho_\alpha \mathbf{q}_\alpha\right) = 0 \ . \tag{2.15}$$

Besides, equation (2.16) for a two-phase flow is called the Buckingham-Darcy law in hydrology and the generalized Konzey-Carmen law in petroleum industry:

$$\mathbf{q}_\alpha = -\frac{k_\alpha k_0}{\mu_\alpha}\nabla(P_\alpha - \rho_\alpha \mathbf{g}) \ . \tag{2.16}$$

Since rock permeability can be different for each phase and therefore introduced as an intrinsic permeability k_0 and a relative phase permeability k_α which can change between 0 and 1. k_α depends on phase saturation and reaches its maximum value, in the case of full saturation of phase α.
By substituting the phase Darcy velocities from equation (2.16) into equation (2.15) , a set of equations is derived to describe two-phase flow in a porous medium:

$$\frac{\partial}{\partial t}\left(\rho_\mathrm{w} S_\mathrm{w} \phi\right) - \nabla\left[\frac{\rho_\mathrm{w} k_0 k_\mathrm{w}}{\mu_\mathrm{w}}\left(\nabla P_\mathrm{w} - \rho_\mathrm{w}\mathbf{g}\right)\right] = 0 \ , \tag{2.17}$$

$$\frac{\partial}{\partial t}\left(\rho_\mathrm{a} S_\mathrm{a} \phi\right) - \nabla\left[\frac{\rho_\mathrm{a} k_0 k_\mathrm{a}}{\mu_\mathrm{a}}\left(\nabla P_\mathrm{a} - \rho_\mathrm{a}\mathbf{g}\right)\right] = 0 \ . \tag{2.18}$$

These equations contain four variables (S_w, S_a, P_w and P_a) and are coupled through equation (2.14).

Another related variable that couples equations (2.17) and (2.18), is macroscopic capillary pressure P_c. It is caused by adsorption and capillary forces and defined as the difference between water and air pressure. Capillary pressure increases with decreasing water saturation and pressure, if the pore air pressure is constant. Thus, it is assumed to be a function of water saturation:

$$P_c(S_w) = P_a - P_w \ . \tag{2.19}$$

The capillary pressure-saturation relationship cannot be determined analytically since it depends on the pore geometry and history of the flow. Though, there are many relations which describe a functional correlation between capillary pressure and saturation. Among those are the models by Brooks and Corey [54] and van Genuchten [55], the most famous ones. The former model can be written in the following form:

$$S_{ew} = \begin{cases} \left(\frac{P_c}{P_n}\right)^{n_b} & \text{if} \quad P_c > P_n \\ 1 & \text{if} \quad P_c \leq P_n \end{cases} \ , \tag{2.20}$$

$$P_c = P_n \left(S_{ew}\right)^{\frac{-1}{n_b}} \ , \tag{2.21}$$

with S_{ew} being effective water saturation, P_n the air-entry pressure and n_b a parameter related to the pore-size distribution and commonly has a value between 0.2 and 5. Air entry pressure is the value that air pressure has to exceed in order to be able to intrude a water saturated porous medium. Above this value, the water saturation decreases while capillary pressure increases and the slope of drainage curve depends on the pore-size distribution. If the pore-size is distributed widely, the porous medium is drained gradually and n_b is smaller [56]. Effective saturation of each fluid phase α is defined as:

$$S_{e\alpha} = \frac{S_\alpha - S_\alpha^{min}}{S_\alpha^{max} - S_\alpha^{min}} \ , \tag{2.22}$$

where S_α^{min} and S_α^{max} are the minimum and maximum possible saturation values depending on the porous sample.
The major drawback of the Brooks-Corey parametrization is the discontinuity when the capillary pressure is equal to the air-entry pressure. This problem is resolved in the other well-known model introduced by van Genuchten [55] as:

$$S_{ew} = \left[\left(\frac{P_c}{P_r}\right)_g^n + 1\right]^{-m_g} \ , \tag{2.23}$$

$$P_c = P_r \left[\left(S_{ew}\right)^{\frac{-1}{m_g}} - 1\right]^{\frac{1}{n_g}} \ . \tag{2.24}$$

P_r is a scaling factor for pressure which depends on the mean pore size. It is commonly chosen so that $P_c \approx 10P_r$ [57]. n_g and m_g are empirical parameters depending on the pore size distribution and it is common to assume $m_g = 1 - \frac{1}{n_g}$. Figure 2.2 demonstrates the results of saturation-capillary measurements on silt loam soil and the fitted curves from Brooks-Corey and van Genuchten models [58]. Capillary pressure head h_c which is used

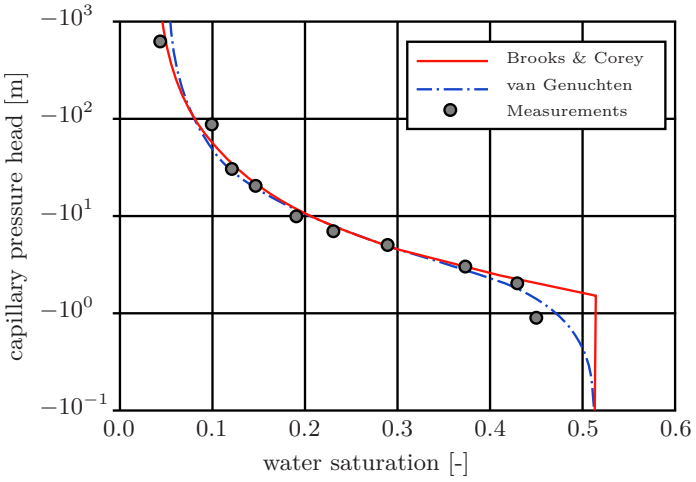

Figure 2.2.: Capillary pressure measured for silt loam soil and fitted curves of Brooks-Corey and van Genuchten models in terms of pressure head h_c (adopted from [58]). The discontinuity at $S_w \approx 0.51$ and h_c=−2 m is the main drawback of the Brooks-Corey model which is solved by van Genuchten parametrization.

in this figure, is an alternative to P_c and can be calculated by replacing P_n and P_r by the corresponding pressure heads. The difference between two models at $S_w = 0.5$ and h_c=−2 m is remarkable.

To make equations (2.17) and (2.18) easier to solve, one may parameterize the relative permeabilities, k_α. There are various analytical and empirical models for this purpose, based on pore-size distribution and the connectivity between pores [59, 60], etc. One common statistical model is introduced by Burdine [61]:

$$k_w = S_{ew}^2 \left(1 - \left(1 - S_{ew}^{\frac{1}{m_g}}\right)^{m_g}\right) , \tag{2.25}$$

$$k_a = (1 - S_{ew})^2 \left(1 - S_{ew}^{\frac{1}{m_g}}\right)^{m_g} . \tag{2.26}$$

To reduce the variables, permeability functions as well as capillary pressure are written in terms of water phase saturation.

Equations (2.17) and (2.18) are simplified up to this point by rewriting air saturation and relative permeabilities in terms of water saturation and water saturation in terms of capillary pressure. Thus, two unknown variables are remained for the system of two PDEs. However, the coupling through capillary pressure-saturation-phase permeability makes the numerical solution of these equations extremely complicated. Thus, further assumptions have to be considered in order to simplify the system of PDEs.

A common assumption in reservoir modeling is considering the pore-space connected to the atmosphere. Since the air viscosity is smaller than the water viscosity at the same temperature, air mobility is much larger than water mobility. If the air phase of the porous medium assumed to be connected to the atmosphere, any pressure change in this phase is compensated immediately instead of compression or expansion. This means the air pressure is considered as the reference atmospheric pressure $P_{atmosphere} = 0$, thus: $P_c = -P_w$ and the number of unknown variables is reduced to one. This assumption brings about an enormous

advantage in numerical modeling of water-air systems in laboratory scale as well as field scale.

As a result, equation (2.17) is expressed in terms of $P_{\mathrm{w}}(S_{\mathrm{w}})$ analogous to the single phase flow. The temporal term of the equation can be rewritten as:

$$\frac{\partial}{\partial t}\left(\rho_{\mathrm{w}}\phi S_{\mathrm{w}}\right) = \phi\rho_{\mathrm{w}}S_{\mathrm{w}}\beta_{\mathrm{w}}\frac{\partial P_{\mathrm{w}}}{\partial t} + \phi\rho_{\mathrm{w}}\frac{\partial S_{\mathrm{w}}}{\partial P_{\mathrm{w}}}\frac{\partial P_{\mathrm{w}}}{\partial t} \ . \tag{2.27}$$

Taking the Boussinesq approximation into account, the pressure diffusion equation for water is derived as:

$$\phi\left(S_{\mathrm{w}}\beta_{\mathrm{w}} + C_{\mathrm{wp}}(P_{\mathrm{w}})\right)\frac{\partial P_{\mathrm{w}}}{\partial t} - \nabla\left[\frac{k_0 k_{\mathrm{w}}}{\mu_{\mathrm{w}}}\nabla\left(P_{\mathrm{w}} + \rho_{\mathrm{w}}\mathbf{g}\right)\right] = 0 \ , \tag{2.28}$$

which is known as Richards equation [62]. $C_{\mathrm{wp}}(P_{\mathrm{w}})$ denotes capacity coefficient defined as:

$$C_{\mathrm{wp}}(P_{\mathrm{w}}) = \frac{\partial S_{\mathrm{w}}}{\partial P_{\mathrm{w}}} \tag{2.29}$$

and can be determined from capillary-saturation relationships, for instance equation (2.23).

2.1.3. Permeability variations

In field scale settings, rock permeability is not constant and can be strongly heterogeneous. In order to model such systems, it is commonly assumed that matrix permeability is stress or pressure dependent (e.g. [63, 1, 64, 16]). This dependency is described either using a power law or an exponential relationship [65]. The former one can be written as:

$$k = k_0\left(\frac{P_{\mathrm{e}}}{P_0}\right)^{\gamma} \ , \tag{2.30}$$

with k_0 being permeability under atmospheric pressure P_0, P_{e} confining pressure and γ being the nonlinearity of the pressure diffusion [66]. The exponential formulation is introduced by David et al. [67] and has been widely used ever since (e.g. [1, 68, 16]):

$$k = k_0 e^{-\alpha(P_{\mathrm{e}} - P_0)} \ , \tag{2.31}$$

with α being an empirical constant. Furthermore, many studies adopt a porosity dependent permeability and consider porosity to be stress and pressure dependent [16, 69, 70, 71]:

$$\phi = \phi_{\mathrm{r}} + (\phi_0 - \phi_{\mathrm{r}})\, exp\left(a \cdot \sigma_{\mathrm{M}}\right) \ , \tag{2.32}$$

$$k = k_0\ exp\left[b\left(\frac{\phi}{\phi_0} - 1\right)\right] \ , \tag{2.33}$$

where ϕ_r is residual porosity, ϕ_0 and k_0 are porosity and permeability at zero mean stress, respectively and a and b empirical control parameters. In this work, equations (2.32) and (2.33) are used for the porous rock. Regarding notably higher permeability and porosity values in fracture zones, k_0 and ϕ_0 are assumed to be larger in this areas.

2.2. Solute transport

In this work, chemical reactions and also dissolution and precipitation effects are neglected and therefore, rock permeability and porosity do not change due to solute transport. This part of the model requires current information about fluid velocity, pressure, temperature, saturation and volume fraction to compute fluid solute concentration. Nonreactive solute transport in saturated porous media can be described as [72]:

$$\phi \frac{\partial C}{\partial t} + \mathbf{q} \cdot \nabla C - \nabla \cdot (\phi \mathbf{D}(\mathbf{q}) \nabla C) = 0 \ . \tag{2.34}$$

C is salt concentration in fluid phase, $\mathbf{q}$ Darcy velocity and $\mathbf{D}(\mathbf{q})$ is the diffusion tensor defined as:

$$\mathbf{D}(\mathbf{q}) = d_{\mathrm{m}}\mathbf{I} + \frac{\alpha_{\mathrm{l}}}{|\mathbf{q}|} \begin{bmatrix} q_x^2 & q_x q_y \\ q_x q_y & q_y^2 \end{bmatrix} + \frac{\alpha_{\mathrm{t}}}{|\mathbf{q}|} \begin{bmatrix} q_y^2 & -q_x q_y \\ -q_x q_y & q_x^2 \end{bmatrix} \ . \tag{2.35}$$

d_{m} is the molecular diffusion coefficient, I is the unit tensor , α_{l} and α_{t} longitudinal and transverse dispersivities, respectively. d_{m} depends generally on pressure, temperature and composition of the mixture. When the porous medium is not saturated, porosity has to be replaced with ϕS in equation (2.34).

Assuming no chemical reactions results in neglecting reaction heat as a source in the heat transport part. However, this modules are still strongly coupled through fluid heat capacity which depends on salt concentration. Salinity affects also fluid viscosity and density and this way, it is coupled to fluid flow (figure 2.1).

2.3. Heat flow

Like solute transport, heat transport is mathematically described by an advection-diffusion equation. Though, through interaction with the solid matrix, it is more complex. As presented in figure 2.1, coupling to the fluid flow part is done by receiving the current state of rock porosity, fluid velocity, density and saturation and sending back the modified variables. Besides, this process is coupled to solute transport through a temperature dependent molecular diffusion coefficient and fluid density.

The simplest model to describe heat transfer in a porous medium, is based on an assumption where fluid and porous medium reach thermal equilibrium immediately. Thus, $T = T_{\mathrm{f}} = T_{\mathrm{s}}$ is representing the solid and fluid temperature. Averaging over the REV leads to [73]:

$$(\rho c_{\mathrm{p}})_{\mathrm{m}} \frac{\partial T}{\partial t} + \phi \, (\rho c_{\mathrm{p}})_{\mathrm{f}} \, \mathbf{v} \nabla T - K_{\mathrm{m}} \nabla^2 T = Q_{\mathrm{h}} \ . \tag{2.36}$$

$(\rho c_{\mathrm{p}})_{\mathrm{m}}$ and K_{m} are overall thermal capacity per unit volume and overall conductivity

respectively, weighted by porosity:

$$(\rho c_{\mathrm{p}})_{\mathrm{m}} = \phi\,(\rho c_{\mathrm{p}})_{\mathrm{f}} + (1-\phi)\,(\rho c_{\mathrm{p}})_{\mathrm{s}} \ , \tag{2.37}$$

$$K_{\mathrm{m}} = \phi K_{\mathrm{f}} + (1-\phi) K_{\mathrm{s}} \ . \tag{2.38}$$

c_{p} is specific heat at constant pressure, K is thermal conductivity, $\mathbf{v}$ is fluid velocity and Q_{h} is heat production per unit volume. This formulation is called local thermal equilibrium (LTE) approach. The most important assumptions introduced in the derivation of equation (2.36) are [74]:

- the porous medium is isotropic and saturated
- there is no heat exchange between fluid and solid
- viscous dissipation and radioactive effects are negligible
- effects of thermal expansion are neglected
- fluid temperature does not exceed any critical value and no phase transition occurs

In an unsaturated air-water system, where the role of heat transport via air is negligible, the above equations have to be modified by multiplying porosity value by water saturation.

In the absence of local thermal equilibrium, fluid and solid temperature fields are described by two differential equations which are coupled via an heat exchange term. In local thermal non-equilibrium (LTNE) equation (2.36) has to be replaced by [74]

$$\phi(\rho c_{\mathrm{p}})_{\mathrm{f}} \frac{\partial T_{\mathrm{f}}}{\partial t} + \phi(\rho c_{\mathrm{p}})_{\mathrm{f}} \mathbf{v} \cdot \nabla T_{\mathrm{f}} = \phi K_{\mathrm{f}} \nabla^2 T_{\mathrm{f}} + h_{\mathrm{fs}}\,(T_{\mathrm{s}} - T_{\mathrm{f}}) \ , \tag{2.39}$$

$$(1-\phi)(\rho c_{\mathrm{p}})_{\mathrm{s}} \frac{\partial T_{\mathrm{s}}}{\partial t} = (1-\phi) K_{\mathrm{s}} \nabla^2 T_{\mathrm{s}} + h_{\mathrm{fs}}\,(T_{\mathrm{f}} - T_{\mathrm{s}}) \ . \tag{2.40}$$

h_{fs} is the heat transfer coefficient between fluid and solid. There are various experimental and analytical models describing h_{fs}. In chapter 4, the model introduced by Dixon and Cresswell is used which considers $h_{\mathrm{fs}} = a_{\mathrm{fs}} h$ in a porous bed of particles with a_{fs} as specific fluid-solid surface area and h as interstitial heat transfer coefficient defined below [75]:

$$a_{\mathrm{fs}} = \frac{6(1-\phi)}{d_{\mathrm{p}}} \ , \tag{2.41}$$

$$\frac{1}{h} = \frac{d_{\mathrm{p}}}{\mathrm{Nu}_{\mathrm{fs}} K_{\mathrm{f}}} + \frac{d_{\mathrm{p}}}{\beta K_{\mathrm{s}}} \ , \tag{2.42}$$

with $\mathrm{Nu}_{\mathrm{fs}}$ as fluid-to-solid Nusselt number, d_{p} as particle diameter and β is a geometrical parameter which is considered as 10 if the particles are spherical [74]. $\mathrm{Nu}_{\mathrm{fs}}$ depends on the Reynolds number and can vary over two orders of magnitude for low values of Reynolds number. In chapter 5, h is discussed in detail as a dynamic parameter depending on fluid velocity.

The LTE condition is widely assumed while modeling flow and heat transfer. The main advantage of this assumption is significantly lower computational costs. Beside the one more equation that needs to be solved in the LTNE model, it contains an extra limitation an for the simulation time-step due to the fluid-solid heat transfer term, which does not appear in the LTE model. However, it has been shown that the LTE condition is not valid in transient conditions [51, 30].

2.4. Numerical method

Above, a set of PDEs are derived in sections 2.1 to 2.3 to model a coupled system of fluid flow with mass and heat transfer. Due to the complexity, these equations can be solved analytically only in simplified geometries with constant rock and fluid properties. Numerical simulations however, can model the dynamics of coupled variables in more complicated geometries and boundary conditions. For this purpose, a numerical code in C++ is developed using the finite difference method (FDM).

The diffusion equation is part of all the studied physical processes in this work. It is assumed to be linear in heat and mass flow but where permeability and viscosity are not constant, pressure equation becomes non-linear. The general form of this equation in the one dimensional scalar field u is

$$\frac{\partial u}{\partial t} = \frac{\partial}{\partial x}\left(D\frac{\partial u}{\partial x}\right) \ , \tag{2.43}$$

with D as diffusivity. By discretization of space and time as $x_j = x_0 + j\Delta x$ and $t_n = t_0 + n\Delta t$, equation (2.43) can be written in differences:

$$\frac{u_j^{n+1} - u_j^n}{\Delta t} = \frac{D_{j+\frac{1}{2}}\left(u_{j+1}^n - u_j^n\right) - D_{j-\frac{1}{2}}\left(u_j^n - u_{j-1}^n\right)}{(\Delta x)^2} \ , \tag{2.44}$$

where

$$D_{j+\frac{1}{2}} = D(x_{j+\frac{1}{2}}) \ , \tag{2.45}$$

with Δx and Δt as the spatial grid size and the time-step, respectively [76]. Here, a forward difference in time and a second order centered difference in space scheme is used to determine u at the next time-step. Therefore, the scheme is called forward in time, centered in space (FTCS). As it can be seen in equation (2.44), the value of each grid point in time-step $n+1$ is calculated explicitly from the known quantities of time-step n. Hence, FTCS is called a fully explicit scheme.

Applying von Neumann stability analysis leads to the stability criterion for the time-step:

$$\Delta t \leq \min_j \left[\frac{(\Delta x)^2}{2D_{\mathrm{j}+\frac{1}{2}}}\right] \ . \tag{2.46}$$

In other words, the maximum time-step has to be smaller than the time an anomaly needs to diffuse from one grid point to the adjacent one. The main disadvantage of the FTCS method is slow simulation speed which is limited due to grid size. It is also notable that equation (2.46) is only valid for $D_j\Delta t > 0$, thus this method is unconditionally unstable for negative diffusivities [77].

In addition to diffusion process, heat and mass are transported due to fluid flow, i.e. the corresponding PDEs get contain an additional term for advection and the general equation

for an arbitrary scalar field u has the following form:

$$\frac{\partial u}{\partial t} + v_x \frac{\partial u}{\partial x} = \frac{\partial}{\partial x}\left(D \frac{\partial u}{\partial x}\right) \ , \tag{2.47}$$

with v_x being velocity in x-direction and assuming no source or sink term. For simplicity, diffusion and advection processes are computed separately. This way, the one dimensional advection equation is expressed as:

$$\frac{\partial u}{\partial t} + v_x \frac{\partial u}{\partial x} = 0 \ . \tag{2.48}$$

The two main issues by modeling the advection equation are numerical dispersion and oscillatory artifacts, which can appear if sharp gradients in the advected material exist. As said above, because of the negative diffusivity, the FTCS method is unstable and cannot be used for advection equation. Yet, there are various methods to deal with advection equation such as upwind scheme, staggered leapfrog, marker-in-cell or semi-Lagrangian methods.

Upwind scheme is obtained by replacing central derivation in FTCS scheme with forward or backward derivation. Being first order in space, it is less accurate than FTCS and moreover, suffers numerical diffusion. One can replace the first order time derivative in FTCS with second derivative and derive the staggered leapfrog method. In other words, information of two time-steps are required and has to be stored [77].

The upwind and staggered leapfrog methods are both defined on an Eulerian grid. In modeling non-diffusive advections it is common to use an Eulerian/Lagrangian approach and combine advecting tracers or markers with a fixed Eulerian grid. The marker-in-cell technique is based on this approach and is demonstrated in figure 2.3. Physical properties such as temperature and density are given to a large amount of markers which are initially distributed on the grid (that can be regularly- or irregularly-spaced). According to the velocity field, markers are advected in the simulation domain. The properties are interpolated from markers to the Eulerian grid [78].

In spite of accuracy and flexibility, this method is not appropriate in simulation of transient flows in heterogeneous media over a long period of time. In such scenarios marker density over the simulation domain is inhomogeneous and may fail delivering information about certain nodes of the Eulerian grid. Besides, combining advection and diffusion requires also an interpolation from the grid to the markers which results in numerical diffusion. Furthermore, applying this method increases the computational time considerably.

The Semi-Lagrangian method is also based on an Eulerian/Lagrangian combination. It has lower numerical diffusion and less computational costs comparing to the marker-in-cell method.

The main idea of this method is to compute the position X of a certain particle in the last time-step t_n and consider its physical properties, e.g. temperature, for position x_j in the next time-step (figure 2.4). As X is not located necessarily on a grid point, an interpolation

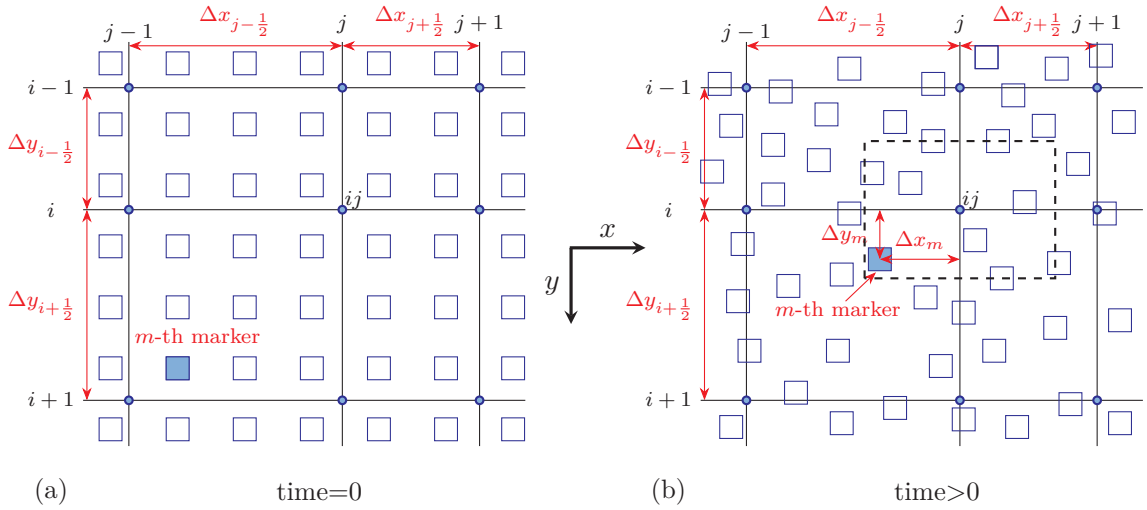

Figure 2.3.: Schematic demonstration of the marker-in-cell method. (a) The initial arrangement of Lagrangian markers is shown on an irregularly-spaced Eulerian grid. (b) The markers have been advected according to the velocity field and the physical properties are interpolated from the markers to the Eulerian nodes by considering the distance between the marker and the node i.e. Δx_m and Δy_m regarding the m-th marker and ij-th node. The dashed boundary represents the area where the markers are used for interpolation to the ij-th node (based on [78]).

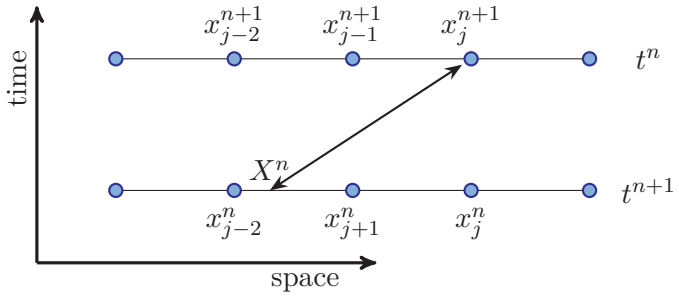

Figure 2.4.: Basic scheme of semi-Lagrangian method on a one-dimensional grid. The particle on the j-th node at time t^{n+1}, has been in position X at time t^n. Physical properties on this position are interpolated from adjacent nodes and assign to the j-th node at time t^{n+1} (modified from [77]).

of scalar field u is required. In order to compute X, it is assumed that the velocity field has only minor variations in time and space, i.e:

$$v_j^{n+1} \approx v_j^n \ , \tag{2.49}$$

$$v_{j-1}^n \approx v_j^n \approx v_{j+1}^n \ , \tag{2.50}$$

where v_j^n is v_x at position x_j and time t^n. Under this assumptions, position X can be computed as:

$$X = x_j - v_j^{n+1}\Delta t \approx x_j - v_j^n \Delta t \ . \tag{2.51}$$

This approach is used to model the heat and solute transport advection-diffusion PDEs in this work due to its stability, the small numerical diffusion and not limiting the simulation time-step. Cubic spline interpolation is applied to interpolate u from grid points and calculate u_X^n. Considering advection to be the only physical process in the system, it can be concluded that $u_j^{n+1} = u_X^n$.

Heat and solute transport and alike many other processes in fluid dynamics, are advective and diffusive (equations (2.34), (2.36) and (2.39)). To solve these equations operator-splitting method is used and diffusion and advection equations are solved successively [77].

In order to simulate dynamics of a system, a two-dimensional numerical code in developed written in C++. Figure 2.5 shows the modular design of this code containing three main modules to deal with thermo-, hydro- and chemical processes. Different modules are coupled through fluid and rock properties. The pressure module has single and two-phase flow options alike the temperature module with LTE and LTNE options.

To increase the computational efficiency, Open Multi-Processing (OpenMP) is used to parallelize the shared memory. The simulations in this work are performed on the KRYPTON cluster of the Geodynamics/Geophysics Group of the Steinmann-Institute, University of Bonn. The simulation results are visualized using Gnuplot or ParaView.

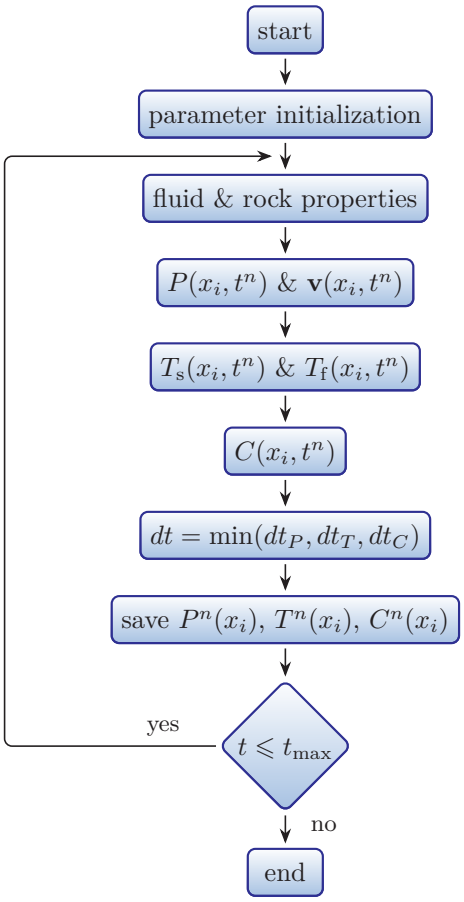

Figure 2.5.: Modular design of the developed code. The flow module can be switched between single and two-phase flow (for water-air systems using Richard equation). The computed velocity field in this part is used in heat and solute transport modules. Heat module contains both LTE and LTNE assumptions. dt is calculated at each time-step depending on the numerical stability criteria.

2.5. Validation of the developed numerical model

Due to a lack of experimental data in simultaneous heat, mass and fluid transfer, each module of the developed two-dimensional code is validated separately. Fluid flow in porous media is benchmarked by reproducing experimental results of Stanchits et al. [79] [80]. For validation of the mass transport module, the Henry seawater intrusion problem is solved. To benchmark the LTNE module, experiments done by of Zhao and Tso [81] are modelled numerically, following the parametrization derived by Zhao [82]. For the LTE module, the analytical solution of Ogata and Banks [83] is used.

2.5.1. Flow in unsaturated porous media

Stanchits et al. studied the fracturing of critically stressed sandstone samples due to fluid pressure [80]. Acoustic emissions were recoded during water injection into stressed Flechtingen sandstone specimens. The results show a clear correlation between induced fluid front and acoustic emissions and therefore it is used as a benchmark for fluid flow in saturated and unsaturated medium, in this work.

After loading, fluid was injected with 5 MPa into the undrained sample Fb28 from bottom. To model this experiment, stress dependent porosity and permeability are computed using equations (2.32) and (2.33). Parameters used for solving equation (2.28) are listed in table 2.1. Dirichlet Boundary condition is set for water pressure on the bottom boundary and Neumann condition for the rest. Measured pore pressure at top and bottom is shown in figure 2.6 together with the numerical results.

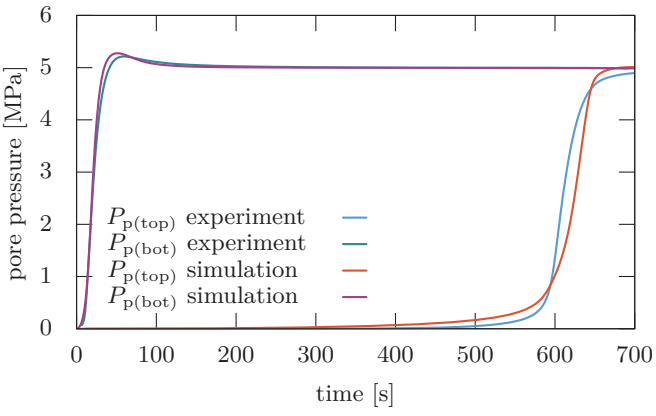

Figure 2.6.: Pore pressure at top and bottom of the unsaturated sample Fb28 during water injection. Simulation results are in good agreement with experiment.

2.5.2. Flow in saturated media

After full saturation of the specimen, injected water pressure was increased to 20 MPa in order to induce failure. Simulation results are compared with the laboratory measurements

symbol	description	value
dx_i	simulation resolution	$1\,\mathrm{mm}$
μ_a	air viscosity	$1.6 \times 10^{-5}\,\mathrm{Pa\,s}$
μ_w	water viscosity	$1.002 \times 10^{-3}\,\mathrm{Pa\,s}$
ρ_a	air density	$1.184\,\mathrm{kg\,m^{-3}}$
ρ_w	water density	$9.982 \times 10^{2}\,\mathrm{kg\,m^{-3}}$
ρ_r	rock density	$2.3 \times 10^{3}\,\mathrm{kg\,m^{-3}}$
β_a	air compressibility	$9.900 \times 10^{-6}\,\mathrm{Pa^{-1}}$
β_w	water compressibility	$4.219 \times 10^{-10}\,\mathrm{Pa^{-1}}$
ϕ_0	porosity at zero stress	0.095
ϕ_r	residual porosity	0.085
a	control parameter in equation (2.32)	$-8 \times 10^{-9}\,\mathrm{Pa^{-1}}$
k_0	zero stress permeability	$3.8 \times 10^{-16}\,\mathrm{m^2}$
b	control parameter in equation (2.33)	4
$S_\mathrm{w}^\mathrm{min}$	irreversible water saturation	0.01
$S_\mathrm{w}^\mathrm{max}$	maximum water saturation	0.99
n	control parameter in equations (2.23) and (2.24)	3.0
P_r	pressure scaling factor	$3.5 \times 10^{5}\,\mathrm{Pa}$
P_in	injection pressure	$5.7 \times 10^{6}\,\mathrm{Pa}$

Table 2.1.: Parameters used in validation of two-phase fluid flow in unsaturated sample Fb28.

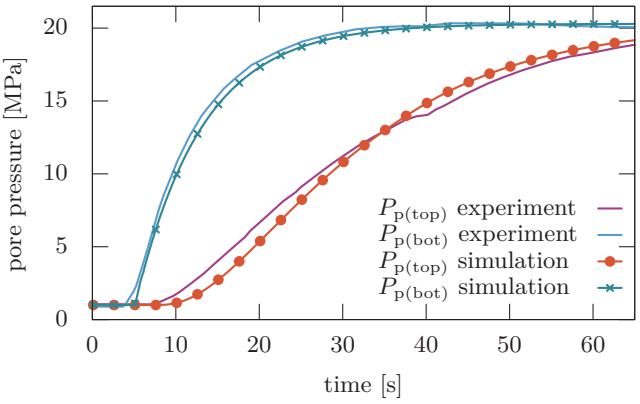

Figure 2.7.: Fluid injection pressure was increased after full saturation of sample Fb28. Simulated top and bottom pore pressure is well comparable with the experimental results of [80].

in figure 2.7. The kink in the experimental curves at about 40 s is due to the failure of the sample and hence not reproducible in the simulation.

2.5.3. Mass transport

To verify the density-dependent flow, the Henry problem is simulated. It describes saltwater diffusion in a homogeneous, isotropic, confined aquifer which is initially charged with freshwater. Flow of freshwater to the inland boundary occurs with a constant flux while the opposite boundary has a constant high density (figure 2.8) [84].

In this scenario, the longitudinal and transverse dispersivities are neglected. The applied parameters and boundary conditions are presented in table 2.2 [85].

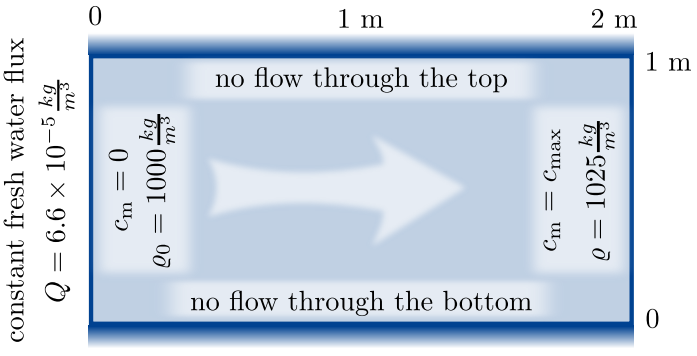

Figure 2.8.: set-up of the Henry problem. A constant flux of fresh water is applied to the system from left with a constant flux, while the opposite boundary is set as a high concentration saltwater [84]. Semianalytical solution for the steady state distribution of salinity is used widely as a benchmark for density flow models.

A semianalytical solution for the steady state distribution of concentration is presented by the Henry at 1964 [86]. This is modeled on a 20×10 grid and the steady state isochlor contours from Henry solution and simulation results are plotted in figure 2.9. Figure 2.10 shows the salinity map of the simulated steady state related to Henry problem.

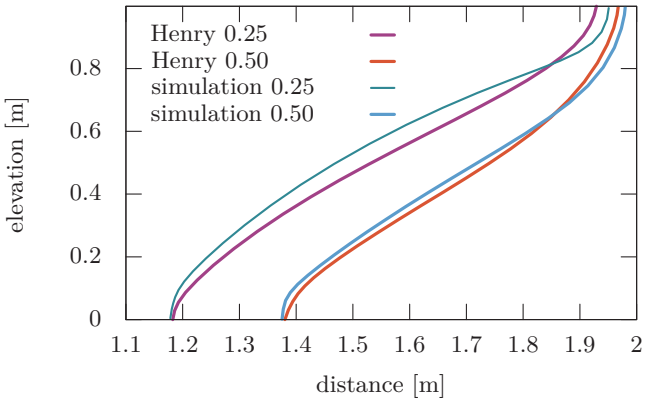

Figure 2.9.: Isochlor contours of steady state solution of Henry problem by [85] comparing to the simulation results.

parameter/boundary	description
porosity	ϕ=0.35
permeability	k=1×10^{-9} msq
fluid viscosity	μ=1×10^{-3} Pa s
molecular diffusion coefficient	d_m=1.886×10^{-6} m s^{-1}
dispersivity	$\alpha_t = \alpha_l$=0 m
equation of state	$\rho = \rho_0(1 + 200C)$
transport boundary conditions	ρ_0=1000 kg m^{-3} on the left boundary
	ρ_{max}=1025 kg m^{-3} on the right boundary
	$\nabla C = 0$ on top and bottom boundaries
fluid flow boundary conditions	constant flux of Q=6.6×10^{-5} kg m^{-3} at the left side
	hydrostatic pressure on the right boundary
	$\nabla P = 0$ on top and bottom boundaries

Table 2.2.: Parameters and boundary conditions used in the Henry problem [85]

2.5.4. Heat transport

The LTNE module is validated by reproducing experiment results of Zhao and Tso [81] numerically, following the parameterization derived in [82]. In these experiments water is injected into a single fracture in the middle of a low permeable rock of dimensions 51 mm × 102 mm. The input temperature T_{in} is measured as well as the output one T_{out}. Temperature on the top and bottom of the specimen is kept constant and the injected water velocity is known.

Parameters for heat transfer are taken from [82], though for two experiments no parameters

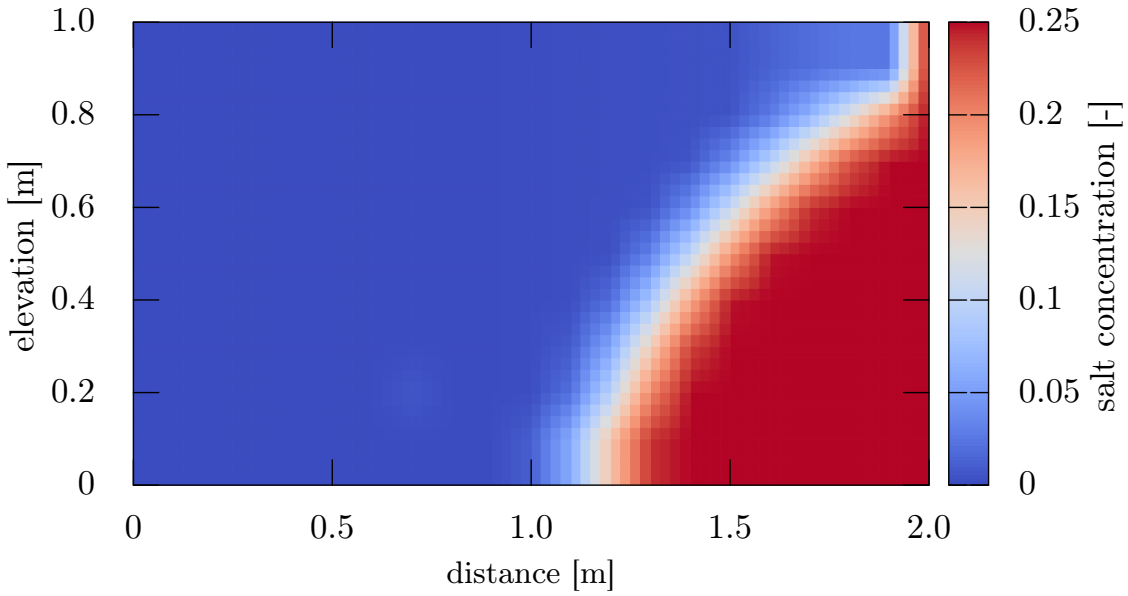

Figure 2.10.: Simulation results of the Henry problem model. The steady state is reached after about 120 min.

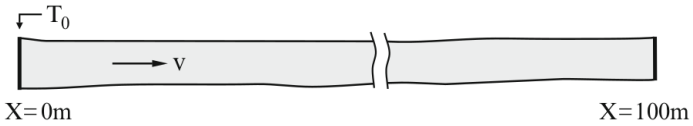

Figure 2.11.: Water flows into a fracture with constant flux and initial temperature of 0 °C. T_0 is set to 1 °C on the left boundary. Pressure on the right and left boundaries is constant [87].

are available. The numerical results of water outflow temperature (reported in table A.1), show good agreement to the experiments with simulated temperatures in a 1 °C window around measured values.

The LTE heat transport module is benchmarked with an analytical solution of a one-dimensional problem. Groundwater enters a fully saturated fracture ($\phi = 1$) with a constant velocity of $3 \times 10^{-7}\,\mathrm{m\,s^{-1}}$. The set-up is shown in figure 2.11 and modelled on a grid of 501 nodes. The parameters and boundary conditions used are listed in table 2.3.

Analytical solution of Ogata and Banks [83] for one-dimensional advective-diffusive transport is used to calculate the temperature breakthrough curve [87]. It is plotted in figure 2.12 together with the simulation results. Maximum error is 0.65% and occurs at about $t = 3.7 \times 10^8$ s.

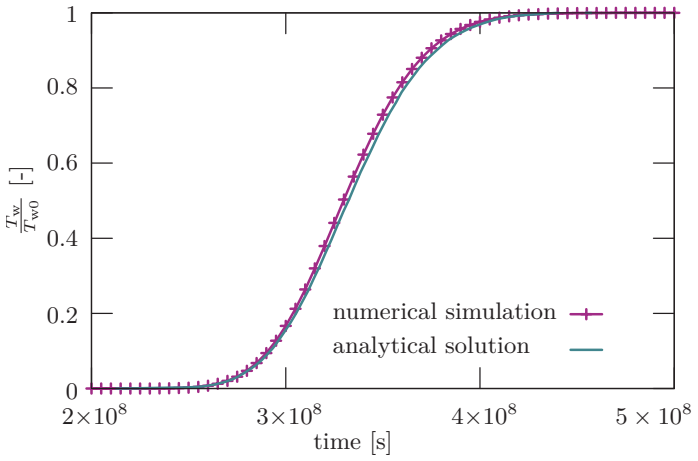

Figure 2.12.: Modelling the analytical solution with LTE module. Fluid temperature curve at position x =100 m.

parameter/boundary	description
fracture length	L =100 m
porosity	$\phi = 1$
water density	ρ_f=1000 kg^2 m^{-1}
thermal conductivity of water	K_f=0.6 W K^{-1}
heat capacity of water	c_{pf} =4000 J kg^{-1} K^{-1}
water velocity	$\mathbf{v}$ =3 × 10^{-7} m s^{-1}
LTE boundary condition	T_0 =1 °C on the left
	Neumann condition on the right border
fluid flow boundary condition	constant fluid flux Q =3 × 10^{-7} m^3 s^{-1} on the left
	constant pressure P =1 × 10^5 Pa on the right border
initial condition	P_{ini} =100 kPa
	T_{ini} =0 °C

Table 2.3.: Parameters and boundary conditions used in LTE heat flow in a porous medium [87]

In order to validate coupled heat transport and density variations of fluid, a one-dimensional test has been done following Kolditz et al. [87]. It is assumed that groundwater flows under a pressure difference of 1 kPa in a 5.2 m long porous medium.

The medium has initial temperature of 300 K and a constant temperature of 400 K is applied to one boundary. Fluid and solid parameters and boundary conditions used in this problem can be found in table 2.4.

The module is run once with ρ =1000 kg m^{-3}, once with ρ =900 kg m^{-3} and finally with variable density. For temperature- and pressure-dependent fluid density, the results of

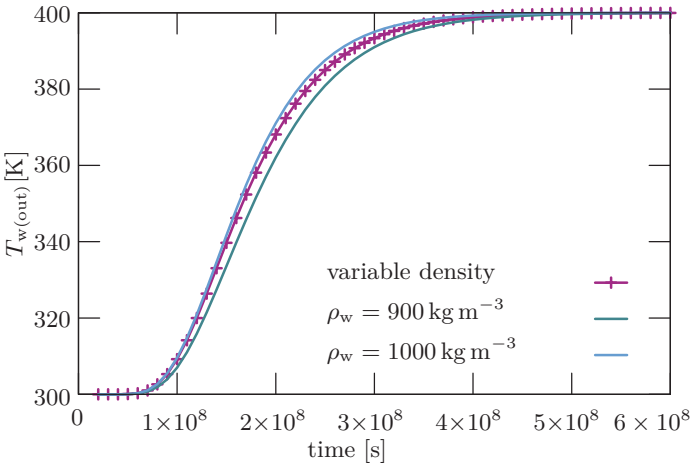

Figure 2.13.: LTE module is run aussuming constant densities of $900\,kg\,m^{-3}$ and $1000\,kg\,m^{-3}$ as upper and lower boundaries for a specific problem and once with variable density, as expected.

Sun et al. [88] are used. Simulated results in figure 2.13 shows that the temperature breakthrough curve assuming variable density, lays between upper and lower density-boundaries.

parameter	description
permeability	$k = 1 \times 10^{-11}\,m^2$
porosity	$\phi = 0.01$
rock density	$\rho_s = 2850\,kg^2\,m^{-1}$
heat capacity of rock	$c_{ps} = 1000\,J\,kg^{-1}\,K^{-1}$
thermal conductivity of rock	$K_s = 3.2\,W\,K^{-1}$
water density	$\rho_f = 1000\,kg^2\,m^{-1}$
water viscosity	$\mu = 1 \times 10^{-3}\,Pa\,s$
thermal conductivity of water	$K_f = 0.6\,W\,K^{-1}$
heat capacity of water	$c_{pf} = 4000\,J\,kg^{-1}\,K^{-1}$
LTE boundary condition	$T_0 = 400\,K$ on the left
	Neumann condition on the right border
fluid flow boundary condition	$P_0 = 101\,kPa$ on the left
	$P = 100\,kPa$ on the right border
initial condition	$P_{ini} = 100\,kPa$
	$T_{ini} = 300\,K$

Table 2.4.: Parameters and boundary conditions used in LTE heat flow coupled with density variaions [87].

3. Numerical study of asymmetric vertical fluid intrusion in deep reservoirs: effects of pressure, temperature and salinity

Non-symmetric upward and downward pressure diffusion from the point of injection is an often observed phenomenon in fluid-triggered seismicity. In recent studies, diverse sets of models are used to describe this phenomenon; most commonly by applying a stress- and pressure-dependent permeability resulting in a depth-dependence of permeability. However, large permeability changes over the limited spatial scales around the injection point may be unrealistic. An alternative possible source of non-symmetric diffusion is variations in fluid properties with depth, particularly because this phenomenon is observed in regions with significant geothermal gradients. A temperature gradient or changes in salinity with depth results in density contrasts that affect buoyancy and viscosity contrasts that affect the hydraulic diffusivity.

In this work, we study these processes separately to identify to what extent each may result in non-symmetric diffusion. We perform one-dimensional simulations using either water as the stimulating fluid. We find that over short time scales, stress-dependent permeability has the strongest influence on non-symmetric diffusion processes, while temperature effects become more important over longer time scales. Salinity plays only a very minor role. Pressure diffusion asymmetry is amplified when both temperature and stress influences occur simultaneously.

Our results indicate the importance of coupling heat flow and fluid flow when simulating fluid injection in regions with high geothermal gradients because fluid motion is influenced by the temperature of the host system even over short time scales.

3.1. Introduction

Fluid pressure as a seismic trigger is a well-known phenomenon and often observed in natural and artificial hydro-thermal systems. Fluid pressure as a trigger for swarm seismicity can occur during geologic CO_2 sequestration, in geothermal systems, and for hydraulic fracturing of tight shales. Often the fluid source can be approximated as a point source from which the fluid pressure diffuses. While considering the radial distance of seismic events from the injection point, it can be shown that fluid diffusivity is most often larger upwards than downwards. This effect has been studied in detail and quantified by [89] for the 2008 Bohemian swarm in which the up-dip diffusivity is around three times larger than the down-dip value. Although not studied in detail, the same effect can also be seen during the injection at the geothermal field Basel 1 [4, 20], at Fenton Hill [90], at the continental deep drilling project KTB [91], the 2010 Yellowstone swarm [3], the main Marmara Fault in Turkey [92], and in the East African Rift [93]. Certainly more examples will be found.

Existing models typically include a pressure dependent permeability where high permeability gradients at depths of a few kilometers can explain upward migration of seismicity. Although a pressure-dependent permeability does result in non-symmetric diffusion, the permeability variations appear exaggerated over the limited spatial scale of the observations. This raises the question of whether other processes are in play when more realistic permeability gradients are used.

In this work, we study the contributions and interplay of three physical processes that may also influence vertically asymmetric pressure diffusion: stress, temperature and mass transport. All of these vary with depth or change the fluid properties, and can therefore cause non-symmetric diffusion. Obviously permeability and porosity depend on the stress state and the fluid pressure, and hence influence pressure diffusivity. In addition, steep temperature gradients, particularly in hydro-thermal systems, can affect fluid buoyancy, while CO_2 rising from deeper origins carries with it a higher temperature than the host system. Salinity contrasts also influence buoyancy. For instance, the injected fresh water during stimulation of an enhanced geothermal field, has a salinity that could be orders of magnitude lower than the existing pore fluid.

For simplicity, we consider a one-dimensional profile of a saturated homogeneous rock from 2 km to 6 km depth with hydrostatic pressure. Pressure diffusion is simulated while water is injected into the system with constant overpressure of 10 MPa at 4 km depth over a period of 6 months.

In a homogeneous system where rock permeability, porosity and temperature as well as fluid density and viscosity are constant over the simulation zone, and the injected water has the same temperature as the host rock, fluid pressure diffuses symmetrically. In other words, upward and downward flow are identical under hydrostatic pressure.

We chose water as the intruding fluid because it is generally the triggering fluid in hydrothermal systems. We will later discuss how the results can be interpreted with respect to supercritical CO_2 as a trigger for natural seismicity. All other parameters are set based

on observations mentioned above. We believe this model is sufficient to draw general conclusions.

We developed a numerical model that has three coupled modules for fluid flow, heat, and mass transport processes. The fluid flow module is benchmarked by laboratory results of Stanchits et al. [80, 79], and the heat transport module is benchmarked with the analytical solution for one-dimensional advective-diffusive heat equation by Ogata and Banks [83]. The developed two-dimensional module to simulate density flow due to salinity, is benchmarked with Henry problem [94], and a one-dimensional version of this module is adapted for this work.

Fluid flow in a heterogeneous saturated porous medium is described by nonlinear pressure diffusion:

$$S\frac{\partial P}{\partial t} + \nabla \cdot \left(-\frac{k}{\mu} \left(\nabla P - \rho \mathbf{g} \right) \right) = 0 \ , \tag{3.1}$$

where S, P, k, μ, ρ and $\mathbf{g}$ are rock storativity, fluid pressure, rock permeability, fluid viscosity and gravitational acceleration, respectively. The storativity depends on rock porosity as:

$$S = \phi\beta_{\mathrm{f}} + (1-\phi)\beta_{\mathrm{s}} \ . \tag{3.2}$$

β_{f} and β_{s} are fluid and rock compressibilities and ϕ is the porosity. Darcy velocity $\mathbf{q}$ is calculated from fluid pressure as:

$$\mathbf{q} = \frac{-k}{\mu} \left(\nabla P - \rho \mathbf{g} \right) \ . \tag{3.3}$$

Heat transport derives from conservation of energy, and we assume local thermal equilibrium. That is, rock and fluid reach thermal equilibrium immediately and $T_{\mathrm{f}} = T_{\mathrm{s}} = T$ with T_{f} and T_{s} temperature of fluid and solid phases, respectively. This leads to a single diffusion-advection equation for the system [95]:

$$\rho c_{\mathrm{p}} \frac{\partial T}{\partial t} + \phi \left(\rho c_{\mathrm{p}} \right)_{\mathrm{f}} \mathbf{v} \nabla T - K \nabla^2 T = 0 \ . \tag{3.4}$$

Specific heat capacity multiplied by density ρc_{p} and thermal conductivity K of the fluid-solid system are weighted by porosity:

$$\rho c_{\mathrm{p}} = \phi \left(\rho c_{\mathrm{p}} \right)_{\mathrm{f}} + (1-\phi) \left(\rho c_{\mathrm{p}} \right)_{\mathrm{s}} \ , \tag{3.5}$$

$$K = \phi K_{\mathrm{f}} + (1-\phi) K_{\mathrm{s}} \ . \tag{3.6}$$

Here subscripts s and f are used for solid and fluid phases, respectively. $c_{\mathrm{p}\alpha}$ is the heat capacity of the fluid or solid phase. The real fluid velocity $\mathbf{v}$ used in the advective term, is related to Darcy velocity as $\mathbf{q} = \phi\mathbf{v}$. We neglect heat sources, viscous dissipation effects and thermal expansion effects.

The effect of density contrasts between the intruding fluid and the initial pore fluid is studied by assuming a different salinity of the injected fluid relative to system. Considering

a homogeneous dispersion and porosity, mass transport is expressed as a linear diffusion-advection equation for salt concentration:

$$\frac{\partial C}{\partial t} + \mathbf{v} \cdot \nabla C - d_{\mathrm{m}} \nabla^2 C = 0 \ . \tag{3.7}$$

C is salt concentration and d_{m} is the molecular diffusion coefficient [85].

We model the one-dimensional diffusion processes using second order FTCS (Forward-Time Central-Space) scheme, while a second order Semi-Lagrangian scheme is used for the advection terms. We use a numerical resolution of 100 grid points resulting in a grid spacing of 40 m. Zero flux boundary conditions are set for pressure, temperature and mass fraction.

3.2. Impact of stress

Here we investigate stress effects on asymmetric diffusion. Usually, effects of stress and pressure on diffusion processes are introduced in the physical model by considering the permeability or porosity as stress dependent. This dependence could be an exponential or a power law relationship. Various studies follow David et al. [67], (for instance [1, 96, 68, 16]) use an exponential form of permeability dependent on effective normal stress. Other studies use a power law for permeability [66] or diffusivity [97, 98]. Other studies [16, 69, 70, 71] use an exponential equation for porosity depending on effective mean stress σ'_{M} and consider permeability changes with porosity variations using an exponential relation:

$$\phi = \phi_{\mathrm{r}} + (\phi_0 - \phi_{\mathrm{r}})\, exp\left(a \cdot \sigma'_{\mathrm{M}}\right) \ , \tag{3.8}$$

$$k = k_0 \ exp\left[b\left(\frac{\phi}{\phi_0} - 1\right)\right] \ , \tag{3.9}$$

where ϕ_r is residual porosity, ϕ_0 and k_0 are porosity and permeability at zero stress and a and b empirical control parameters, respectively.

We use equations (3.8) and (3.9) to examine non-symmetric diffusivity due to pore pressure changes. The parameters chosen are similar to Rutqvist et al. [69] (table 3.1) such that density and viscosity at the injection point are comparable with section 3.3 where temperature effects are studied. Porosity declines slightly more than 2% over 4 km depth with an average value of 5% as shown in figure 3.1(c). Permeability decreases about 50 times from $2.3 \times 10^{-13}\,\mathrm{m}^2$ to $5 \times 10^{-15}\,\mathrm{m}^2$ over 4 km depth (figure 3.1(b)). This permeability gradient is still large compared to laboratory data of Dong et al. [65] for sandstone, however other studies utilise even stronger gradients to explain recorded seismic data. Dong et al. show that the permeabilities of the sandstone samples remain between $1 \times 10^{-13}\,\mathrm{m}^2$ and $1 \times 10^{-14}\,\mathrm{m}^2$ while confining pressure increases from 3 to 120 MPa [65].

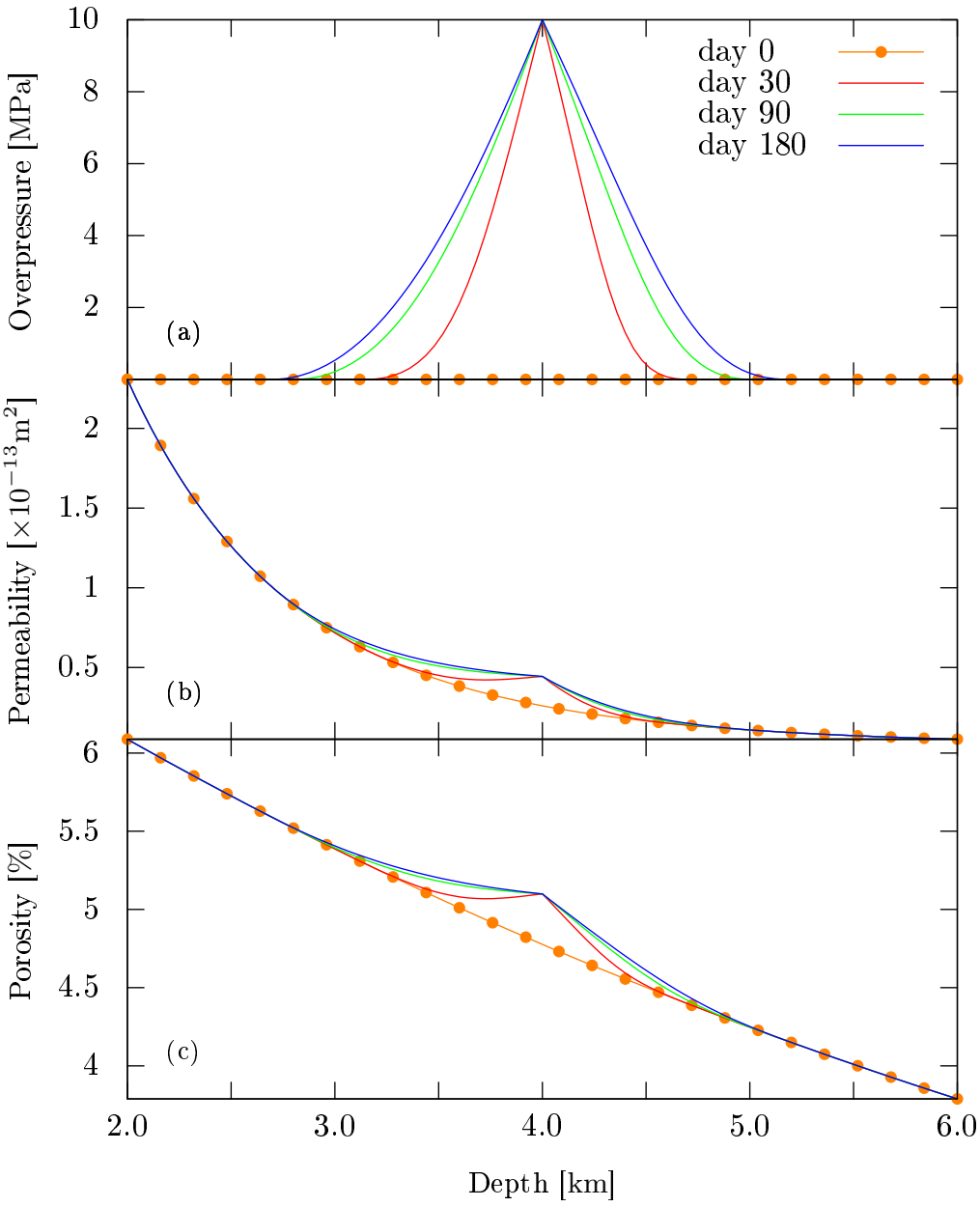

Figure 3.1.: Porosity is a nonlinear function of effective stress and permeability depends on porosity. The parameters are chosen in a way that the mean porosity and permeability are the same as in the rest of the study, i.e. 0.05 and $5 \times 10^{-13}\,\mathrm{m\,s^{-1}}$ respectively.

symbol	quantity	value	unit
ϕ_0	zero stress porosity	0.078	-
ϕ_r	residual porosity	0.01	-
a	exponent constant in equation (3.8)	-8×10^{-9}	-
k_0	zero stress permeability	$4{\times}10^{-12}$	m^2
b	exponent constant in equation (3.9)	13	-
ρ_f	fluid density	920	$\mathrm{kg\,m^{-3}}$
μ	fluid viscosity	$2.5{\times}10^{-4}$	$\mathrm{Pa\,s}$
β_f	fluid compressibility	10^{-10}	$\mathrm{Pa^{-1}}$
β_s	pore compressibility	10^{-8}	$\mathrm{Pa^{-1}}$

Table 3.1.: Parameters used in section 3.2 to study influence of the stress-dependent permeability and porosity on vertical pressure diffusion.

The numerical experiment is run for 180 days of injection with constant pressure of 10 MPa. Figure 3.1(a) shows the overpressure at four stages. It is evident that the upward diffusion occurs faster than the downward direction, particularly after one month of injection. Lower porosity in the deeper levels leads to larger storativity, considering that water compressibility is negligible compared to pore compressibility (table 3.1 and equation (4.3)). This compensates the smaller permeability values to some extent and can explain the faster expansion of the downward pressure P_d after 180 days.

3.3. Impact of temperature

A temperature gradient in the system influences density and viscosity of the fluid. On the one hand, depending on the injected fluid temperature, it causes buoyancy driven flow that is inherently anisotropic. On the other hand, changing viscosity makes the diffusivity in equation (3.1) inhomogeneous and the diffusion nonlinear.

In order to investigate the influence of temperature, we assume permeability and porosity to be constant and we choose the values similar to the injection point values in the previous section. Temperature at the top boundary is set to 70 °C and with a temperature gradient of $35\,\mathrm{K\,km^{-1}}$, the lower boundary is set to 210 °C. Other parameters used in this section are presented in table 3.2. Injected water has a temperature equal to the system at the injection depth of 4 km.

We use temperature dependent density $\rho(T)$ and viscosity $\mu(T)$ following Huyakorn and Pinder [99], which are plotted in part (b) of figures 3.2 and 3.3 in the range used in this work. To examine the effects of $\rho(T)$ and $\mu(T)$ independently, we run the simulation once with constant $\mu = 0.2 \times 10^{-3}\,\mathrm{Pa\,s}$ and once with $\rho_\mathrm{f} = 920\,\mathrm{kg\,m^{-3}}$.

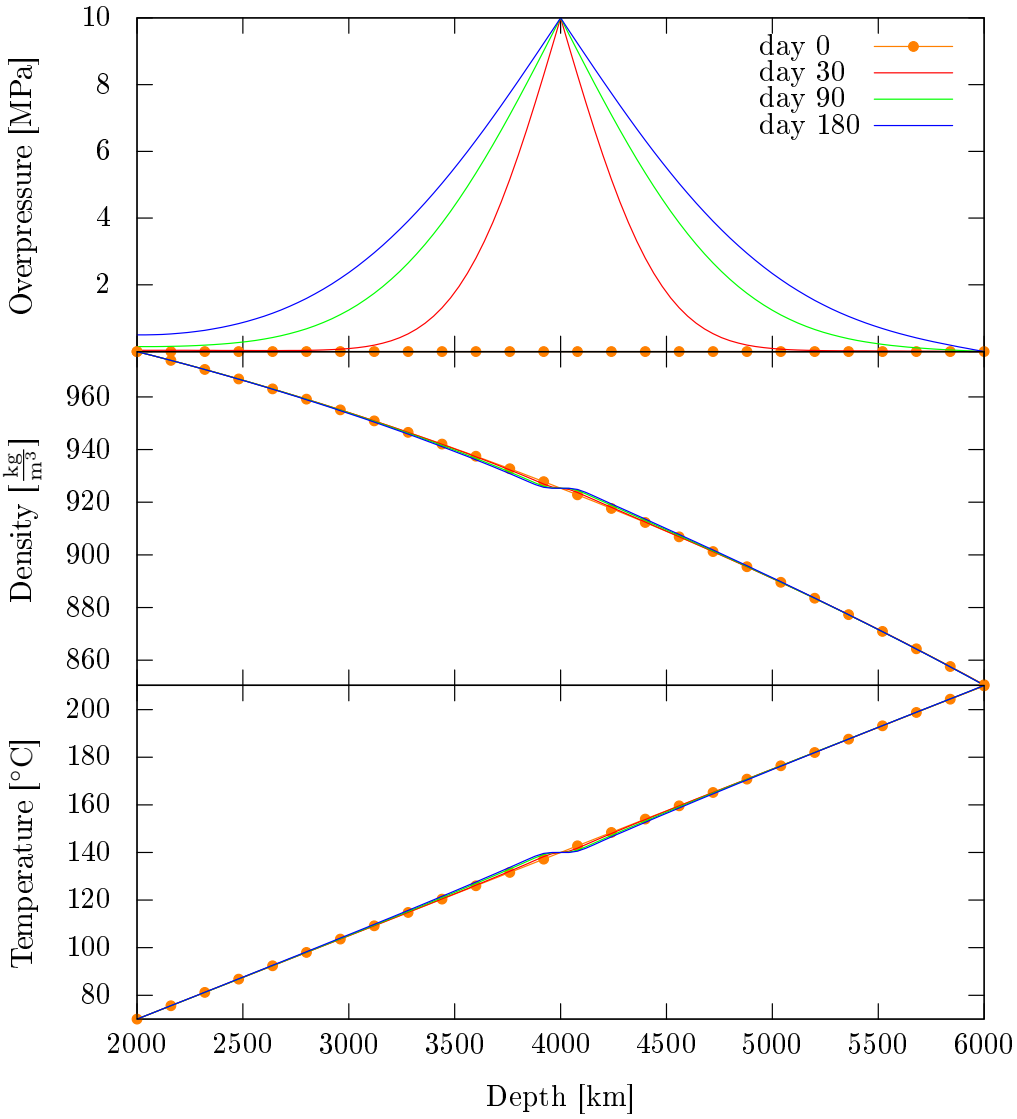

Figure 3.2.: Temperature gradient effect on density while fluid viscosity is constant. Temperature of injected water is the same as injected point. Difference of overpressure at top and bottom boundaries reaches to 1.4 MPa after 6 months.

Figure 3.2 shows the numerical result of variable density and constant viscosity. Compared with the initial configuration, temperature increases above the injection point and decreases beneath the injection point due to the intrusion. As expected, heat transfer is slower than pressure diffusion and limited to about 170 m at the end of the simulation time.
This can explain the delayed buoyancy effect due to temperature gradients. While permeability changes due to stress propagates quickly, temperature driven buoyancy spreads slowly. Pressure diffusion occurs asymmetrically and the difference between top and bottom pressure grows with time from a negligible difference after 30 days to 0.7 MPa after 180 days of simulation time.

symbol	quantity	value	unit
ϕ	porosity	0.05	-
k	permeability	10^{-13}	m^2
T_{top}	temperature at top boundary	70	°C
∇T	temperature gradient	35	$K\,km^{-1}$
c_{pr}	rock heat capacitance	1000	$J\,kg^{-1}\,K^{-1}$
K_r	rock thermal conductivity	3.2	$W\,m^{-1}\,K^{-1}$
ρ_r	rock density	2850	$kg\,m^{-3}$
c_{pf}	fluid heat capacitance	4200	$J\,kg^{-1}\,K^{-1}$
K_f	fluid thermal conductivity	0.6	$W\,m^{-1}\,K^{-1}$

Table 3.2.: Parameters used in section 3.3 to study effect of temperature gradient on vertical pressure diffusion.

We also perform simulations for variable viscosity and constant density. Fluid viscosity decreases with increasing temperature and therefore pressure diffusivity is higher below the injection point (equation (3.1)). The viscosity and density have obviously opposite effects on fluid diffusion. The results are shown in figure 3.3. At the end of the simulation time the overpressure of the bottom boundary is about 0.7 MPa higher than the top one.

Furthermore, heat transfer experiments are performed considering simultaneous viscosity and density changes. Figure 3.4(a) and (d) show the overpressure and temperature field, respectively. P_d is slightly higher than the upward pressure P_u after 30 and 90 days. However, buoyancy overcomes viscosity after 180 days of simulation and the overpressure at the top boundary is about 0.1 MPa higher than the bottom one.

Up to this point, we have assumed that the injected fluid has the same temperature as the system at the injection point. In reality however, this is not always the case. If the intrusion occurs from below, the injected fluid has often a higher temperature as the system (e.g. [100]), which causes a stronger buoyancy effect. Therefore, we consider a scenario with variable density and viscosity, where the injected fluid has a constant temperature of 200 °C. Other fluid and rock parameters are kept constant as shown in table 3.2. Figure 3.5 shows the changes in the overpressure field, density, viscosity and fluid temperature in time.

The low viscosity in the high temperature region results in a higher pressure diffusivity compared to figure 3.5. Hence, the region with increased temperature is extended over 500 m after 180 days.
Through viscosity effects, P_d is again slightly higher than P_u, after 90 days of injection. Temperature front spreads slowly and buoyancy has overcome viscosity effects after 180 days. The upward and downward pressure difference grows to 0.1 MPa at the end of the simulation time.

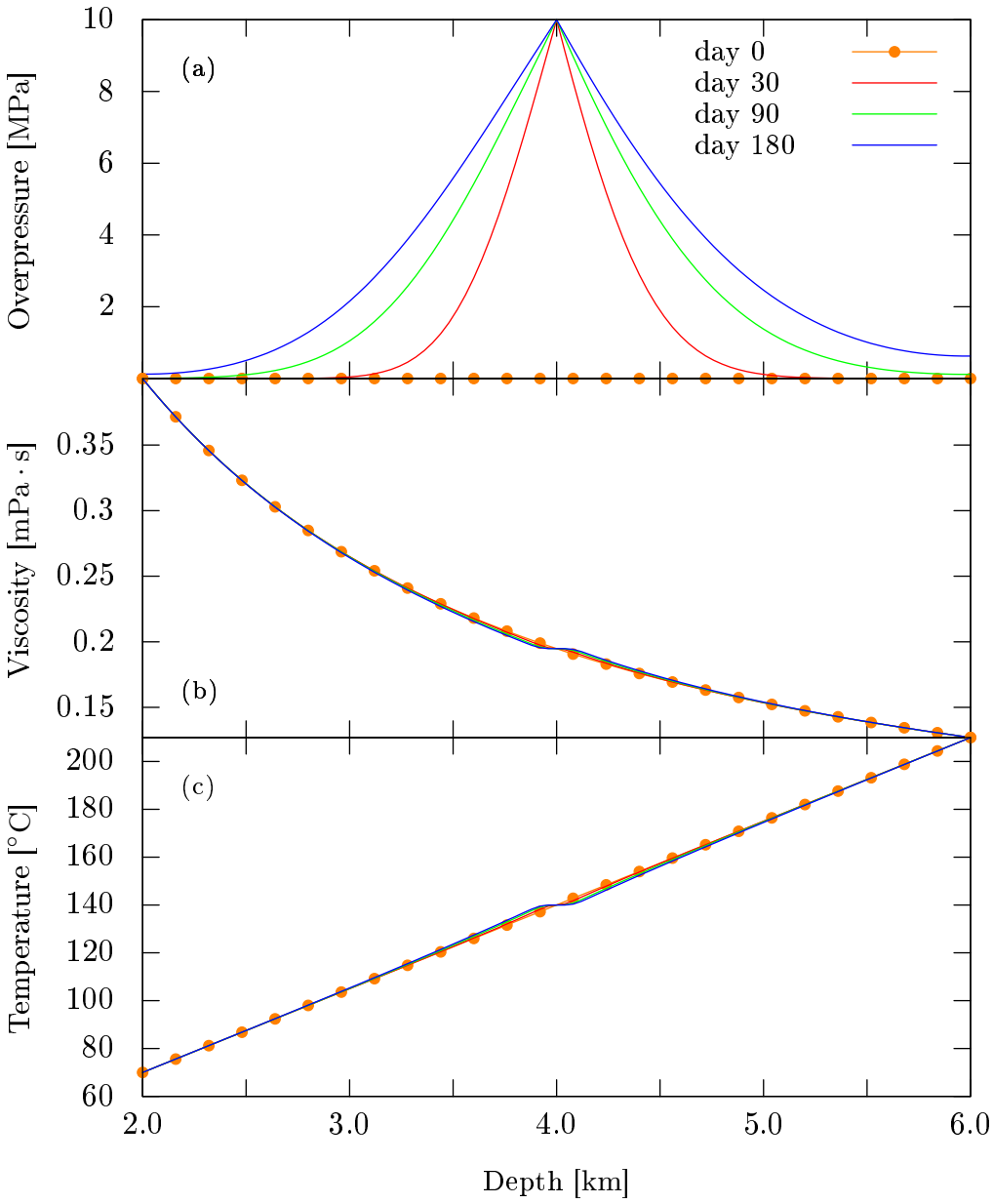

Figure 3.3.: Temperature gradient effect on viscosity while fluid density is constant. Because of lower viscosity beneath the injection point, diffusivity is higher towards bottom.

If we assume that T_{in} is lower than the pore fluid temperature like in enhanced geothermal systems, viscosity contrasts and buoyancy affects in the same direction and P_{d} is higher than P_{u}.

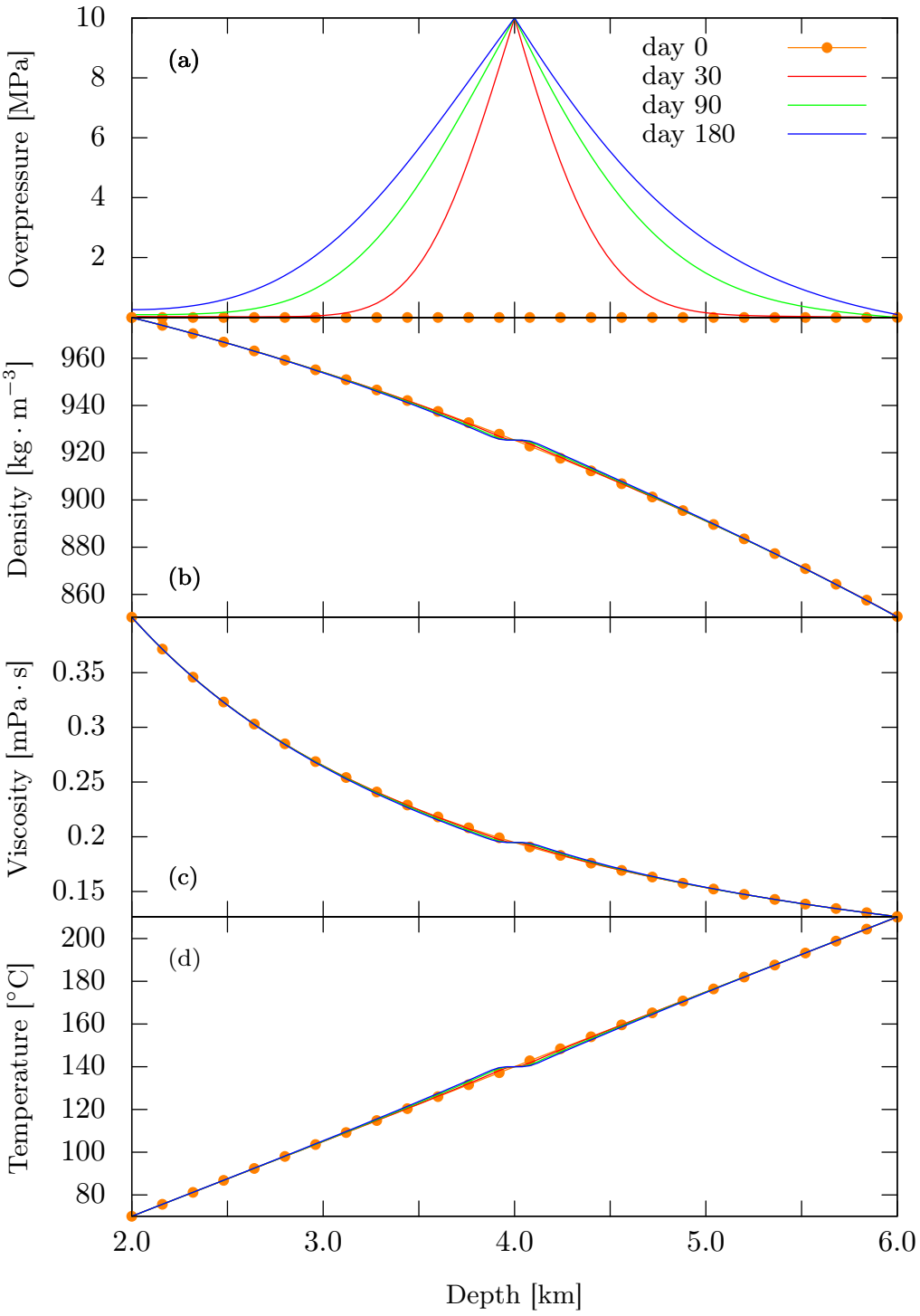

Figure 3.4.: Assuming that T_{in} has the same temperature as the system at injection point. The system cools down at the top of injection point and warms up beneath this. At the end of the simulation time, overpressure at top is significantly higher than bottom.

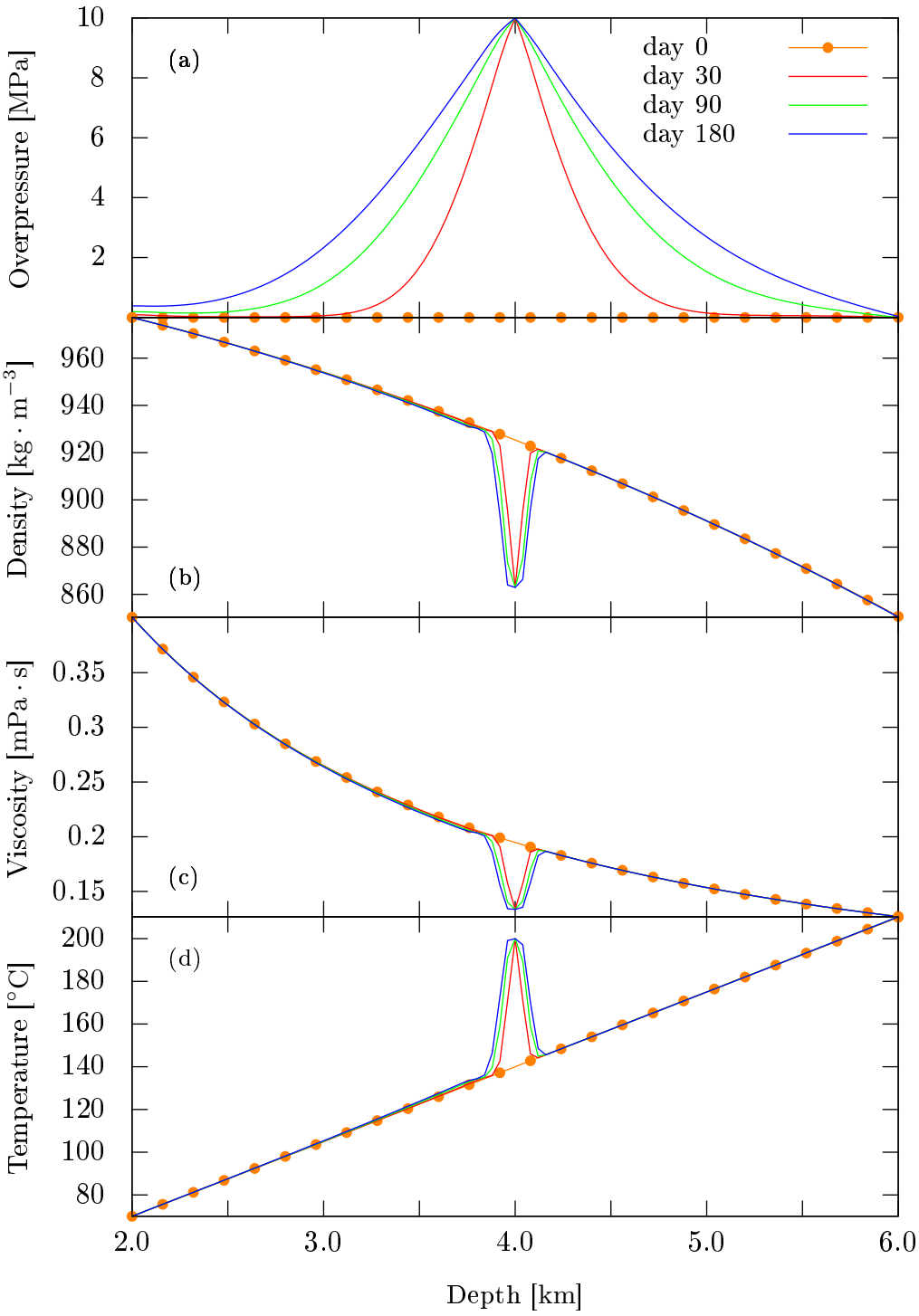

Figure 3.5.: Assuming that T_{in} is higher than the temperature at injection point, buoyancy effect is much stronger and the top and bottom pressure difference after 6 months of simulation, reaches to 2.4 MPa.

3.4. Impact of salinity

Section 3.3 shows the importance of buoyancy effects in non-symmetric fluid diffusion. In addition to temperature, salinity contrasts can cause fluid density gradients. To examine the influence of salinity on asymmetric fluid diffusion we assume fresh water with salt concentration of $C_{\text{in}} = 0.1\,\text{kg}\,\text{m}^{-3}$ is injected into the system.

Initial concentration is assumed as $C_0 = 50\,\text{kg}\,\text{m}^{-3}$. Fluid density depends on salt concentration through:

$$\rho = \rho_0(1 + \varepsilon C) \ , \tag{3.10}$$

where ρ_0 is a reference fluid density and ε the density coefficient [94]. Table 3.3 shows the simulation parameters used here. To model this, we simulate the coupled equations (3.1) and (3.7) over 6 months of injection. Simulation results (figure 3.6) show that the low concentration region is over 1.7 km wide after 180 days, while the overpressure remains almost symmetric.

The intruding fluid can also have a higher salinity comparing to the system. In this case, the buoyancy effect leads to higher downward pressure.

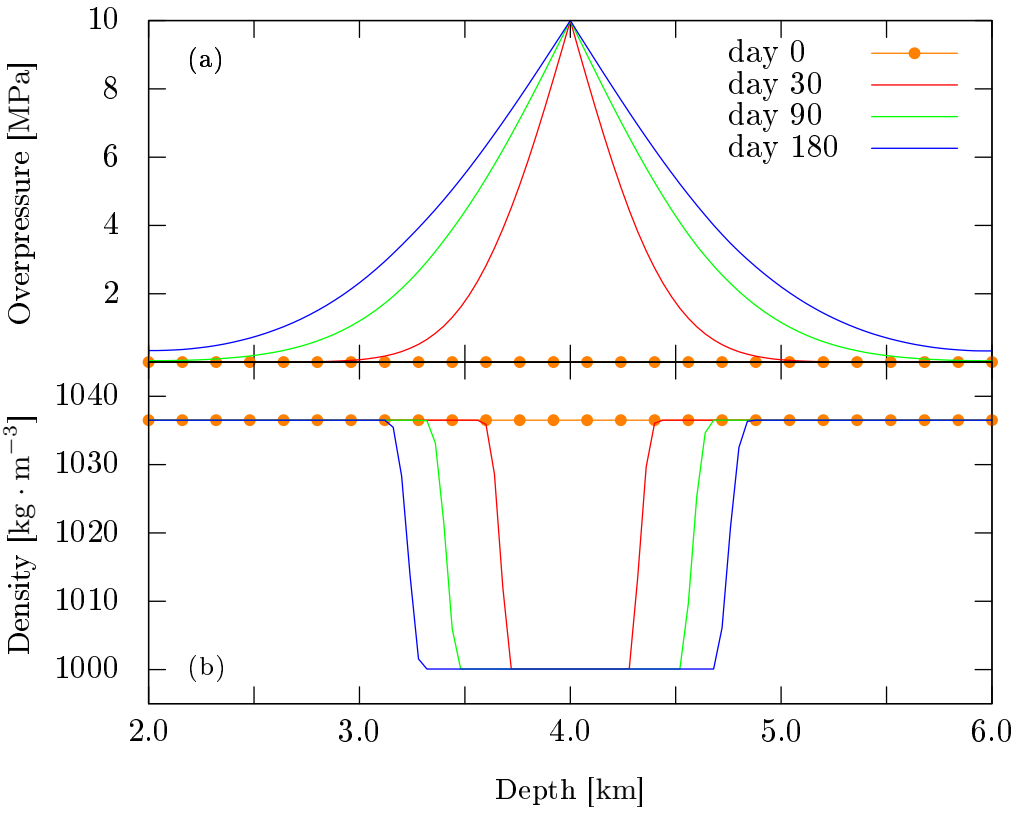

Figure 3.6.: Salinity of the injected water is less than the pore fluid, hence the upward fluid front is slightly faster than downward.

symbol	quantity	value	unit
ϕ	porosity	0.05	-
k	permeability	10^{-13}	m^2
μ	fluid viscosity	2.5×10^{-4}	Pa s
ρ_0	reference water density	1000	$kg\,m^{-3}$
ε	density dependence coefficient	7.3×10^{-4}	$m^3\,kg$
d_m	salt dispersion coefficient	6.6×10^{-6}	$m^2\,s^{-1}$

Table 3.3.: Parameters used in section 3.4 to model influence of density flow due to salinity on vertical pressure diffusion. d_m and ε are set after [94].

We simulated this scenario for $C_{in} = 50\,kg\,m^{-3}$ and initial concentration of $C_0 = 0.1\,kg\,m^{-3}$. The numerical results (figure 3.7) show again no significant difference at top and bottom overpressure.

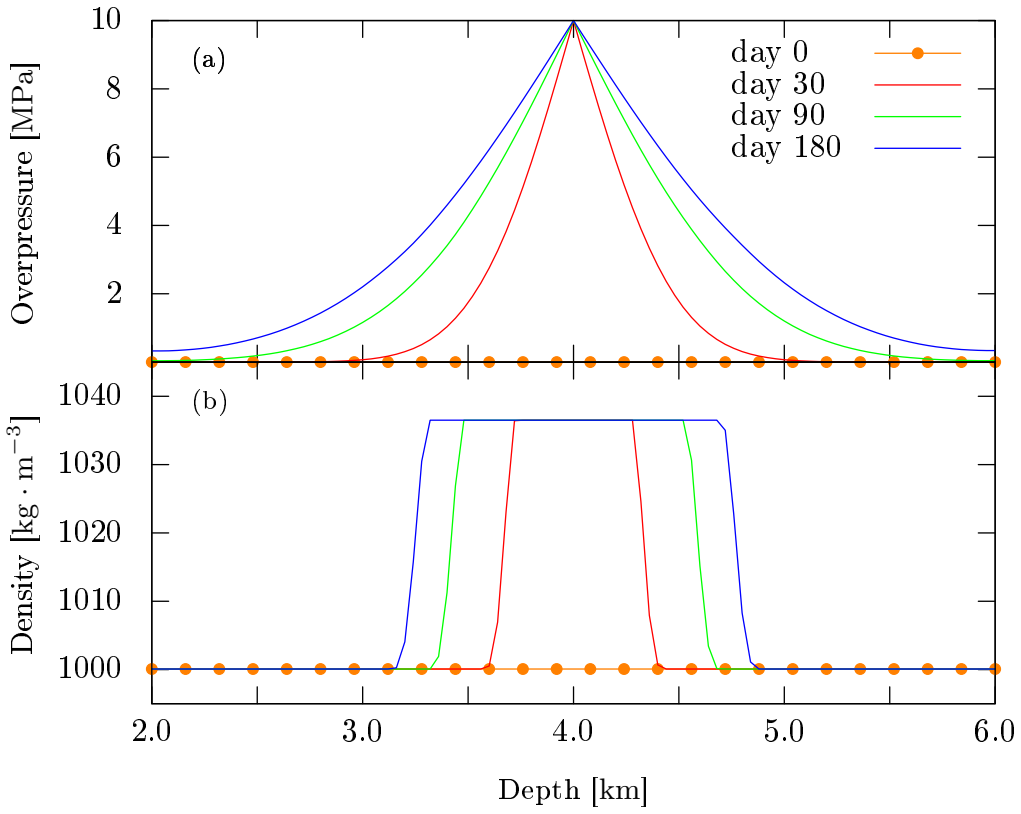

Figure 3.7.: Salinity of the injected water is higher than the system and the fluid front moves faster towards bottom.

3.5. Discussion

We studied the influence of different physical processes on asymmetrical fluid diffusion with depth. In order to summarise the impacts of these processes, we divide the simulated area in two parts and plot the upward and downward diffusion versus distance to the diffusion source. The result is illustrated in figure 3.8 at three different simulation stages. Considering the effect of temperature gradient, we choose the scenario in which the injected water has 200 °C. The salinity curve is related to the scenario of fewer salt concentration in the intruding fluid compared with the initial system.

We observe that the stress factor which affects permeability and porosity, is the dominant source for asymmetrical diffusion. The effectiveness decreases with time and at the end of the simulation time (figure 3.8c) P_{d} is even higher than P_{u} near the injection point. As discussed in section 3.2, this occurs because of the opposing roles of permeability and storativity in pressure diffusivity.

Temperature curves show a competition between viscosity and density changes. Since the temperature front moves slower than pressure front, in earlier stages P_{d} is higher than P_{u} (figure 3.8a). Density driven flow cannot overcome the viscosity effect until 90 days that P_{u} becomes slightly higher than P_{d} in the vicinity of the injection point. At the end of the simulation time, P_{u} curve crosses P_{d} at the distance of about 0.65 km from the injection point. This provides an estimation of the thermal buoyancy front velocity that is about $3.5\,\mathrm{m\,s^{-1}}$ in this case.

Density flow due to salinity causes a minor difference between upward and downward fluid flow, yet this difference grows with time and after 180 days, the difference between P_{u} and P_{d} is comparable with thermal buoyancy contribution.

We studied the individual effects of stress, heat and mass transport. Because of complexity of temperature and stress effects, we investigate combination of these two and neglect salinity. We model a scenario in which hot water is injected to a system in the presence of permeability and temperature gradients. Temperature of input water is 200 °C and the permeability and porosity changes as well as thermal parameters are chosen as sections 3.2 and 3.3.

Figure 3.9 shows the resulting overpressure diffusion in three different time-steps. We observe that the upward pressure front is faster after 30 days and 90 days. Afterwards, the propagation speed of the upward and downward pressure fronts are almost equal. To evaluate the asymmetry of the diffusion, we plot the overpressure versus distance to injection point in figure 3.10. It can be seen that combining temperature and stress effects make upward pressure to be always larger than downward. The maximum difference between P_{u} and P_{d} occurs after about 90 days of injection.

For simplicity, we used water as the flowing fluid, but it has been shown that in many cases (e.g. [101, 102, 93, 1, 103], etc.), supercritical CO_2 or a CO_2–H_2O mixture is responsible for triggering seismicity. The fluid flow in this condition is comparable since compressibility of CO_2 is about ten times higher than water and the viscosity is in the same order less [1]. On

the other hand, density of CO_2 in the temperature and pressure range used here, is much less than of water [104] and the density is much more

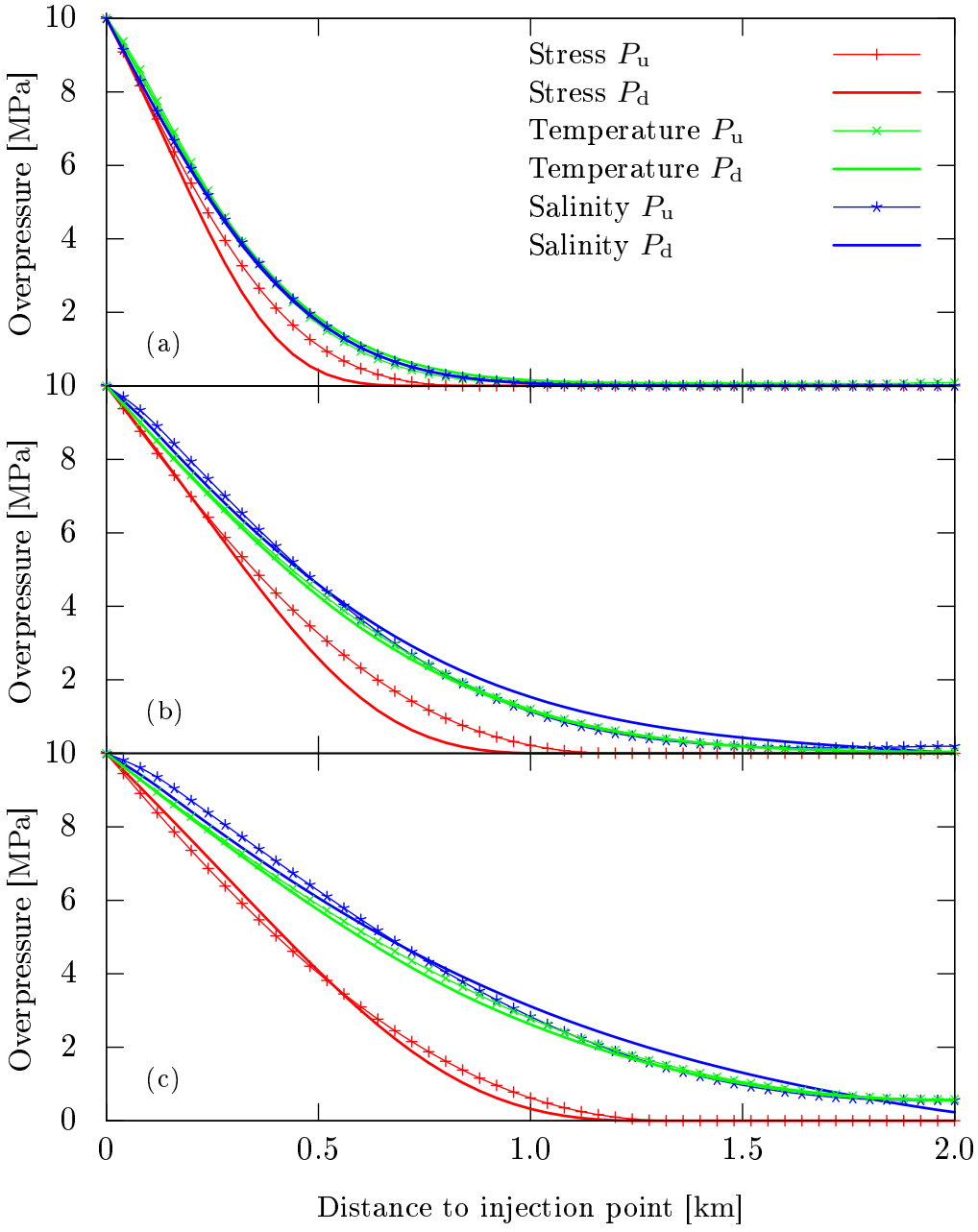

Figure 3.8.: Upward and downward overpressure due to stress effects on permeability, temperature gradient effects on density and viscosity, and finally density flow at (a) t=30 d, (b) t=90 d and (c) t=180 d.

sensitive to temperature changes. This results in an even faster upward fluid diffusion as calculated in this work and a stronger dominance of buoyancy effects.

We also assume a fully saturated environment. In the case of an unsaturated host rock the pressure diffusion equation can be altered, e.g. with the Richards approximation [62]. Darcy velocity, equation (3.3), can be rewritten for each phase as:

$$\mathbf{q}_\alpha = \frac{-k_0 k_{\mathrm{r},\alpha}(S_\alpha)}{\mu_\alpha} \left(\nabla P_\alpha - \rho_\alpha \mathbf{g}\right) \ , \tag{3.11}$$

with α as liquid or gaseous phase, k_0 intrinsic permeability, $k_{\mathrm{r},\alpha}$ scalar relative phase permeability as a function of phase saturation S_α, μ_α viscosity, P_α pressure and ρ_α density of phase α respectively [56].

$k_{\mathrm{r},\alpha}(S_\alpha)$ is defined via the van Genuchten relationships [55] and changes between 0 and 1. Based on a saturation-dependent permeability, an initial non-symmetric distribution of saturation could cause non-symmetric diffusion. In general, water content increases with depth. Therefore, such a non-symmetric distribution, besides gravitational effects, would cause a faster pressure diffusion downwards.

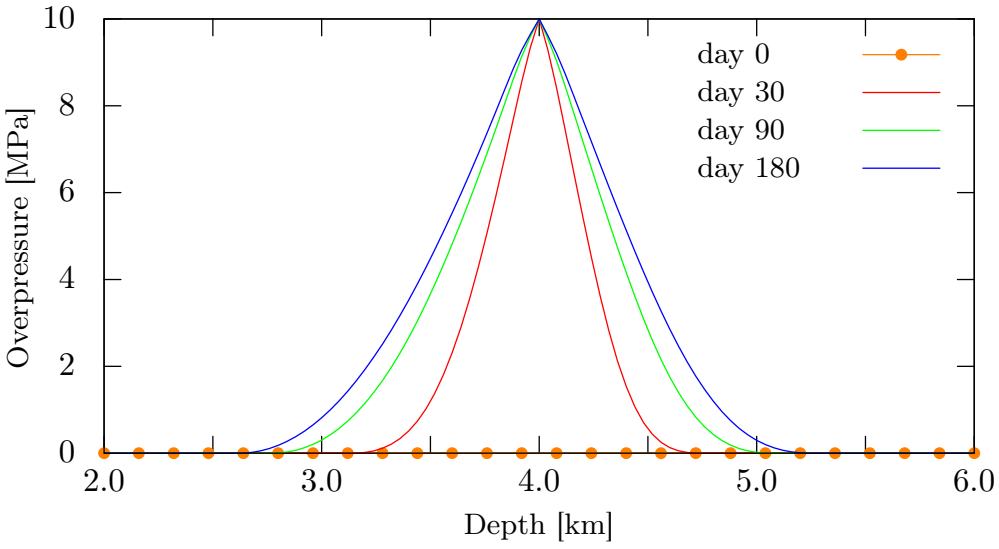

Figure 3.9.: Pressure diffusion influenced by temperature and stress simultaneously. The injected water is 200 °C hot and viscosity along with density vary as in figure 3.5. Permeability and porosity are stress dependence is the same as in section 3.2.

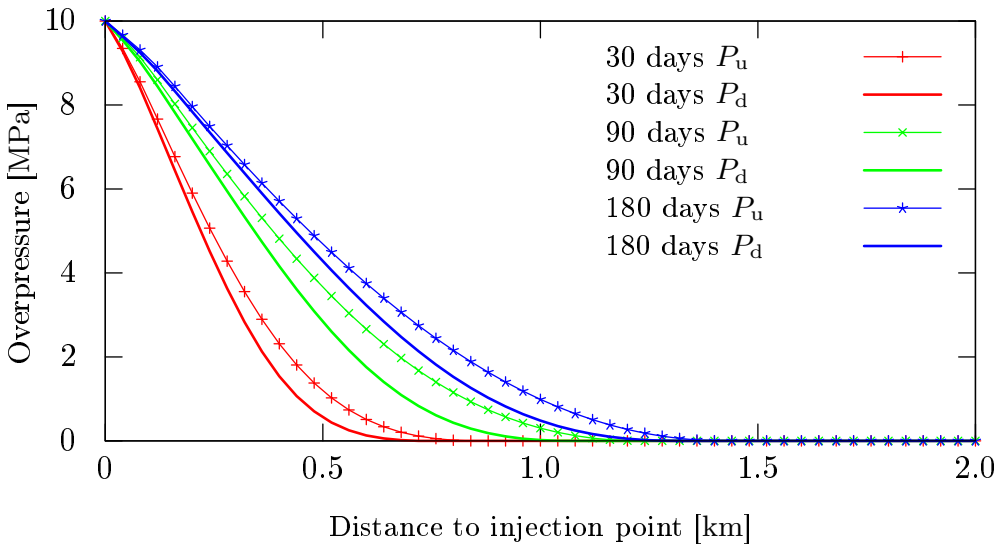

Figure 3.10.: To evaluate the symmetry of the diffusion, overpressure from figure 3.9 is plotted in respect to radial distance from the injection point. Upward pressure is always higher than downward if we consider a combination of temperature and stress effects. The maximum asymmetry of pressure occurs after about 90 days of injection.

3.6. Conclusion

To explain the vertically asymmetric, fluid-driven seismic events like aftershocks or earthquake swarms, we have studied three major physical processes that can be responsible for non-symmetric fluid flow in the Earth's crust. Using a one-dimensional model, we simulated fluid flow in a saturated medium due to overpressure and studied stress effects on rock permeability and porosity, as well as heat and salinity effects on density or viscosity.

The stress effect is implemented as an exponential relationship for porosity and permeability. This resulted in a significant difference between upward and downward fluid flow at short time scales, although effects become smaller at larger time scale due to the competing effect of pressure sensitive permeability and porosity.

We considered density and viscosity to be temperature-dependent and first studied the impact of a temperature gradient on each one separately. Downward diffusion is faster when constantly lowering viscosity with depth (e.g. due to temperature) is considered. Temperature diffuses much slower than fluid pressure. Therefore, buoyancy effects appear slower than viscosity effects but causes a similar asymmetry (almost 0.7 MPa after 180 days of injection).

Combinations of varying density and viscosity are also considered assuming two different scenarios where injected water had the same temperature as the pore fluid at the injection

point or a higher temperature. After 30 days of injection, the downward pressure is higher than the upward one due to viscosity profile. Thermal buoyancy effects appear later and overcomes the viscosity effect until 180 days. It is a long-term effect and at large time scales thermal effects can be the dominant process causing asymmetrical pressure diffusion.

We investigated density changes due to salinity contrasts between the system and high pressure fluid of higher or lower salt concentrations into the system. Density is considered as a linear function of salt concentration. The numerical results showed that salinity has a minor influence between top and bottom boundary overpressure. However, as shown in the temperature effects on density, buoyancy is a long-term process and can significantly contribute to non-symmetric diffusion with the intrusion of a less dense fluid into a saturated host system. Salinity can influence diffusion process more distinctly, if one considers fluid viscosity dependence on salt concentration, which we neglect in this work. In the last studied scenario, we coupled the effects of both temperature and stress, and found that the combined effects on permeability and temperature gradients lead to enhanced upward fluid flow.

It is shown that stress as a single source of non-symmetric diffusion plays an important role over short time scales even considering realistic permeability gradients. The temperature front spreads slower than pressure, and accordingly thermal effects appear over longer time period. This should be considered in models of fluid triggered seismicity more for accurate estimations of fluid pressure diffusion.

We also discussed scenarios in which the effect of faster upward can be reversed such as an unsaturated system where fluid permeability increases with saturation. Another instance is intrusion of highly saline fluid into the system. Of course, future models should also include geological structures like cap rocks or strong preferential hydraulic pathways that could dominate non-symmetric pressure diffusion.

4. Critical review of the local thermal equilibrium assumption in fracture networks and geothermal systems: dependence on permeability and porosity contrasts

Increasing demand of renewable energy sparked a renewed interest in extracting geothermal energy resources. An accurate description of the temperature field and related heat extraction potential remains a challenge and is critical for successful geothermal energy exploitation. Typically, two main approaches are used when modeling heat exchange and transport in geothermal reservoirs. The standard approach assumes immediate thermal equilibrium between solid and fluid phases (LTE), while another approach considers heat transport separately for the fluid and the solid and coupled through a heat exchange term (LTNE).

In this work, we investigate both the LTE and LTNE approaches and how they affect fluid and reservoir characteristic properties on temperature profiles. We compare LTE and LTNE heat transfer models in a simple, two dimensional model with a layer of different hydraulic parameters embedded in a host rock, and study in detail the role of heterogeneous distributions of permeability and porosity. Results of the effects of porosity and permeability contrast between the layer and the host rock on the predicted fluid temperature for the LTE and LTNE approaches reveal separate regimes in which the LTE assumption is the lower or upper bound for field scale heat transfer systems. Using these results, we compare LTE and LTNE models in a field scale geothermal model and show that LTE models significantly overestimate heat extraction potential over medium to long-term operational durations.

4.1. Introduction

Although exploiting geothermal power dates to ancient times, increasing demands of renewable energy make large scale production of geothermal power increasingly attractive because it is a base-load power source independent of weather variations. New technologies continue to advance geothermal techniques from heat extraction in bore hole heat exchangers to large scale power production in geothermal systems.

Methods used to investigate geothermal systems include in situ field measurements and increasing use of numerical models. Some excellent tools exist for characterising geothermal systems during stimulation and production phase that have been summarised in the literature [105, 106, 31, 107, 108, 109, 37]. Yet despite numerous studies, precise production estimates of these systems remain a challenge.

Accurately describing the dynamic temperature field in a geothermal system is critical for estimating heat production, the influence of thermal stresses and thermally-triggered seismicity [110]. The two commonly used continuum mechanical approaches describing heat transport in porous media include, 1) immediate thermal equilibrium between solid and fluid phase, termed local thermal equilibrium (LTE), and 2) separate but coupled heat transport in the fluid and solid phases addressed through a heat exchange term and termed local thermal non-equilibrium (LTNE). To date, numerical simulations of geothermal systems predominantly employ the LTE assumption.

Several detailed studies comparing fluid and solid phase temperature using the LTE and LTNE (e.g. [50, 51]) showed that the LTE assumption is appropriate since the observed temperature difference between rock and fluid temperature in LTNE are small. However, later studies showed significant differences between LTE and LTNE results. A small difference between rock and fluid temperatures in the LTNE model do not necessarily result in a similar temperature of LTE and LTNE models. For instance, Shaik et al. [30] simulate the heat production in a geothermal system with both LTE and LTNE models and conclude that the equivalent LTE model underestimates the produced fluid temperature. Although they did not inspect impacts of rock properties on the temperature difference, their work shows the importance of studying LTE and LTNE as different models. Lu-Wu and Zhi-He [53] find the radial stress around a spherical cavity in sandstone to be significantly larger assuming LTNE then LTE and Al-Sumaily et al. [52] show that LTE is not able to describe the fluid temperature in a porous cylinder at high temperature. Gelet et al. [111] explore the influence of LTE and LTNE heat transfer model on the mechanical response of the reservoir. They found, that only LTNE models are able to reproduce the mechanical reservoir response during thermal recovery. Yet, they assume solid impermeable blocks of rock and a saturated fracture network and neglect the fluid stored in the pore space, which may provide additional heat storage [25].

Constraining the temperature evolution of the system is also important from an economics viewpoint because overestimating the total geothermal energy production over the system lifetime can lead unfavorable economic consequences. Therefore, models that can estimate

the lower bounds of long-term heat flow provide a basis for assessing investment risk and financial feasibility.

To better understand the thermal equilibrium condition, we simulated coupled heat and fluid transport in a two-dimensional numerical model to explore the long-term behavior and the differences between the LTE and LTNE assumptions.

Following a summary of the equations governing fluid and heat transport with the LTE and LTNE assumptions in section 4.2, we benchmark the model with experimental data or analytical solutions in section 4.3. We then conduct a detailed sensitivity test with one layer embedded in a host rock of different hydraulic parameters, and investigate the effects of permeability and porosity contrast on LTE and LTNE results in section 4.4. Finally, we compare LTE and LTNE models at the field scale over long time scales in simulations of a fractured, heterogeneous geothermal reservoir with coupled fluid-rock properties in section 4.5.

4.2. Theoretical model

The governing equation corresponding to fluid flow is derived from generalized Darcy's Law, assuming a laminar flow in a fractured porous medium, along with the Boussinesq approximation. The heat transport equations are derived from the conservation of energy, where we neglect heat sources in the model domain.

4.2.1. Fluid mass balance and generalized Darcy's law

The conservation of mass for the fluid phase is given as:

$$\frac{\partial(\phi\rho)}{\partial t} + \nabla \cdot (\rho \boldsymbol{q}) = \rho Q_{\mathrm{s}} \ , \tag{4.1}$$

where ρ is mass density of the fluid [ML^{-3}], ϕ is rock porosity [-], Q_s is volumetric flow rate per unit volume of aquifer, representing the source or sink term [T^{-1}] and $\boldsymbol{q}$ is the Darcy velocity [LT^{-1}] defined as:

$$\boldsymbol{q} = -\frac{k}{\mu} \left(\nabla P - \rho \boldsymbol{g}\right) \ , \tag{4.2}$$

with k permeability of the porous medium [L^2], μ the dynamic viscosity of the fluid [$\mathrm{ML}^{-1}\mathrm{T}^{-1}$], P fluid pressure [$\mathrm{ML}^{-1}\mathrm{T}^{-2}$] and $\boldsymbol{g}$ the gravitational acceleration vector [LT^{-2}]. We define specific storativity of rock [$\mathrm{LT}^2\mathrm{M}^{-1}$] as:

$$S = \phi c_{\mathrm{f}} + (1 - \phi) c_{\mathrm{s}} \ , \tag{4.3}$$

with c_{f} and c_{s} as the fluid and rock compressibility [$\mathrm{LT}^2\mathrm{M}^{-1}$], respectively. Considering the Boussinesq approximation which neglects the density variations in the fluid mass balance

equation except in gravitational terms, the non-linear pressure diffusion equation is derived from equation (4.1):

$$S\frac{\partial P}{\partial t} + \nabla \cdot \left(-\frac{k}{\mu} \left(\nabla P - \rho \boldsymbol{g} \right) \right) = Q_\mathrm{s} \ . \tag{4.4}$$

4.2.2. Heat transport

In local thermal equilibrium there is no difference between fluid and rock temperature, so $T = T_\mathrm{f} = T_\mathrm{s}$ is representing the solid and fluid temperature [Θ]. Neglecting radioactivity and viscous dissipation effects, the linear heat equation is obtained [73]:

$$\rho c_\mathrm{p} \frac{\partial T}{\partial t} + \phi \left(\rho c_\mathrm{p} \right)_\mathrm{f} \boldsymbol{v} \nabla T - \lambda \nabla^2 T = 0 \ . \tag{4.5}$$

c_p and λ are thermal capacity [$\mathrm{L^2MT^{-2}\Theta^{-1}}$] and conductivity [$\mathrm{MLT^{-3}\Theta^{-1}}$] of the fluid-solid system respectively, weighted by porosity [74]:

$$\rho c_\mathrm{p} = \phi \left(\rho c_\mathrm{p} \right)_\mathrm{f} + (1 - \phi) \left(\rho c_\mathrm{p} \right)_\mathrm{s} \ , \tag{4.6}$$

$$\lambda = \phi \lambda_\mathrm{f} + (1 - \phi) \lambda_\mathrm{s} \ . \tag{4.7}$$

Subscripts s and f are used for solid and fluid phases. $\boldsymbol{v}$ is true fluid velocity and is related to Darcy velocity, through the Dupuit-Forchheimer relationship $\boldsymbol{q} = \phi \boldsymbol{v}$.
On the other hand, the LTNE model requires two coupled heat equations for the solid and fluid phases [74]:

$$\phi (\rho c_\mathrm{p})_\mathrm{f} \frac{\partial T_\mathrm{f}}{\partial t} + \phi (\rho c_\mathrm{p})_\mathrm{f} \boldsymbol{v} \cdot \nabla T_\mathrm{f} = \phi \lambda_\mathrm{f} \nabla^2 T_\mathrm{f} + h \left(T_\mathrm{s} - T_\mathrm{f} \right) \ , \tag{4.8}$$

$$(1 - \phi)(\rho c_\mathrm{p})_\mathrm{s} \frac{\partial T_\mathrm{s}}{\partial t} = (1 - \phi) \lambda_\mathrm{s} \nabla^2 T_\mathrm{s} + h \left(T_\mathrm{f} - T_\mathrm{s} \right) \ , \tag{4.9}$$

where h, the heat transfer coefficient [$\mathrm{ML^{-1}T^{-3}\Theta^{-1}}$], describes the heat exchange between the solid and fluid phases. In a porous bed of particles, h can be expressed as ([75, 74]):

$$h = a_\mathrm{fs} h^* \ , \tag{4.10}$$

a_fs is the specific fluid-solid surface area [$\mathrm{L^{-1}}$] and h^* is the interstitial heat transfer coefficient [$\mathrm{MT^{-3}\Theta^{-1}}$], which are given by [75]:

$$a_\mathrm{fs} = \frac{6(1 - \phi)}{d_\mathrm{p}} \ , \tag{4.11}$$

$$\frac{1}{h^*} = \frac{d_\mathrm{p}}{\mathrm{Nu_{fs}} \lambda_\mathrm{f}} + \frac{d_\mathrm{p}}{\beta \lambda_\mathrm{s}} \ , \tag{4.12}$$

where $\mathrm{Nu_{fs}}$ is the fluid-to-solid Nusselt number [-]. Assuming that the porous medium consists of spherical particles, d_p is the particle diameter [L] and $\beta = 10$ [74]. Recent studies (e.g. [81, 82, 112]) show that h^* depends on fluid velocity and temperature as well as on

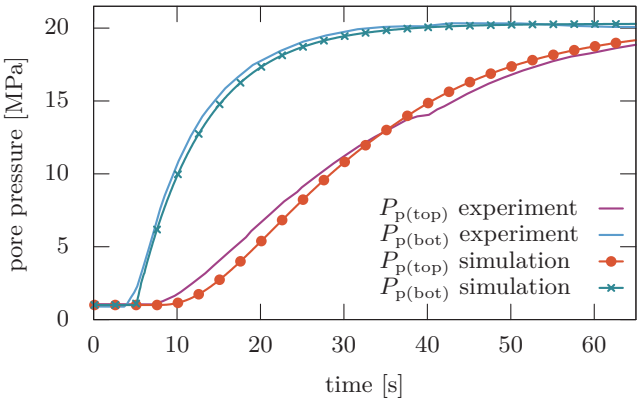

Figure 4.1.: Pore pressure on top and bottom of a sandstone sample (no. Fb28) during hydraulic fracturing [80]. The kink in the pore pressure experimental curve at the top is due to sample failure, which is not reproducible in our model.

thermal properties of fluid and solid.

4.3. Numerical model and benchmarks

We model the 2D porous fractured media using a single medium. We solve equations (4.4), (4.5), (4.8) and (4.9) using explicit finite difference approximations. For the advection part of the heat transfer equations (4.5), (4.8) and (4.9), we employ a semi-Lagrangian scheme with cubic spline interpolation.

Each part is validated separately, using laboratory experiments and analytical solutions. First, forced fluid flow inside a saturated rock is verified by reproducing the experimental results of Stanchits et al. ([79, 80]). In those experiments, water injected from the bottom with 20 MPa into a saturated sandstone in which increased pore pressure results in shear failure of the sample. To reproduce the experimental results, we introduce variable porosity and permeability following Rutqvist and Tsang [16]. The numerical results of pore pressure at the top and bottom of this sample compare well with the measured values (figure 4.1), with a mean derivation between simulation and experimental data below 10%. Further details on the numerical reproduction of the experiment can be found elsewhere [19].

Heat transfer is modeled under both the LTE and LTNE assumptions. To validate the LTNE model, we numerically reproduce the experiments of Zhao and Tso [81] following the parameterization derived in [82]. In these experiments water flows through a single fracture in the middle of a low permeability rock, while the temperature at the outer surface of the rock is kept constant.

Fracture aperture and rock temperature are known, as is the inflow and outflow water velocity and temperature. Parameters for heat transfer are taken from [82], although parameters are unavailable for two experiments. The numerical results of water outflow temperature (reported in table A.1), show good agreement to the experiments with simulated temperatures in a 1 °C window around measured values.

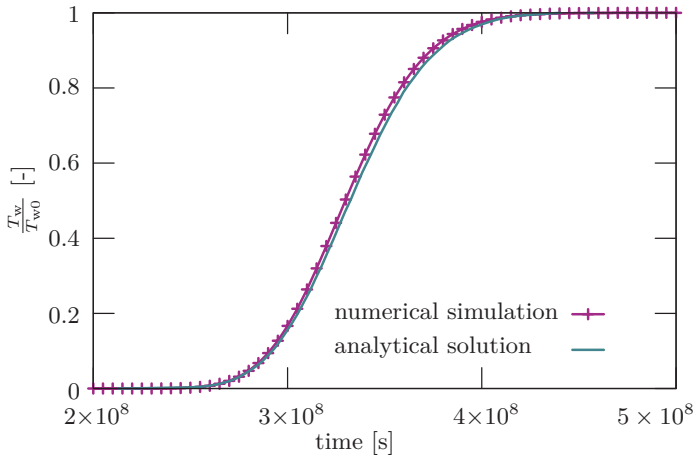

Figure 4.2.: Benchmark for heat flow under LTE assumption. Temperature breakthrough curve at the end on a fracture. The simulation results are in good agreement with the analytical solution of [83].

We benchmark the LTE model, like others [31], using the analytical solution for one-dimensional advective-diffusive heat transport in a saturated fracture [83]. Flow velocity is assumed constant along the fracture and the fracture is defined as a porous medium with $\phi = 1$. Initial temperature inside the fracture is $T_0 = 0\,°\mathrm{C}$ and input water temperature $T_{\mathrm{in}} = 1\,°\mathrm{C}$. Figure 4.2 compares the analytical solution and simulation results of this problem, showing an error of approximately 0.65% at time $t = 3.7 \times 10^8\,\mathrm{s}$.

The same module is tested for heat transport in a homogeneous porous medium with variable density [31]. Water with initial temperature $T_{\mathrm{in}} = 400\,\mathrm{K}$ flows into a porous matrix with $\phi = 0.01$, $k = 10 \times 10^{-11}\,\mathrm{m}^2$ and $T_0 = 300\,\mathrm{K}$, under a constant pressure gradient.

We performed three different 1D numerical simulations, one with $\rho = 1000\,\mathrm{kg\,m^{-3}}$ related to T_0, a second with $\rho = 900\,\mathrm{kg\,m^{-3}}$, corresponding to T_{in} and third with variable density. For temperature- and pressure-dependent fluid density, we use the results of Sun et al. [88]. Temperature evolution curves in figure 4.3 show that the results with variable density lie between the upper and lower density-bounds, as expected, demonstrating an accurate numerical model.

In spite of the very good agreement of the LTE model and analytical solutions,it does not reproduce the experimental results of Zhao and Tso [81], which can be described well using the LTNE. Although rock and fluid properties are well defined in [113, 81, 82], the resulting temperatures using the LTE are always too high compared with measured values, in fact they are close to initial rock temperature. This shows that although the LTE module is numerically verifiable, this assumption may fail in reproducing some experimental data.

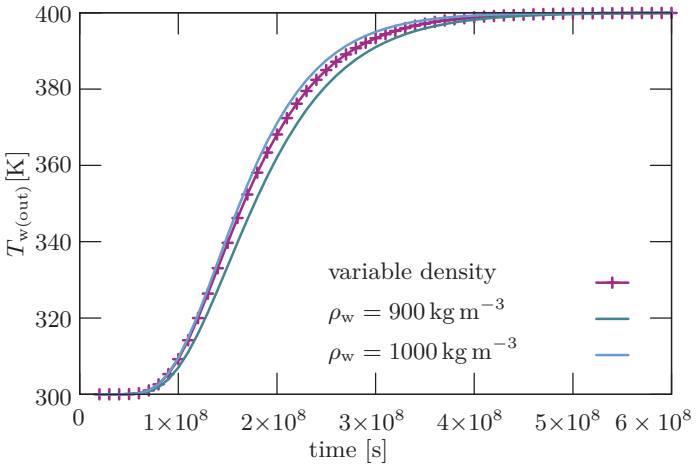

Figure 4.3.: Verification of the LTE assumption. Evolution of the output temperature of water flowing in a homogeneous porous medium is shown here. The variable density curve behaves as expected between minimum and maximum density values (following [31]).

4.4. Divergence of model temperatures in fractured porous media

As shown in section 4.3, the steady state results of LTE and LTNE in modeling heat transport in fractured media do not converge necessarily in any scenario. Especially the presence of heat sources in both phases can cause persistence of non-equal phase temperatures even for infinite time. In such cases the LTE model can not predict correct values. We assume a simple set-up to test if the divergence in phase temperatures or between LTE and LTNE approaches also persists over reasonable time frames also in other scenarios. The schematic of the test set-up (figure 4.4) adopts a set-up similar to Zhao and Tso [81]. We simulate fluid flow and heat transfer in a 3 m×1 m rock sample with a single layer of different hydraulic parameters in the middle of the host rock using a grid resolution of 10 cm×10 cm. We assume a horizontal rock plate ignore gravity forces.

The initial temperature of the saturated host rock is $T_0 = 180\,°\mathrm{C}$. Fresh water with $T_{in} = 80\,°\mathrm{C}$ is injected from the left side with constant input pressure $P_{in} = 110\,\mathrm{kPa}$, while the pressure at the right side is set to 100 kPa. Thermal conductivity of rock is $2.8\,\mathrm{W\,m^{-1}\,°C^{-1}}$ and of water $0.609\,\mathrm{W\,m^{-1}\,°C^{-1}}$. Rock density is $\rho_r = 2820\,\mathrm{kg\,m^{-3}}$ and heat capacity $c_{p,r} = 790\,\mathrm{J\,kg^{-1}\,°C^{-1}}$. Water density $\rho_f = 998.2\,\mathrm{kg\,m^{-3}}$, heat capacity $c_{p,f} = 4200\,\mathrm{J\,kg^{-1}\,°C^{-1}}$ and viscosity $\mu = 1\times10^{-3}\,\mathrm{Pa\,s}$ as well as the rock properties, are

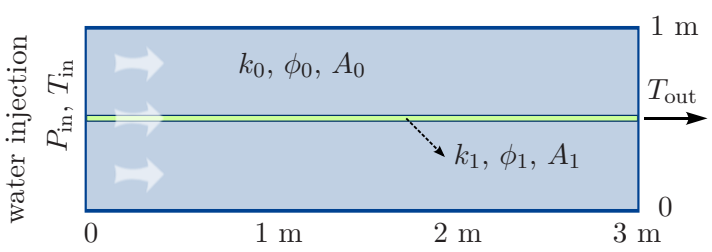

Figure 4.4.: The set-up used for the sensitivity test of LTE and LTNE approaches. Neumann boundary condition is assumed for fluid flow and heat transport on top and bottom.

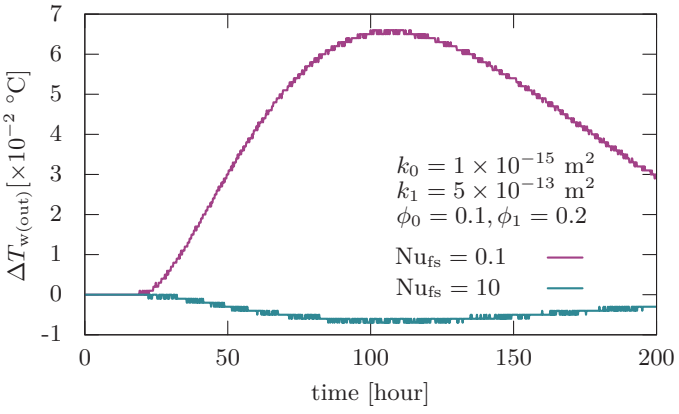

Figure 4.5.: To examine the code sensitivity to Nusselt number, three different values are tested in the range mentioned by [74]. The plot shows the output temperature deviation from the $Nu_{fs} = 1$ case.

constant during the numerical simulations. Neumann boundary conditions are applied for pressure and temperature at top and bottom boundaries of the model.

4.4.1. Consistent parameterization

Comparing LTE and LTNE models without a well-defined heat exchange term is not reliable. As pointed out [75], the heat transfer coefficient h^* depends on fluid-to-solid Nusselt number Nu_{fs} (equations (4.11) and (4.12)), and particle diameter d_p.

According to [74], Nu_{fs} is estimated in two different regimes depending on the Reynolds number, Re, controlled by d_p. In laminar flow, where Re is low, Nu_{fs} varies between 0.1 and 12.4 [74]. We examine three different values in this range in which advective-dominant scenarios as well as diffusion-dominant scenarios are investigated.

For simplicity we keep the heat transfer area a_{fs} constant during this test over the whole domain. We assume that the porous medium consists of spherical particles with radius $r_p = 1\,\text{mm}$. However, porosity and permeability are not constant. We consider a sandstone with typical porosity and permeability of $k_0 = 10 \times 10^{-15}\,\text{m}^2$ and $\phi_0 = 0.1$ [114] for host rock. Permeability and porosity of the embedded layer are assumed to be $k_1 = 500 \times k_0$ and $\phi_1 = 0.2$.

The numerical simulation is tested under LTNE assumption and the deviation of outflow temperature from $Nu_{fs} = 1$ is shown in figure 4.5. Raising Nu_{fs} from 0.1 to 10, increases h^* almost two orders of magnitude (from almost 30 to $2501\,\text{W}\,\text{m}^{-2}\,°\text{C}^{-1}$), yet the absolute temperature deviation does not exceed 0.07 °C. This occurs because for sandstone a_{fs} mainly controls the heat transfer coefficient. Therefore, in subsequent simulations we assume $Nu_{fs} = 1$ in the simple one-layer experiments. In geothermal systems however, we distinguish fracture zone from intact matrix and set $Nu_{fs} = 10$ for the former and $Nu_{fs} = 0.1$ for the latter to emphasize the advective behavior in fractures and primarily diffusive behavior in a porous matrix.

The other parameter required to determine h in a LTNE model is the fluid to solid heat transfer area a_{fs}. Due to lack of experimental data about the specific surface area in

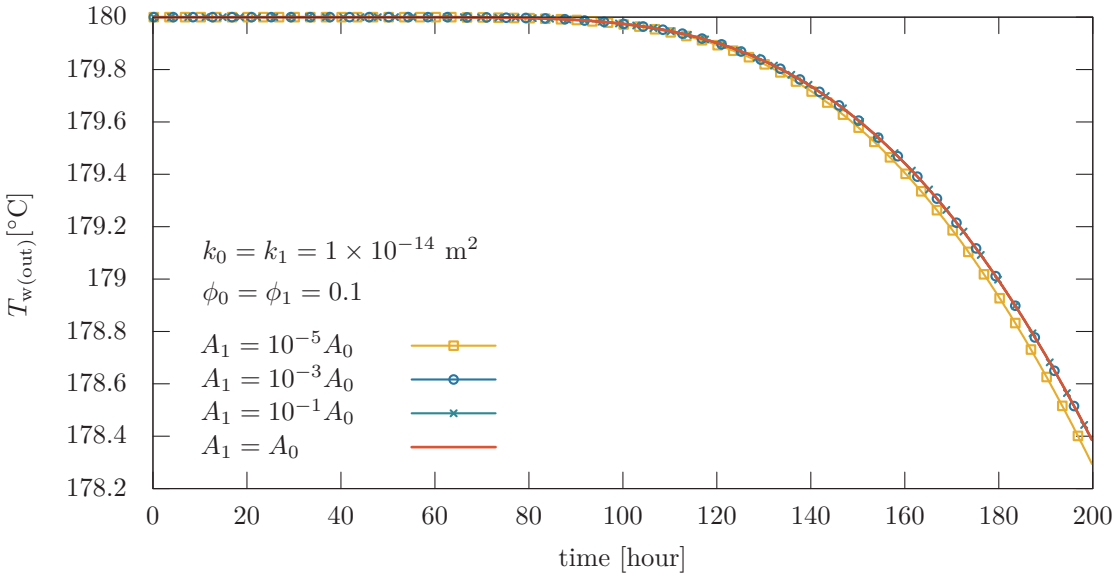

Figure 4.6.: Heat exchange between fluid and rock is proportional to the heat transfer area. Here we assume a sample with homogeneous permeability and porosity and compare the outflow temperature in various scenarios. The case with the smallest A_1, has cooler outflow since heat exchange with rock is smaller.

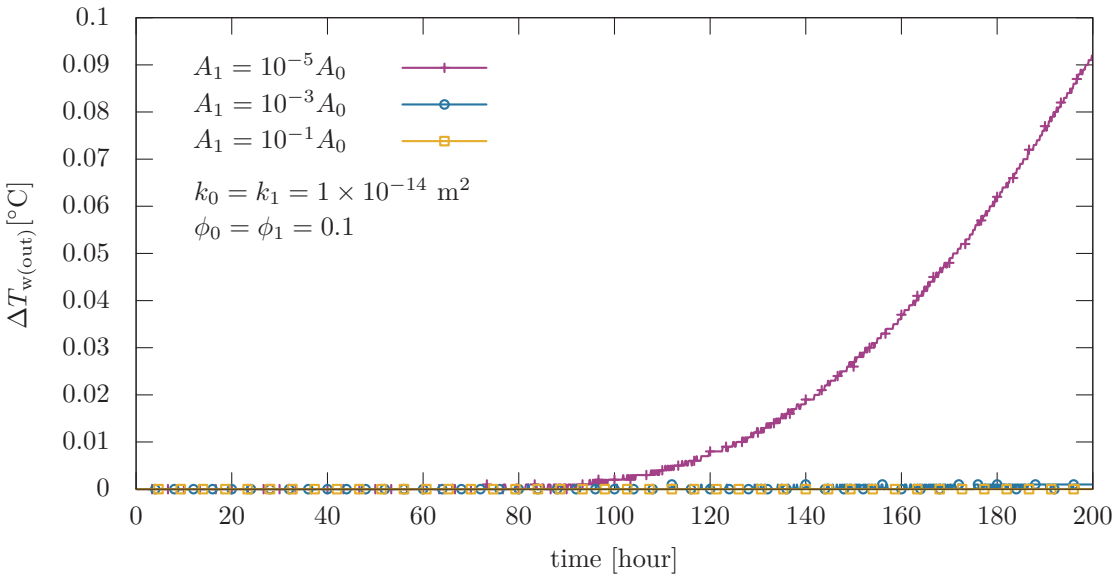

Figure 4.7.: Deviation of outflow temperature from the case $A_1 = A_0$. Assuming $r_p = 1 \times 10^{-3}$ m, a_{fs} is so large that the simulation is not sensitive to A_1.The outflow temperature change in the case $A_1 = 10^{-5} A_0$, after 200 his still less than 0.1 °C.

fractured media, again, we test sensitivity of our set-up to this parameter, starting from a similar value used in the previous simulation. Additionally, we perform a series of simulations with different A_1 to A_0 ratios, separating heat transfer areas in the layer from the host rock, while keeping homogeneous porosity and permeability. The temperature curves in figure 4.6 show little variation when assuming $A_1 \geq 10^{-3} A_0$. This is shown more prominently in figure 4.7, where minimal outflow temperature deviations from the case in which $A_1 = A_0$ are demonstrated. The reason is again the large values of A_0 in a highly porous medium.

Amiri and Vafai ([50, 115]) examine the LTE condition by comparing the dimensionless fluid and solid phase temperatures under LTNE assumption at any time . Based on our numerical simulations we observed local similarity of T_f and T_s in LTNE, but fluid temperatures under LTNE and LTE approaches, $T_\mathrm{f}^\mathrm{LTNE}$ and T^LTE respectively, differ from each other. A new dimensionless parameter $\%\Delta T_\mathrm{w}$ is defined, analogous to the parameter %LTE of [50], to evaluate the differences between LTE and LTNE models in time or space:

$$\%\Delta T_\mathrm{w} = \frac{T^\mathrm{LTE} - T_\mathrm{f}^\mathrm{LTNE}}{T_0 - T_\mathrm{in}} \times 100 \ . \tag{4.13}$$

4.4.2. Influence of porosity and permeability contrast

In this section we investigate the influence of permeability and porosity of the host rock and layer on water outflow temperature $T_\mathrm{w(out)}$ under LTE and LTNE assumptions. We start with porosity effects by setting typical values for fractured sandstones e.g. $k_0 = 1 \times 10^{-15}\,\mathrm{m}^2$, $k_1 = 5 \times 10^{-13}\,\mathrm{m}^2$, $\phi_0 = 0.1$ [114]. We vary layer porosity ϕ_1 from 0.01 to 0.20. Figure 4.8 shows the temperature breakthrough curves of three cases $\phi_1 = 0.01$, $\phi_1 = 0.20$ and $\phi_1 = \phi_0 = 0.1$ using both heat transfer models.

Assuming a constant porosity for the entire system results in the same output temperatures for LTE and LTNE. In the equivalent model $T_\mathrm{w(out)}$ does not depend notably on porosity. On the other hand, the non-equivalent one is more sensitive to this parameter.

Interestingly, $T_\mathrm{w(out)}^\mathrm{LTNE}$ is higher than in the LTE case, if $\phi_1 < \phi_0$ and lower if $\phi_1 > \phi_0$. Figure 4.9 shows the $\%\Delta T_\mathrm{w(out)}$ in time, for different porosities. As the contrast between ϕ_0 and ϕ_1 increases, the difference between equivalent and non-equivalent model increases up to about 5 % in 200 h. Numerical simulation results of a geothermal system by Shaik et al. [30] show underestimation of fluid temperature by the LTE model. [H]

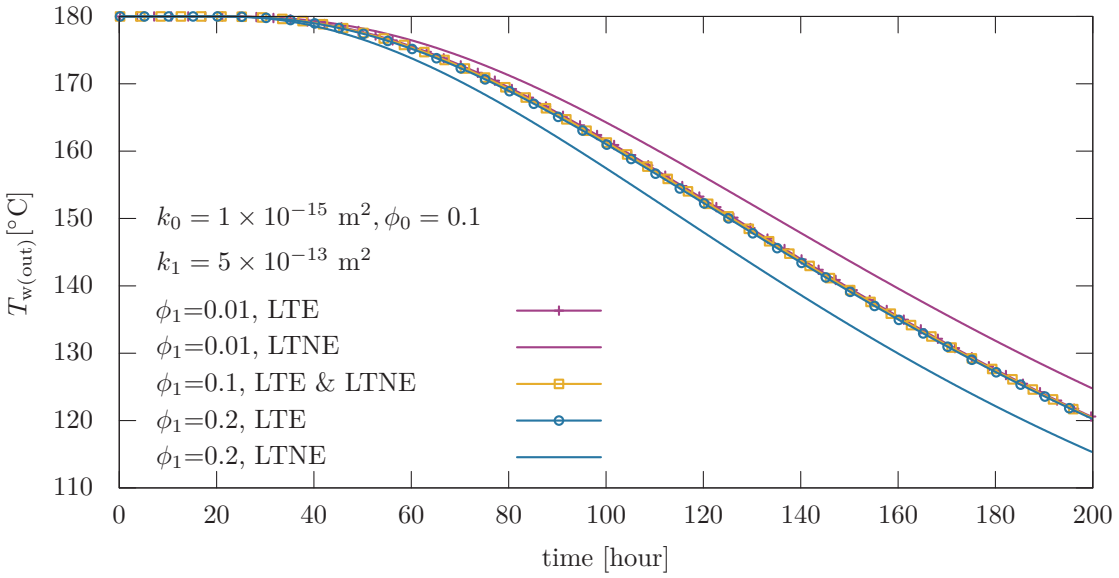

Figure 4.8.: Water outflow temperature of simulations with different porosity of the embedded layer. LTNE model is sensitive to the porosity contrast, while LTE model does not show significant changes.

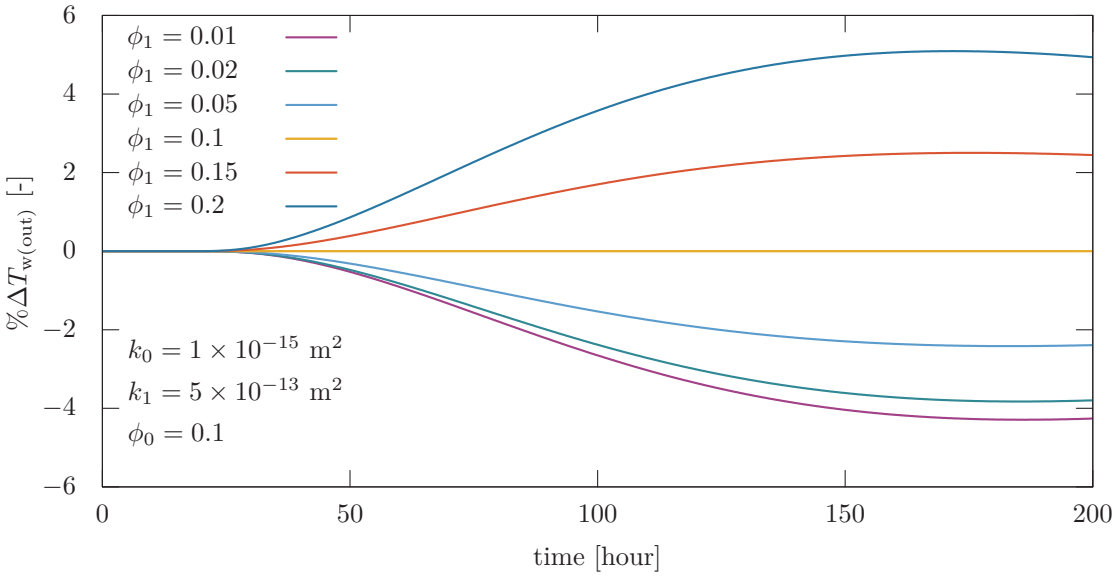

Figure 4.9.: In the case of similar porosity in the host rock and layer, both LTE and LTNE approaches show the same results and $\%\Delta T_{w(out)}$ vanishes. The ratio of ϕ_1 to ϕ_0 determines whether T_f^{LTE} is smaller or T_f^{LTNE}.

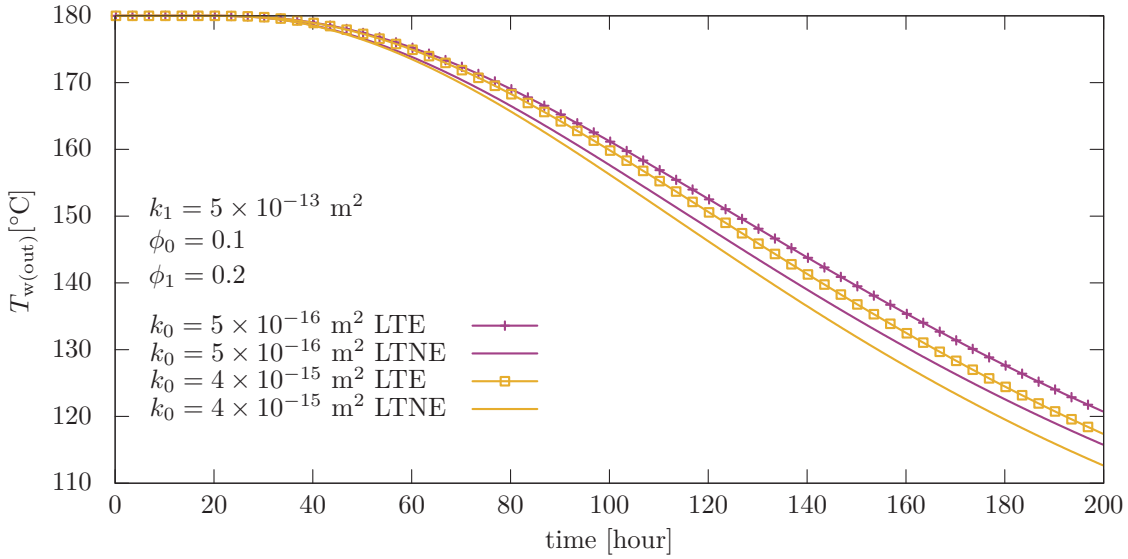

Figure 4.10.: Water outflow temperature of two different host rock permeabilities while the layer permeability is constant. The host rock with higher permeability cools down faster and therefore provides the layer flow with less heat.

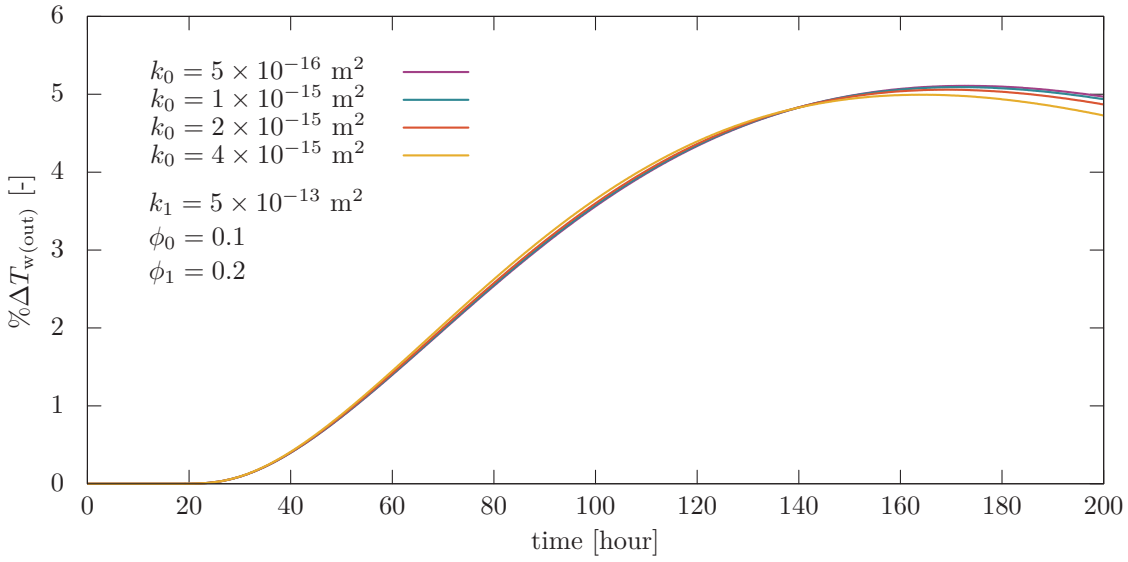

Figure 4.11.: The LTE and LTNE models both react to k_0 changes in the same way. The difference between two models increases to a maximum of about 5 %.

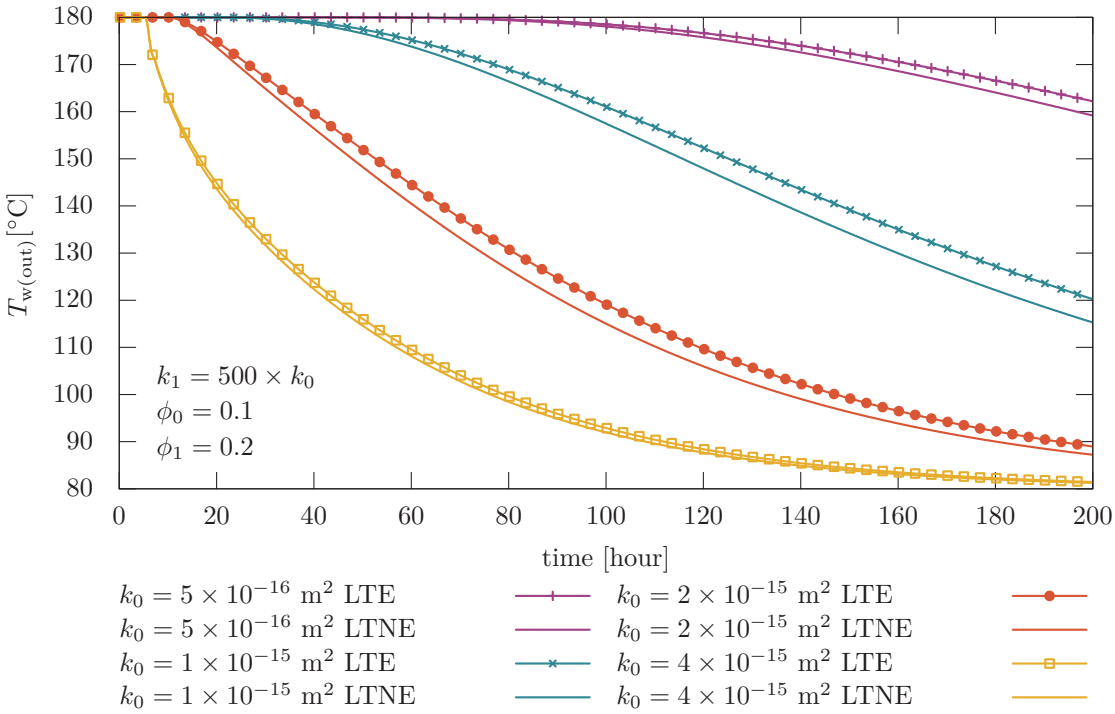

Figure 4.12.: Breakthrough curves in different permeability ranges. Layer and host rock permeabilities are varying while the ratio $\frac{k_1}{k_0}$ is constant. Water temperature predictions under the LTE are higher than the LTNE since ϕ_1 is assumed to be larger than ϕ_0.

We can therefore presume they set porosity in the less fractured numerical cells higher than in cells than they define as highly fractured. Nevertheless, various field measurements for instance by Xu et al. [116] or Vernoux et al. [117] show a higher porosity in the fracture zones, so we use $\phi_1 = 0.2$ and $\phi_0 = 0.1$ in the simple simulations with one embedded layer.

Next, we investigate the effect of host rock permeability by setting k_1 a constant and changing k_0. Figure 4.10 shows $T_{w(out)}$ evolution for two different matrix permeabilities. The water temperature falls faster when host rock permeability is higher. This is plausible because the matrix acts like a heat reservoir for the system and with high permeability, the rock cools down faster. This can be seen for both equivalent and non-equivalent models.

The differences between these approaches remain almost constant up to about 5 % in various k_0 values, as shown in figure 4.11. We observe that the difference between $\%\Delta T_{w(out)}$ for $k_0 = 5 \times 10^{-16}\,\mathrm{m}^2$ and $k_0 = 4 \times 10^{-15}\,\mathrm{m}^2$ is about 0.3 % after 200 h. The ratio of k_1 to k_0 has therefore only minor effect on differences between the LTE and LTNE assumptions.

To investigate the effect of a permeability contrast between the layers with a constant ratio between them, we vary k_0 from $5 \times 10^{-16}\,\mathrm{m}^2$ to $4 \times 10^{-15}\,\mathrm{m}^2$ while k_1 is assumed to be 500 times larger than k_0. Figure 4.12 shows that water temperature reduces faster in high permeability rocks as expected.

Corresponding $\%\Delta T_{\mathrm{w(out)}}$ in figure 4.13 shows a typical evolution of $\%\Delta T_{\mathrm{w(out)}}$, which starts from zero and then reaches its absolute maximum value where the equivalent and non-equivalent models diverge the most and then decreases as the host rock cools down to input water temperature. We observe that LTE and LTNE models coincide better in the high permeability cases.

For $k_0 = 5 \times 10^{-16}\,\mathrm{m}^2$, the maximum divergence is not achieved during the simulation time. The maximum value of $\%\Delta T_{\mathrm{w(out)}}$ is over 5 % for $k_0 = 1 \times 10^{-15}\,\mathrm{m}^2$. This value falls to 1.4 % for $k_0 = 4 \times 10^{-15}\,\mathrm{m}^2$. Comparing these results with figure 4.11, we conclude that the difference between the two models increases with decreasing permeability causing lower flow velocity. This means in the case of high permeable porous medium, the predictions of LTE and LTNE models converge.

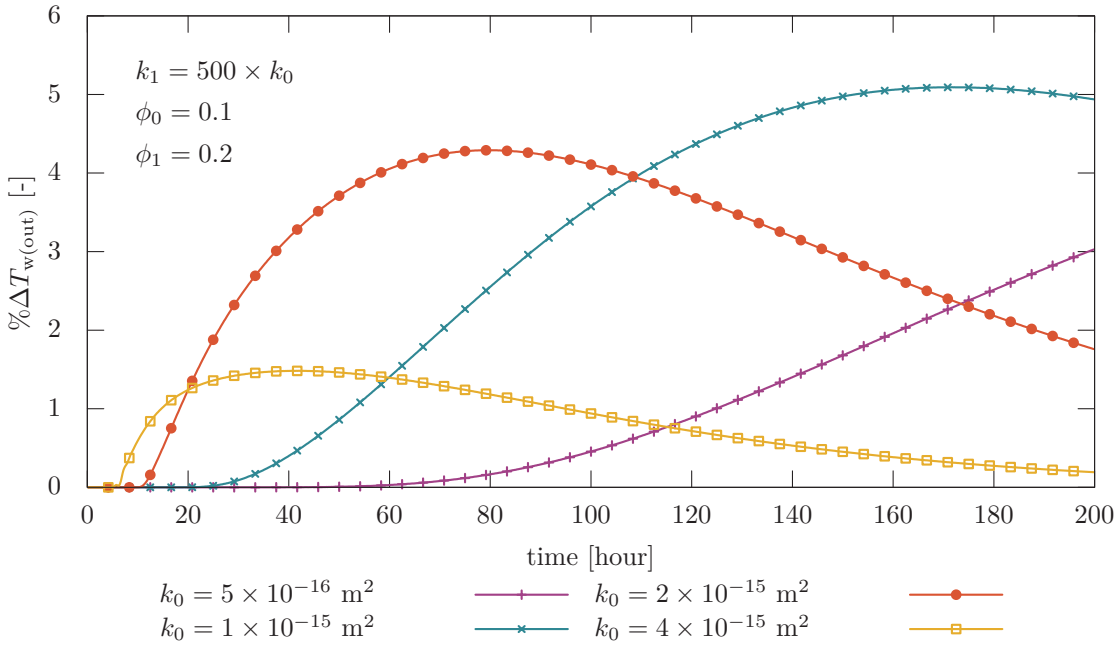

Figure 4.13.: Difference between water outflow temperature under the LTE and LTNE assumptions. Three stages of a typical $\%\Delta T_{\mathrm{w}}$ curve can be seen here: 1. zero value for pumping out reservoir water 2. increasing to a maximum value which starts when the injected water is through the domain 3. declining to zero as the reservoir cools down. Layers with less permeabilities lead to a higher divergence between the LTE and LTNE models. Maximum value of $\%\Delta T_{\mathrm{w(out)}}$ related to the least permeable rock is not reached in the simulation time.

4.5. Application to geothermal systems

In the previous section we investigated under which conditions divergence of the equivalent and non-equivalent approaches becomes significant. We found differences between the two approaches are amplified with low permeability and porosity contrasts between the different layers. Here we simulate a hypothetical geothermal system under both LTE and LTNE assumptions to determine if similar conclusions can be drawn and to quantify the divergence between both models. An arbitrary fracture network is generated over a domain of 1 km×1 km as shown in figure 4.14 and then mapped to the finite difference grid.

Assuming a five spot well pattern as in [118, 119], the top right quarter of this network is mapped on a 30×30 grid and used for the numerical simulations. This domain is located at the depth of $z_0 = 2\,\text{km}$, horizontally, so that the gravitational effect on fluid flow is negligible.

Following Rutqvist and Tsang [16], we consider rock porosity as a function of the mean effective stress, σ'_{M}:

$$\phi = \phi_{\text{r}} + (\phi_0 - \phi_{\text{r}})\, exp\left(a \cdot \sigma'_{\text{M}}\right) \tag{4.14}$$

where ϕ_{r} is residual porosity, ϕ_0 is porosity at zero stress and a an experimental control parameter. This leads to higher porosity values in the fracture zone and therefore as it is shown in section 4.4.2, the non-equivalent model generates a lower limit for the outflow temperature.

We consider a normal distribution of ϕ_0 with a standard deviation of 5% and a mean value of 0.15 while zero stress porosity is set to 35% in the fracrure zone. The permeability depends on porosity, following [16]:

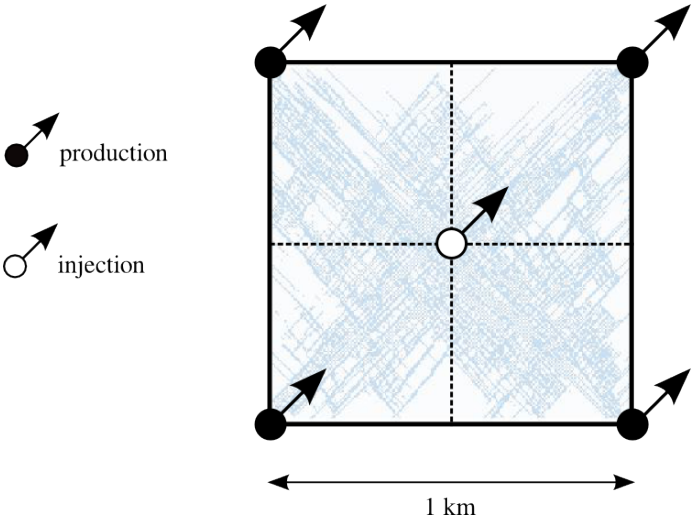

Figure 4.14.: The arbitrary fracture network in the five-spot well pattern following [118]. We introduce heterogeneity and use only the upper right quarter for the numerical simulation of a geothermal system.

$$k = k_0 \; exp\left[b\left(\frac{\phi}{\phi_0} - 1\right)\right] \tag{4.15}$$

k_0 is the zero stress permeability and b is an experimental permeability control parameter. We consider k_0 to be strongly heterogeneous and set it 50 times larger in the fracture zone rather than elsewhere in the simulation field. Besides, a normal distribution of k_0 is assumed with a mean value of $5 \times 10^{-14}\,\mathrm{m}^2$ and a standard derivation of 10 % which results in the permeability distribution shown in figure 4.15.

Fluid density and heat capacity depend on temperature and pressure following Sun et al. [88]. Fluid viscosity is temperature dependent as in Huyakorn and Pinder [99]. Other rock and fluid parameters used in the numerical simulations are presented in table 4.1. Figure 4.16 shows the flowchart of the numerical algorithm.

Water at 80 °C with a constant injection rate is pumped from bottom left corner into the reservoir with initial temperature of $T_0 = 200\,°\mathrm{C}$ and initial pressure of $P_0 = \rho_\mathrm{w} g z_0$. The production well is in the top right corner and production rate is assumed to be 25 % of the injection rate, if the overpressure is positive. The flow rate into and from the reservoir are computed depending on the matrix permeability, as Miller [20]:

$$Q_\mathrm{s} = A\boldsymbol{q} = 2\pi RH\boldsymbol{q} \tag{4.16}$$

A is the area of the open-hole section and $\boldsymbol{q}$, the fluid velocity across it. The radius R is assumed to be 1 m and the open-hole length $H = 10\,\mathrm{m}$. A Neumann boundary condition is assumed for non-linear pressure and temperature processes at the boundaries, except at the injection and production corners where we apply Dirichlet boundary condition for temperature.

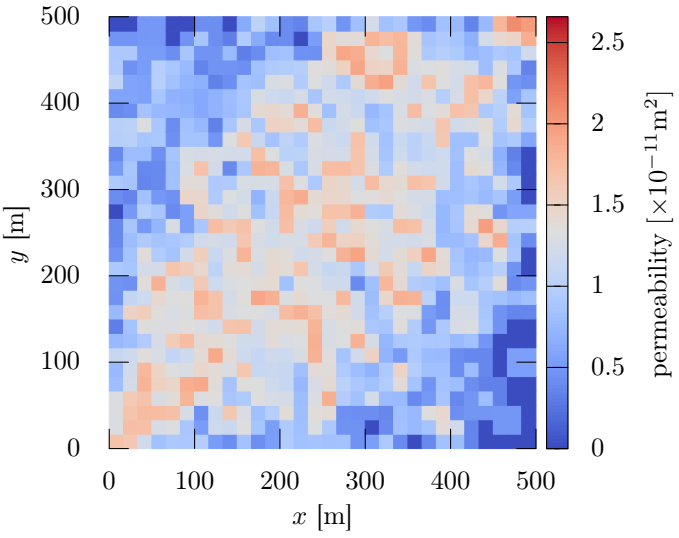

Figure 4.15.: The permeability field used within the geothermal system simulation obtained by mapping the fracture network in figure 4.14 on a 30×30 numerical grid and considering a normal distribution arround $5 \times 10^{-14}\,\mathrm{m}^2$ with a standard derivation of 10 %.

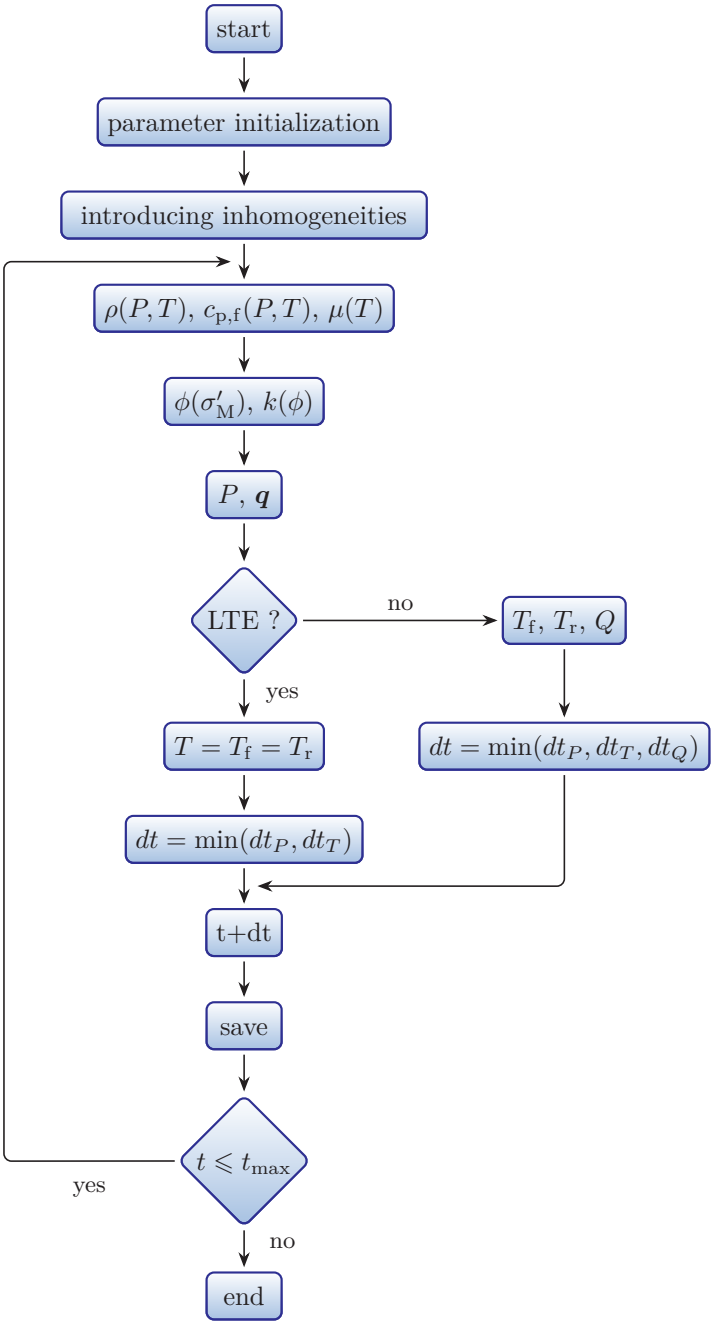

Figure 4.16.: Numerical steps in simulation a geothermal system. In each time-step, after computing the fluid properties, porosity and permeability, overpressure and darcy velocity are calculated. Darcy velocity field is used to calculate the advective part of the heat transport.

rock properties		
density of rock	ρ_r	$2820\,\mathrm{kg\,m^{-3}}$
intrinsic permeability of reservoir	k_0	$2 \times 10^{-15}\,\mathrm{m^2}$
exponent for equation (4.15)	b	2
zero stress porosity	ϕ_0	0.1
residual porosity	ϕ_r	0.001
exponent for equation (4.14)	a	$1 \times 10^{-8}\,\mathrm{Pa^{-1}}$
pore compressibility	c_s	$1 \times 10^{-8}\,\mathrm{Pa^{-1}}$
rock grain diameter	d_p	$2 \times 10^{-3}\,\mathrm{m}$
heat capacity of rock	c_{pr}	$1170.0\,\mathrm{J\,kg^{-1}\,°C^{-1}}$
thermal conductivity of rock	λ_s	$2.80\,\mathrm{W\,m^{-1}\,°C^{-1}}$
fluid properties		
fluid compressibility	c_f	$1 \times 10^{-10}\,\mathrm{Pa^{-1}}$
thermal conductivity of fluid	λ_f	$0.609\,\mathrm{W\,m^{-1}\,°C^{-1}}$
fluid-to-solid Nusselt number	$\mathrm{Nu_{fs}}$	10

Table 4.1.: Parameters used in the simulation of a geothermal system.

4.5.1. Geothermal Systems: Results

Figure 4.17 shows simulation results of produced water temperature at three different injection rates, $50\,\mathrm{L\,s^{-1}}$, $100\,\mathrm{L\,s^{-1}}$ and $150\,\mathrm{L\,s^{-1}}$, for both LTE and LTNE models. Outflow temperature starts to decrease after about 7 yr of production and the drop rate depends on the injection and production rates. It can also be seen that the LTE approach results in higher fluid temperature.

Differences in water outflow temperature between LTE and LTNE models after 40 years of production are 4.52 °C, 5.11 °C and 5.27 °C for $50\,\mathrm{L\,s^{-1}}$, $100\,\mathrm{L\,s^{-1}}$ and $150\,\mathrm{L\,s^{-1}}$ injection rates, respectively. Figure 4.18 shows $\%\Delta T_{w(out)}$ for different injection rates in time. After 40 years the temperature difference is smaller than 5 %, supporting the argument that LTE is a reasonable assumption in this time range [50]. However, from a commercial standpoint this difference may matter. Richards et al. [120] points out that commercial Hot Dry Rock systems need to produce at $50\,\mathrm{L\,s^{-1}}$ rate without major decrease in 20 yr. Hence the 1 % temperature difference reached after this time (figure 4.18), may be important at in commercial scales. Moreover, if we assume that figure 4.13 represents typical behavior of $\%\Delta T_w$ curves, the maximum value of the curves are not covered in the simulated time frame of 40 years. For longer times the difference in water outflow temperature between both models will continue to increase.

Studies often present average water temperature in the reservoir in addition to the outflow water temperature, and figure 4.19 shows the temporal average water temperature in

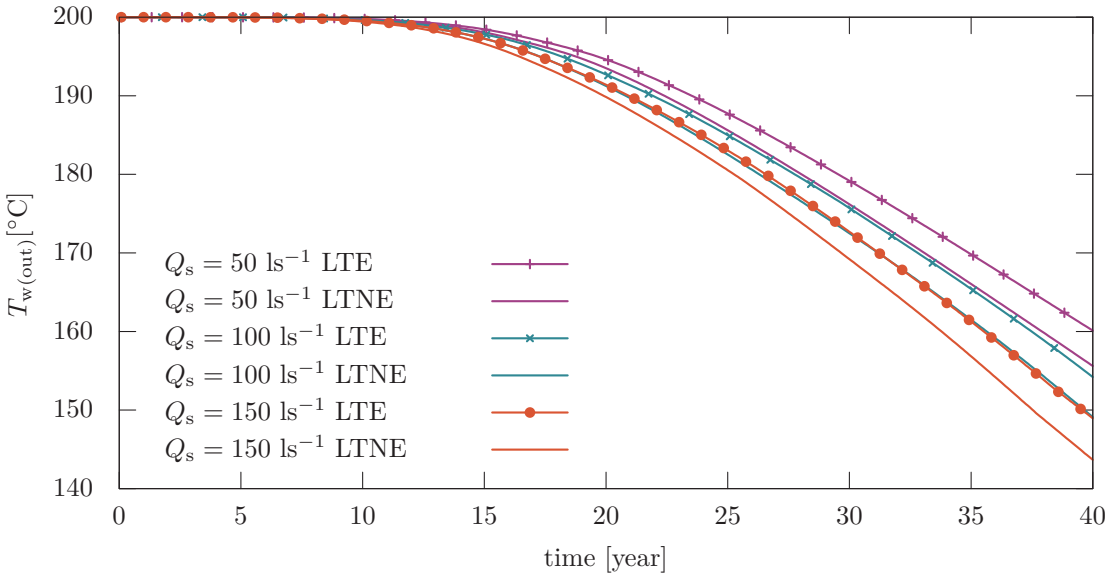

Figure 4.17.: Produced water temperature for different injection rates under the LTE and LTNE assumptions. Higher injection and production rates cause faster fluid temperature drop.

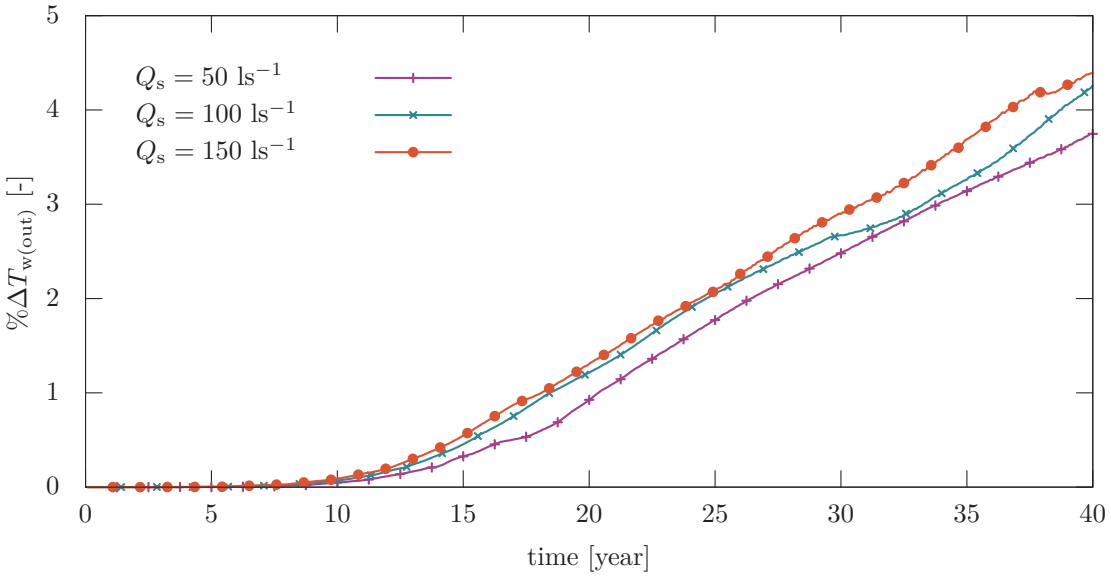

Figure 4.18.: Difference between produced water temperature under the LTE and LTNE assumptions. $\%\Delta T_{w(out)}$ is greater in lower fluid rates, as expected from single fracture zone experiments.

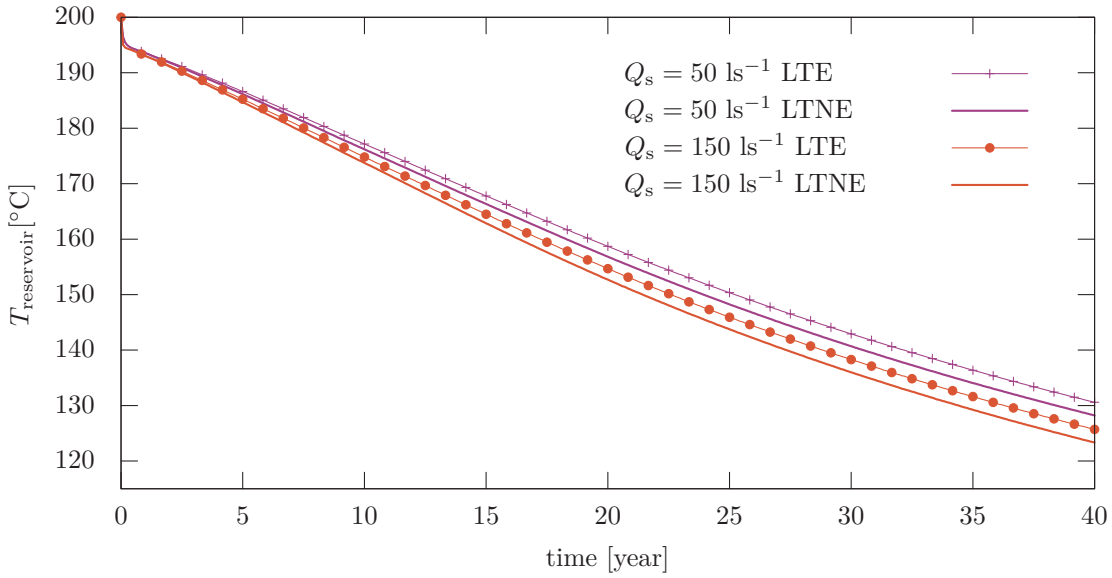

Figure 4.19.: Average water temperature in the reservoir for two different injection rates.

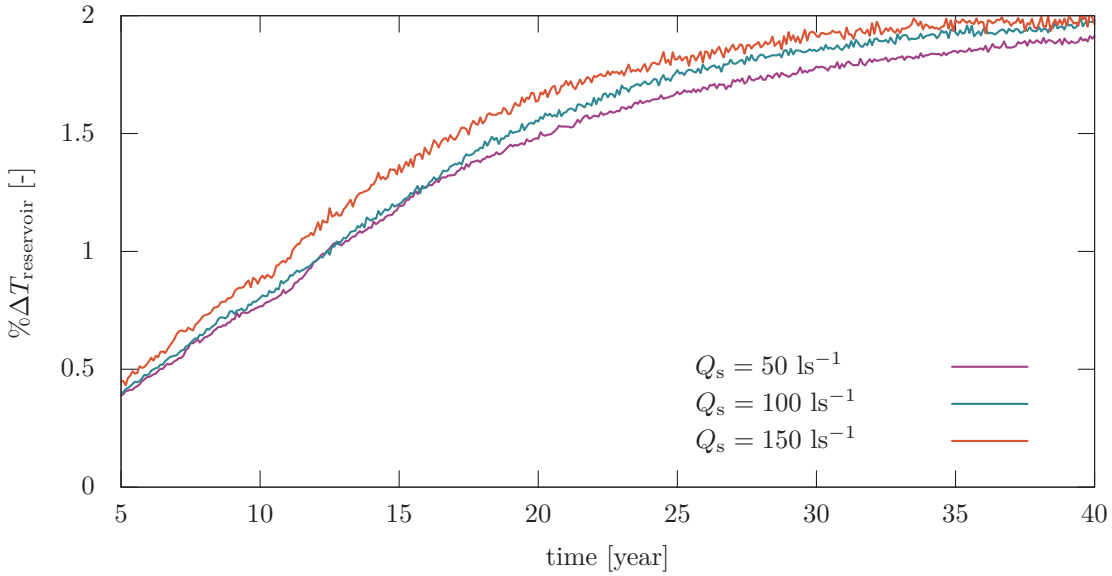

Figure 4.20.: Difference between average reservoir fluid temperature under the LTE and LTNE assumptions.

the reservoir at two different flow rates $50\,\mathrm{L\,s^{-1}}$ and $150\,\mathrm{L\,s^{-1}}$. The rapid decrease at the beginning occurs because of the Dirichlet boundary condition of temperature at the injection zone. It can be seen that at the lower flow rate, $50\,\mathrm{L\,s^{-1}}$, average reservoir temperature decreases from 200 °C to 130.6 °C in the LTE model and to 128.2 °C in the LTNE model. Higher flow rates, however, show a drop to 125.7 °C and 123.3 °C in LTE and LTNE models, respectively.

Figure 4.20 shows that the difference between two models is initially fast for the first 25 yr, and then remains almost constant about 2 %. The average reservoir temperature differs less than the water outflow temperature between both models because a large area of the modeling domain is either at the initial temperature or has cooled down to the final temperature (figure 4.21). In areas where rock and fluid temperature have the same initial or final value, LTE and LTNE naturally show similar results. Average water temperatures underestimate the differences in the LTE and LTNE models compared to actual water outflow temperatures.

This is also seen in figure 4.22 where two dimensional $\%\Delta T_{\mathrm{w}}$ is illustrated for the whole simulated domain. The area in which the heat transfer between fluid and rock occurs (the temperature front) is easily recognized in these plots because of the larger difference between the LTE and LTNE models. It is noteworthy that the maximum value of $\%\Delta T_{\mathrm{w}}$ is higher than $\%\Delta T_{\mathrm{w(out)}}$ exceeding 7 %, which evidently occurs in the less permeable zone.

4.6. Conclusion

We numerically investigated, and quantified, fluid temperature differences that arise between models that assume either Local Thermal Equilibrium (LTE) or Local Thermal Non-Equilibrium (LTNE) to determine the impact of either assumption on the long-term behavior of geothermal systems. We developed two-dimensional models that fully couple fluid and heat transport in a continuum, and benchmarked these models using analytical solutions or experimental data. Although the LTNE approach requires more parameters to determine the heat transfer term, it does not require the local thermal equilibrium and adequately reproduces the experimental results [81] that could not be reproduced using LTE.

We performed a variety of numerical sensitivity tests on a simple geometrical numerical experiment consisting of a $1\,\mathrm{m} \times 3\,\mathrm{m}$ large host rock with a more permeable embedded layer in the middle. We studied the impact of porosity and permeability on the results of LTE and LTNE models by assigning different values and ratios to layer and host rock. These results show that the LTE model is not as sensitive to porosity changes as under the LTNE assumption.

The LTNE model predicts lower fluid temperatures than the LTE model when the porosity of the embedded layer is higher than in the surrounding rock and higher temperatures in the case of a lower layer porosity. Within fractured fractured systems, porosity distribution is critical

because it determines which model predicts the lower temperature bound. Permeability, surprisingly, does not influence the difference between the two models significantly. However, if the fracture zone permeability reduces along with the host rock, the divergence between predictions under LTE and LTNE models becomes significant.

The effects of assuming thermal equilibrium in heat production of a geothermal system is examined by modeling a generic case with a fully coupled heat and fluid flow model in a 500 m × 500 m saturated reservoir with an arbitrary heterogeneous fracture network. We show that the temperature of the produced water increases to about a 4% difference between LTE and LTNE predictions after 40 years of production. However, we also find larger differences between the two models (>7 %) in the less permeable zones. Averaging over the whole simulated domain, this difference is about 2 %, i.e. 5×10^{-4} °C per year in the reservoir. Although the differences between the two assumptions are relatively small, they could impart a non-trivial economic consequence of a commercial geothermal system over its lifetime. We only considered water in the current study, but differences may be significantly higher if other circulating fluids such as CO_2 are used for heat extraction.

Our model can be improved by including additional processes that are important. For example, we assumed a constant heat transfer coefficient for the fluid and rock heat exchange, but recent work [112] on a dynamic heat transfer coefficient that depends on fluid velocity and temperature could modify our current results. It remains an open question how both models would behave by including the effects of salinity, gravity, and partial saturation.

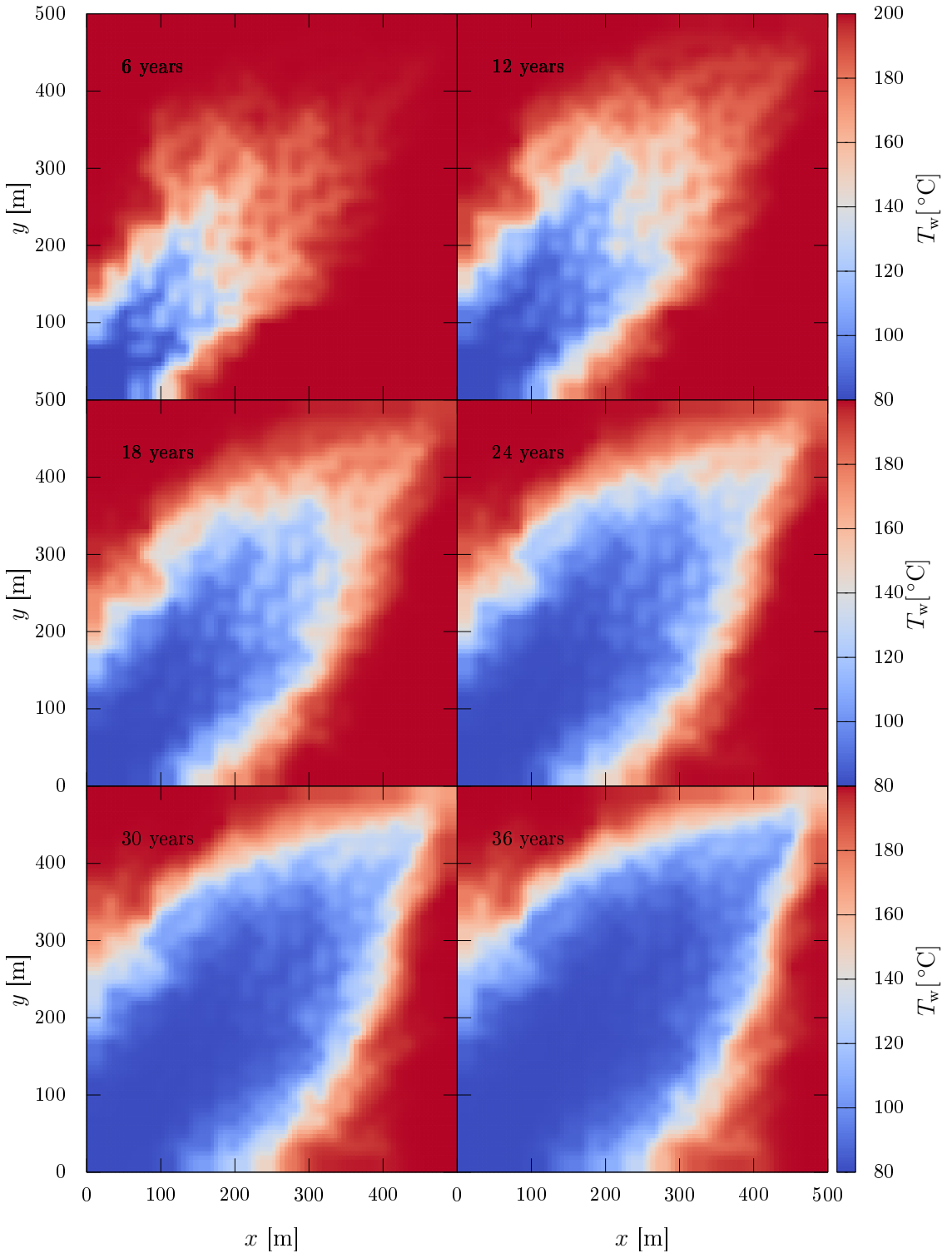

Figure 4.21.: Evolution of the water temperature field with injection rate $150\,\mathrm{L\,s^{-1}}$ at six different production steps.

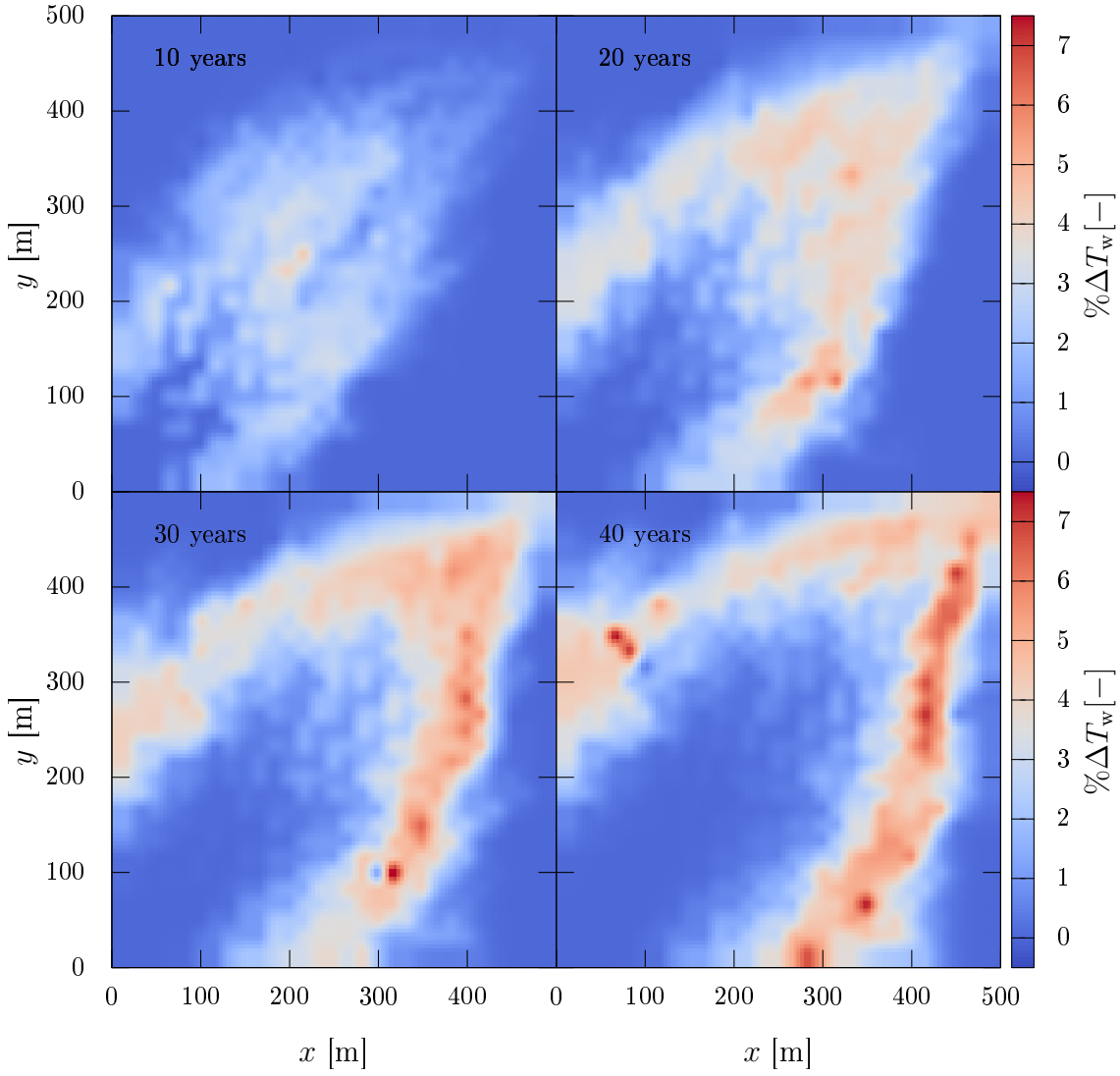

Figure 4.22.: Spatial difference between the LTE and LTNE approaches for an injection rate of $150\,\mathrm{L\,s^{-1}}$. Cooling front of the system is well observable. Maximum value of $\%\Delta T_\mathrm{w}$ exceeds 7 % which can not be seen in the outflow temperature plots.

5. A dynamic heat transfer coefficient between fractured rock and flowing fluid

Estimation of heat production remains a major challenge for geothermal industry. In continuum mechanics two main approaches need to be separated to model heat transfer between fluid and rock: local thermal equilibrium (LTE) and local thermal non-equilibrium (LTNE). While LTNE does not require the strong assumption of instantaneous local thermal equilibrium, the parameters for explicit heat transfer between rock and fluid are only loosely defined. This work focuses on the heat transfer coefficient between rock walls and flowing fluid. Based on an experimental setup with simple geometry and a steady state scenario, we derive a dynamic heat transfer coefficient dependent on fracture aperture, flow velocity and thermal parameters. We compare our model to experimental data and achieve a good agreement for most temperatures. In comparison to a static heat transfer coefficient, a dynamic coefficient changes the fluid and rock temperature distribution in the fractured system. We then show possible extensions of our dynamic approach with a simulation on reservoir scale. In opposite to existing models and empiric approaches our model intrinsically adjusts to spatial heterogeneity and temporal changes in flow and temperature field. The model is based on well-defined physical parameters which can be easily obtained from standard laboratory tests and dependent on characteristic variables like velocity and rock temperature. Our model can be extended by including more constitutive relationships linking permeability, fracture aperture, fluid pressure and heat transfer.

Published as:
T. Heinze, S. Hamidi, and B. Galvan. "A dynamic heat transfer coefficient between fractured rock and flowing fluid". *Geothermics* 65 (2017), pp. 10-16. DOI: 10/f9g653

5.1. Introduction

Numerical simulations of geothermal systems during stimulation and production phases are common prognostic tools nowadays (e.g. [31, 37, 107]). Complex fluid flow models consider phase change of the fluid or dynamic behavior of permeability and porosity ([121, 118, 35]). Yet, estimation of heat production remains a major challenge. Some of the issues related to heat transport can be addressed with a continuum approach.

Two models need to be separated in this context: In the equivalent temperature model, the fluid and rock are represented as a single continuum and a common temperature is calculated, assuming that fluid and rock reach local thermal equilibrium (LTE) instantaneously. In the context of geothermal systems and other applications this assumption might not be fully applicable as a temperature gradient between fluid and rock is essential for the system. Also a recent study shows significant differences between LTE and a method neglecting local thermal equilibrium (LTNE) for long-term production [30]. The authors of [122] show that air temperature during flow in a porous cylinder at high flow rates can also not described well by LTE. If local thermal equilibrium is neglected, heat exchange between fluid and rock is calculated using a transfer term, which depends on specific contact area A between rock and fluid, on the temperature difference $\Delta T = T_\mathrm{f} - T_\mathrm{r}$ between rock and fluid and heat transfer coefficient h. The transfered heat Q_h is then calculated as [123]:

$$Q_\mathrm{h} = hA\Delta T \ . \tag{5.1}$$

The input parameter h is, amongst others, influenced by the geometry of the fluid-rock interface and the fluid motion. So far, different approaches exist to estimate the heat transfer coefficient. One method is the use of a thermal boundary layer, assuming laminar flow along a plate with constant temperature [124]. Values calculated with this method are found to be rather high [82] and are constant in time and space like all other available approaches. For a porous medium the heat transfer coefficient can be calculated with an empirical correlation using the Nusselt number and, assuming spherical particles, the spherical diameter of the grains as described in [125]. For more complex particle geometries or a fracture system, so far a satisfying expression for h is missing. In most geothermal systems heat transfer and fluid flow primarily take place within fractures. We therefore focus on fracture geometries in this study.

A series of experiments is presented in [81] to estimate the heat transfer coefficient for a steady state case. Fluid flows through a single fracture in a rock specimen with known inflow temperature, while the rock specimen is heated from the outside. Fluid velocity, fracture aperture and temperatures of rock and fluid are varied over 78 different experiments. With the observed fluid outflow temperature, the authors present empirical power-laws concerning the dependence of h on velocity and fracture aperture [81]. The study of [81] is one of the very few conducted to study the influence of different parameters on the heat transfer coefficient.

Recently [82] renew the interpretation of these experiments by combining the experimental results with analytical solutions of heat flow in the experimental setup and was able to

derive an analytical equation for the heat transfer coefficient for the steady state case. One drawback of the solution presented in [82] is the specific adaption to the experiment, which makes it difficult to utilize the approach in a prospective geothermal simulation. This applies especially to the choice of parameters and the steady state assumption. Further h is assumed to be constant in time and space, similar to other previous studies (e.g. [30, 125, 126]). Experimental data and analytical models show dependencies between h and other system variables and parameters like flow velocity, fracture aperture and temperature which are not constant in realistic applications. Also previous studies assume a constant effective value for a whole system, not considering local heterogeneity like it may occur in permeability in a fractured system.

In this work we will examine the solution derived in [82] in more detail and derive an equation for a locally defined, dynamic heat transfer coefficient, overcoming the shortfalls mentioned above. This model is suitable for a dynamic, evolving heat transport scenario in a fractured environment and usable in a simulation of a geothermal system. We test our approach with experimental data from [81] and present a study on reservoir scale to prove the scalability of this model.

5.2. Theory

We consider a single horizontal fracture with aperture $2b$ inside an impermeable specimen with length $L = 102\,\mathrm{mm}$ and width $2R = 51\,\mathrm{mm}$ (see figure 5.1). This corresponds to the experimental setup in [81]. Water is injected into the fracture on the left side with temperature T_{in} and leaves the fracture on the right with temperature T_{out}. The specimen is heated at top and bottom with temperature T_0. In total 78 experiments with different fluid velocities, temperatures and apertures were conducted (see table A.1; originally part of the publication). Fluid velocities are assumed to be uniform and constant in the fracture.

The governing equation for rock temperature T_{r}, assuming local thermal non-equilibrium is:

$$\frac{\partial T_{\mathrm{r}}}{\partial t} = \frac{K_{\mathrm{r}}}{(1-\phi)\rho_{\mathrm{r}}c_{\mathrm{r}}}\nabla^2 T_{\mathrm{r}} + \frac{1}{(1-\phi)\rho_{\mathrm{r}}c_{\mathrm{r}}}Q_{\mathrm{h}} \ , \tag{5.2}$$

where K_α is thermal conductivity, ρ_α is density, ϕ is porosity and c_α heat capacity of phase $\alpha = \{\mathrm{r}, \mathrm{f}\}$ [123]. The heat equation of the fluid considers an additional advection term with velocity $\mathbf{v}$:

$$\frac{\partial T_{\mathrm{f}}}{\partial t} = \frac{K_{\mathrm{f}}}{\phi\rho_{\mathrm{f}}c_{\mathrm{f}}}\nabla^2 T_{\mathrm{f}} - \frac{1}{\phi\rho_{\mathrm{f}}c_{\mathrm{f}}}Q_{\mathrm{h}} - \frac{1}{\phi}\mathbf{v}\nabla(T_{\mathrm{f}}) \ . \tag{5.3}$$

For the steady state case the rock temperature can be simplified, assuming that heat conduction only takes place perpendicular to the plane [82]:

$$\frac{\partial^2 T_{\mathrm{r}}}{\partial z^2} = 0 \ . \tag{5.4}$$

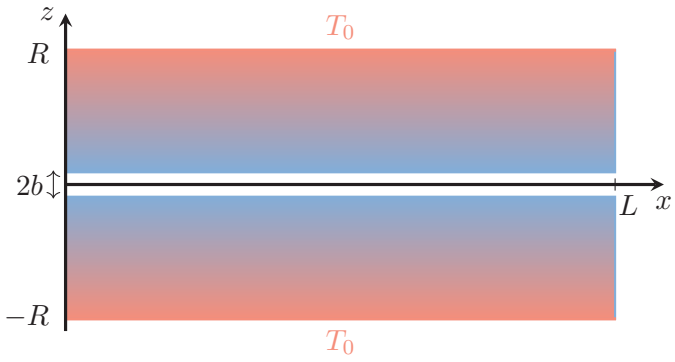

Figure 5.1.: Sketch of the experimental setup used in and for derivation of the analytical solution.

With the boundary condition at the fracture surface $z = b$:

$$K_\mathrm{r} \frac{\partial T_\mathrm{r}(x,z)}{\partial z} = -h(T_\mathrm{f}(x,b) - T_\mathrm{r}(x,b)) \ , \tag{5.5}$$

and the boundary condition at top and bottom $z = R$:

$$T_\mathrm{r}(x,R) = T_0 \ , \tag{5.6}$$

an analytical expression for rock temperature depending on fluid temperature can be derived:

$$T_\mathrm{r}(x,z) = \frac{h}{K_\mathrm{r} + hR} \left(T_0 - T_\mathrm{f}(x)\right)(z - R) + T_0 \ . \tag{5.7}$$

As shown in [82], conductivity in the water can be neglected and water flow is only one-dimensional in the experimental setup (cf. figure 5.1). Using equation (5.7) and the boundary conditions:

$$T_\mathrm{f}(x = 0) = T_\mathrm{in} \ , \tag{5.8}$$

$$T_\mathrm{f}(x = \infty) = T_0 \ , \tag{5.9}$$

an analytical solution for fluid temperature in a steady state is derived as:

$$T_\mathrm{f}(x) = T_0 + (T_\mathrm{in} - T_0) \exp\left(-x \frac{hAK_\mathrm{r}}{\mathbf{v}\rho_\mathrm{f} c_\mathrm{f}(K_\mathrm{r} + hR)}\right) \ . \tag{5.10}$$

For a known fluid temperature at position x the heat transfer coefficient can be calculated

$$h = -\frac{\mathbf{v}\rho_\mathrm{f} c_\mathrm{f} K_\mathrm{r} \ln\left(\frac{T_\mathrm{f}(x) - T_0}{T_\mathrm{in} - T_0}\right)}{xAK_\mathrm{r} + \mathbf{v}\rho_\mathrm{f} c_\mathrm{f} R \ln\left(\frac{T_\mathrm{f}(x) - T_0}{T_\mathrm{in} - T_0}\right)} \ . \tag{5.11}$$

In the study of [82] equation (5.11) was used to calculate a constant, homogeneous heat transfer coefficient for the experimental setup in a steady state with $T_\mathrm{f}(x = L) = T_\mathrm{out}$. Several improvements need to be applied to expand this idea to calculate such an effective heat transfer coefficient for geothermal applications.

First of all, this solution contains parameters, which are problem specific to the experimental setup. In the experiment, parameter R describes the shortest distance from the fracture to the heating plate, or more general, the distance to the defined temperature T_0. In the experimental setup and the analytical solution, this is the only known rock temperature. In the context of a geothermal system, R could be interpreted as some characteristic length scale of the system in terms of an influence domain, giving the shortest distance to a point where rock temperature remains constant through fluid injection. Hence, an a-priori guess of such a point is difficult, especially in long-term production, and the parameter would always remain ambiguous. We therefore propose the following approximation: for the limit $R \to 0$, T_0 becomes $T_\mathrm{r}(x)$ and the heat transfer coefficient simplifies to

$$h = -\frac{\mathbf{v}\rho_\mathrm{f}c_\mathrm{f}}{Ax} \ln\left(\frac{T_\mathrm{f}(x) - T_\mathrm{r}(x)}{T_\mathrm{in} - T_\mathrm{r}(x)}\right) \quad . \tag{5.12}$$

Using this approximation, experimental data presented in [81] and analytically calculated rock temperatures, we obtain almost similar, although slightly lower, heat transfer coefficients than calculated in [82]. Thus, this simplification has only minor influence on h but reduces the number of required parameters. The made approximation is similar to a simpler model assuming laminar flow through two plane plates with temperature T_r. Between two neighboring, discrete points the rock temperature changes only very little in time and space, compared with fluid temperature.

Equations (5.11) and (5.12) are conceived for laboratory scale domains. However, equation (5.12) could be used in field scale simulations, in a local sense, describing the heat transfer coefficient within the individual numerical cells conforming the field scale domain. This way we can reproduce local heterogeneity in the fracture network or the host rock at field scale. We can then also replace T_in with the fluid temperature of the neighboring upstream point $T_\mathrm{f}(i-1)$, if i is the point index increasing in flow direction. In the next sections we will explain the inclusion of a local and dynamic heat transfer coefficient h_dyn following equation (5.12) in a numerical simulation and its benefits in comparison to a static and effective heat transfer coefficient h_stat.

5.3. Numerical method

We implemented an explicit Euler-scheme on a finite difference grid to solve equations (5.2) and (5.3). We use a Semi-Lagrangian scheme with cubic spline interpolation to solve the advection part in the fluid temperature equation (e.g. [126, 127, 128]). For simulations on laboratory scale as well as on field scale, we use the same set of equations and similar fluid and rock parameters. Thermal conductivity of rock is $3.38\,\mathrm{W\,m^{-1}\,°C^{-1}}$ and of water $0.609\,\mathrm{W\,m^{-1}\,°C^{-1}}$. We set rock density $\rho_\mathrm{r} = 2600\,\mathrm{kg\,m^{-3}}$ and heat capacity $c_\mathrm{r} = 790\,\mathrm{J\,kg^{-1}\,K}$. On laboratory scale the spatial resolution is set to 1 mm and the setup follows the description in [82, 81].

We calculate water density and heat capacity in dependence of temperature and pressure according to [88]. Pore pressure values for the experimental setup were not published but

we estimate them using the given fluid velocities and fracture apertures as well as Darcy's law:

$$\mathbf{q} = -\frac{k}{\mu}\nabla P \ . \tag{5.13}$$

With Darcy velocity $\mathbf{q}$, permeability k, dynamic viscosity μ and pore pressure P. From Darcy velocity $\mathbf{q}$ true velocity can be calculated with the Dupuit-Forchheimer relationship $\mathbf{v} = \mathbf{q}/\phi$, but for the experimental setup true fluid velocity is given in [81].
We further use a link between a single rock fracture and permeability

$$k = \frac{b^2}{12} \ . \tag{5.14}$$

With these equations and the velocities and apertures given in [81], we calculate pore pressure gradients along the fracture to be less than 1 MPa for the experiments. With a total pressure above 0.5 MPa the water will be in the liquid phase for the temperatures used in the experiments. We therefore assume that pore pressure is small and neglect the influence of pressure on fluid properties for the laboratory experiments. In opposite to the simulation on field scale, for the laboratory experiments we set the one-dimensional fluid velocity constant in the fracture and neglect any diffusion process in the host rock because duration of each experiment is short and permeability of the host rock is low.

On field scale evolution of fluid pressure is calculated with a non-linear diffusion equation:

$$\frac{\partial P}{\partial t} = \frac{1}{\phi(\beta_\mathrm{f} + \beta_\phi)}\nabla\left(\frac{k}{\mu}\nabla P\right) \ , \tag{5.15}$$

where permeability k is strongly heterogeneous, representing a fracture network and $\beta_{\mathrm{f},\phi}$ are compressibility for fluid and rock. For the geothermal reservoir, we generate an arbitrary fracture network, over a domain of 500 m × 500 m with a spatial resolution of 10 m^2, from the lower left to the upper right corner by marking grid points as 'fractured' or 'unfractured' (figure 5.2). For simplicity we assume that each fractured cell only contains one single, plane fracture with aperture b.

We distribute aperture over all fractured cells following a normal distribution with a mean of 18.5×10^{-6} m and a standard derivation of 1×10^{-6} m. Background permeability of an unfractured grid cell is 1×10^{-16} m^2. The final two-dimensional distribution of aperture is shown in figure 5.2. From aperture we calculate permeability using equation (5.14). Although this may contradict the hypothesis of a single fracture, for simplicity we assume permeability to be isotropic. Overpressure in the injection hole is 10 MPa. Porosity is set to 0.02, injection temperature of water is 30 °C. Heat transfer is assumed to only take place in fractures. The rock is fully saturated and initial temperature of fluid and rock is 120 °C. On field scale water density, viscosity and heat capacity depend on fluid temperature and pressure, assuming hydrostatic pressure at 4 km depth. The shown fracture network is oriented horizontally, therefore there are no gravity effects.

While equations for h derived above consider steady state, we use them in a time evolving equation, assuming that changes with time are slow compared to the numerical time-step. As long as this is true, we assume h_dyn to remain quasi-static. Figures 5.4 and 5.8 show that this

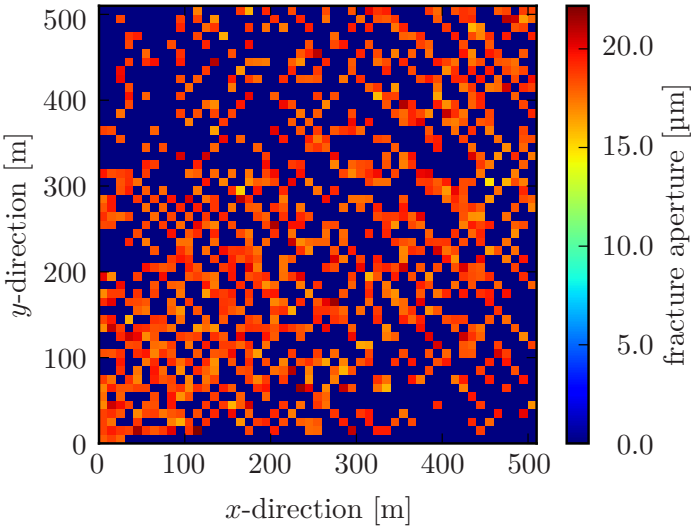

Figure 5.2.: Heterogeneous distribution of aperture on an arbitrary fracture network, used for the simulation of static and dynamic heat transfer coefficients in field scale.

assumption is valid, because h changes only over long time periods, compared with a time-step less than a fraction of a second. We do not assume h_{dyn} to be spatially constant in the system but calculate h_{dyn} at every time-step for every grid point separately.

5.4. Results

We simulate all 78 experiments from [81]. At first we use the constant heat transfer coefficient derived by [82]. The simulation results for the outflow fluid temperature coincide very well with the experimental ones (see table A.1). This proves that our modelling framework is working well and the full set of dynamic equations converges towards the analytical solution presented in [82]. The good agreement between these simulations and the experimental observations is to be expected because the value of h_{stat} is chosen to match the experimental observed outflow temperature.

In figure 5.3 change in outflow fluid temperature over time with h_{stat} are shown in dashed lines for some experiments. The observed values are marked with circles and a tolerance region of around 1 °C. The system reaches steady state after around 700 seconds for both simulated cases, with static and dynamic h. The estimated outflow temperatures with the dynamic approach are in general roughly in a 3 °C window around the ones measured in the experiments. Our model tends to overestimate the outflow temperature in most cases, with a better match for higher fluid velocities. For a rock temperature of 120 °C the temperatures are estimated very well with the dynamic approach while for a rock temperature of 140 °C our model deviates stronger from the experimental data. Outflow temperatures calculated with h_{dyn} agree well in most cases with the temperatures estimated by a theoretical model assuming similar temperature at the fluid-rock interface (Model 1 in [82], see table A.1).

When dynamic heat transfer coefficient h_{dyn} is used, it shows strong variability along the

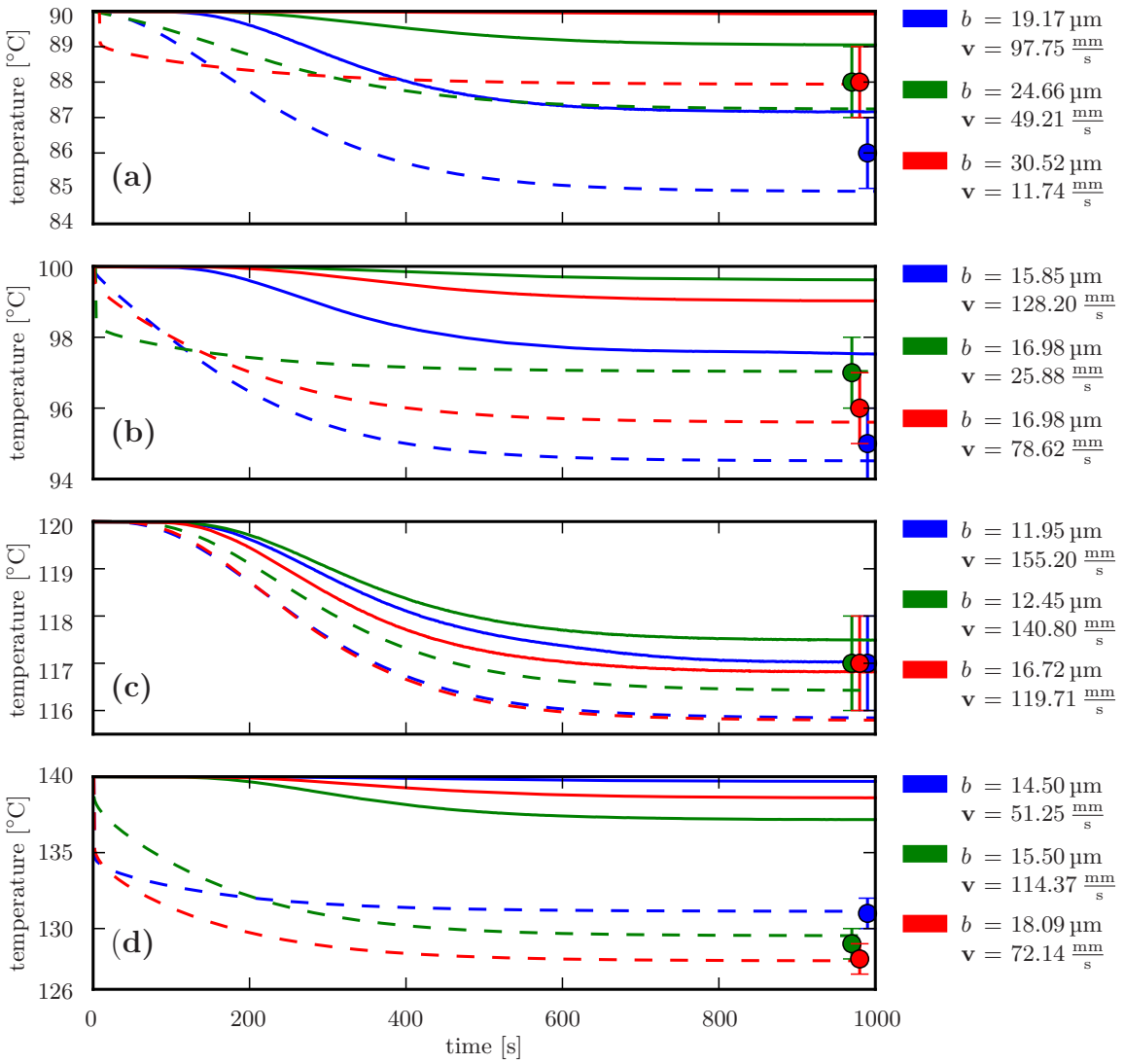

Figure 5.3.: Outflow temperature on the right for a maximum rock temperature of (a) 90°C, (b) 100°C, (c) 120°C, (d) 140°C. Observed values shown as circles with tolerance region. Dashed lines show simulation results with h_{stat}, solid lines with h_{dyn}.

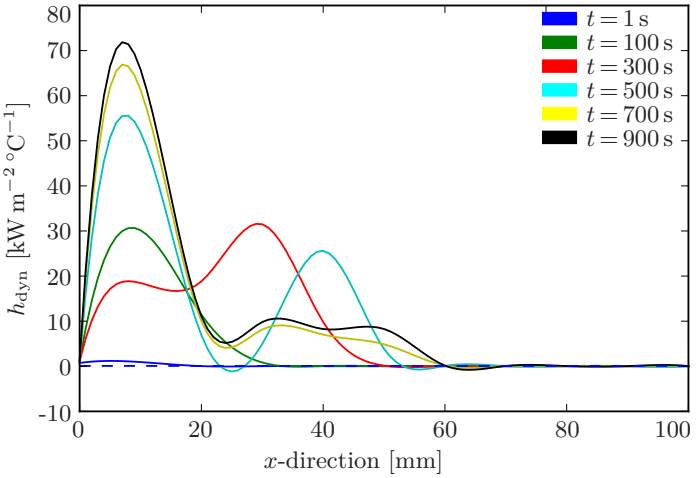

Figure 5.4.: Dynamic heat transfer coefficient for several timesteps after injection along the fracture. Dashed line shows calculated static heat transfer coefficient from [82].

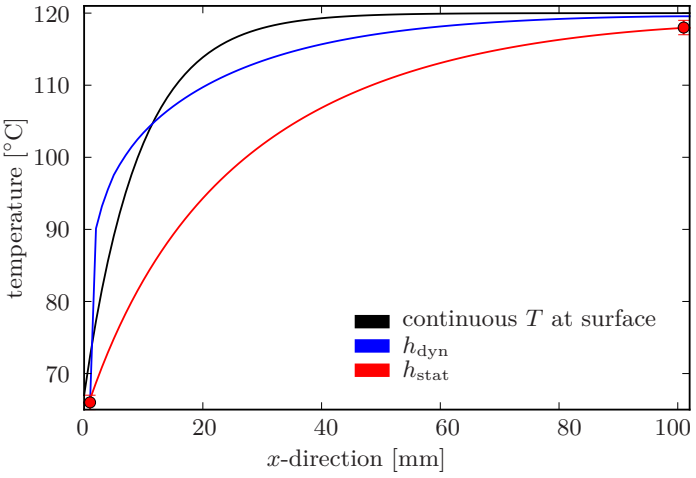

Figure 5.5.: Steady state fluid temperature profile along the fracture with h_{stat} following [82], h_{dyn} and assuming thermal equilibrium at the fracture surface following Model 1 in [82].

fracture. In early stages of the simulation, when temperature gradient between fluid and rock is higher at the beginning of the fracture, the coefficient is higher and its value declines towards the end of the fracture. Figure 5.4 shows that the heat transfer coefficient grows with time and in flow direction. For later stages of the simulation, only small variations can be observed as temperature distribution reaches steady state. After around 60 mm along the fracture, the dynamic heat transfer coefficient h_{dyn} drops below the level of the static value h_{stat} (dashed line in figure 5.4).

Fluid temperature distribution along the fault diverges between the models with a dynamic or static heat transfer coefficient (figure 5.5). For comparison we also included a model derived in [82], assuming a similar temperature for rock and fluid at their interface. This model shows a very rapid increase of temperature at the beginning and temperature does not change beyond 60 mm along the fault.

As already discussed in [82] this approach overestimates the steady state fluid temperature. In the model using h_{dyn}, the temperature increases rapidly close to the inflow point as well and reaches the final outflow temperature after 50 mm. Using h_{stat}, temperature

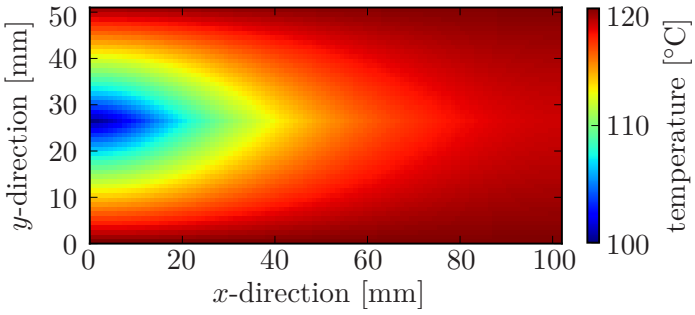

Figure 5.6.: Rock temperature for the experiment in the steady state case.

increases steadily along the fracture till its end. For a better evaluation inflow and outflow temperature are marked in the figure 5.5. In the experiment the temperature profiles were not measured. Therefore, temperature profiles of the different models can not be compared with measured data and can only be interpreted as characteristic for the models used.

The two dimensional temperature distribution of the rock is strongly altered around the injection point with a drop in temperature of around 20 °C, and increases with distance from the injection point. The rock temperature also shows very little variation along the fracture beyond 50 mm (figure 5.6). On field scale, we simulated 25 years of production. In opposite to the experimental setup described above no steady state is reached.

Figure 5.7 shows the outflow temperature over time for three different scenarios: $h_{\mathrm{stat}} = 90\,\mathrm{W\,m^{-2}\,°C^{-1}}$, $h_{\mathrm{stat}} = 900\,\mathrm{W\,m^{-2}\,°C^{-1}}$ and h_{dyn}. The temperature starts to drop after around 7 years and a rapid drop is observed after around 15 years in all cases. In the study of [30] similar dynamics were obtained for the outflow temperature.

The simulation using h_{dyn} shows a slightly later but therefore more rapid drop in outflow temperature than the two cases with h_{stat}. The one with higher h_{stat} drops less rapid than the one with lower h_{stat} but differences between both are small. The dynamic heat transfer coefficient following equation (5.12) evolves over time and space at field scale similar to the experiments in the laboratory.

At early times the heat transfer coefficient has large values close to the injection point. With time its maximum value moves away from the injection point and larger values are observed towards the outflow (figure 5.8). This is the same behaviour as seen in figure 5.4 for the laboratory experiment. Though, due to the heterogeneous distribution of fractures in the field, the tendency is less clear. The absolute values for h_{dyn} are slightly lower on field scale than on laboratory scale, which is mainly due to lower fluid velocities.

5.5. Discussion and Conclusion

We presented a new approach to calculate the heat transfer coefficient between rock and flowing fluid in a fractured system in which we consider dynamic changes and local heterogeneity. We validated it with a comparison between simulation results and laboratory

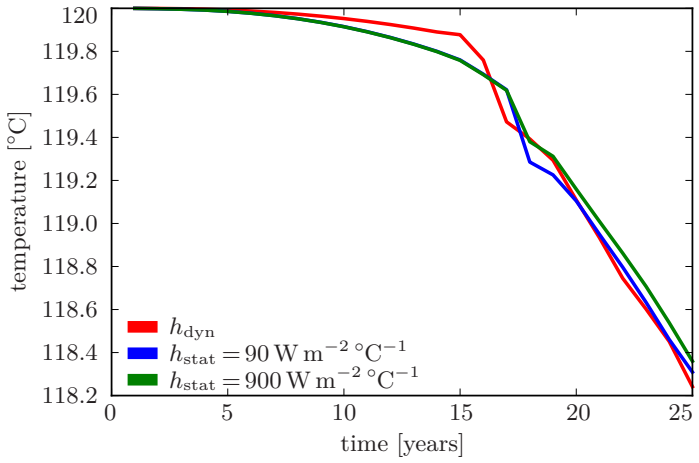

Figure 5.7.: Outflow temperature of geothermal reservoir simulation over time.

experiments. Our approach reproduced most of the experiments very well. However, it had the tendency to overestimate the water temperature, similar to other previously reported models ([30, 82]). A strong divergence of more than 5 °C between our model predictions and the experimental results exists for the highest temperature tested in the experiments, a rock temperature of 140 °C. The experimental data for this temperature is partially inconclusive in itself, showing a way stronger velocity dependency than for other rock temperatures. Also it is noticeable that in experiments with this rock temperature fluid outflow temperature even for the lowest fluid velocity is several degrees lower than the rock temperature. In experiments with lower rock temperatures the outflow temperature for similar apertures and flow velocities is close to rock temperature.

Already the study of [82] showed that experimental data for 140 °C, and partially also for 100 °C rock temperature, behave differently than for the other rock temperatures. A possible reason might be the unknown pressure conditions in which the experiments were performed and which might influence the fluid behaviour. Together with the inconsistencies in the experimental dataset further experimental work is necessary to further evaluate our model. Especially temperature profiles along fracture surfaces are important to validate and calibrate the model. For a dynamic heat transfer coefficient experiments with variable flow velocity in a more complex fracture geometry are needed. A comparison of our model with real values on field scale also needs to be evaluated.

With a simple case study on a 500 m times 500 m field with an arbitrary fracture network, we showed that our model scales well and can also be used for geothermal simulations. The absolute values for h_{dyn} are higher in this work than in a previous study for h_{stat} but the same study also shows that the outflow temperature does not strongly depend on h for the steady state case [82]. On the other hand, h strongly influences the temperature distribution along the fracture, where experimental data is missing but which is important for long-term simulations of geothermal production sites [30].

Our approach improves existing models as our model intrinsically adjusts the heat transfer coefficient h to dynamic changes in the system, like a change in flow velocity, and can cover heterogeneous domains. We calculate h locally instead of assuming a constant,

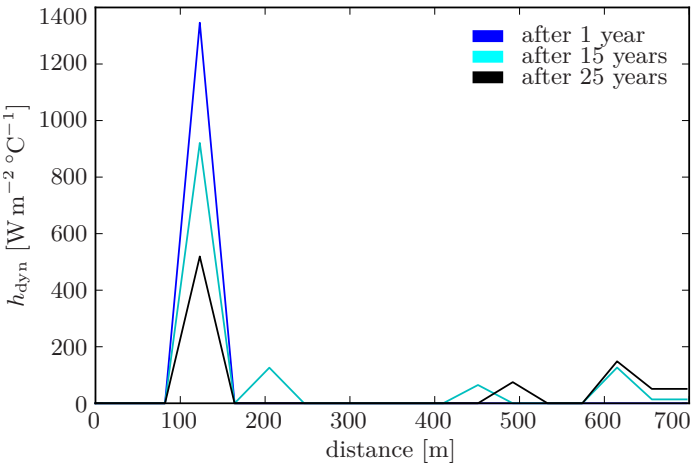

Figure 5.8.: Evolution of dynamic heat transfer coefficient for several time-steps after the injection in distance from the injection point along a continuous fluid path.

effective value. We reduced the number of parameters to enable an adaption from laboratory experiments to real field applications. Further, all input parameters are well defined and can be obtained easily with field observations, laboratory testing and numerical simulations.

So far, we do not account for rock or fluid specific behaviour, like surface roughness or tortuosity. In the study of [129] surface roughness was shown to have a major influence on heat transfer between rock and flowing fluid. In our model surface roughness would influence the hydraulics due to a variable fracture aperture and a resulting variable permeability but also due to an increased heat transfer area A and probably the heat transfer coefficient h. Besides the numerical study of [129], to our best knowledge no experimental study exists studying the effect of surface roughness in detail.

With a yet to develop model on grain scale it might be possible to include parameters like surface roughness and explain the difference in estimated and observed outflow temperatures in the experiment. Though, we consider a more detailed experimental study over a broader range of temperatures essential to progress. Only this way we can discount that the divergence between experimental data and theoretical models is not based on experimental limitations.

Naturally, our model for a dynamic heat transfer coefficient can be coupled to a way more advanced fluid flow model than the one applied here. Also dynamic fluid flow parameters, e.g. a pressure dependent permeability [20], can be incorporated into the model using equation (5.14).

6. Discussion and future research perspective

This thesis studies fluid-rock interactions during fluid flow, heat and mass transport in the Earth's subsurface and the effects of these couplings on natural phenomena and industrial applications. For this purpose, a numerical model is developed. Thermal, hydraulic and non-reactive mass transport processes are coupled together and influence each other by changing fluid and rock properties. In the presented manuscripts, different physical and numerical aspects of these interactions are studied and analyzed.

The first manuscript is about asymmetric fluid intrusion in deep reservoirs. It explains how stress, temperature and salt concentration gradients can influence fluid propagation patterns. In many fluid-triggered seismic data sets, it can be seen that the vertical distribution of events are not equal, and upward propagation is faster than downward (e.g. [4, 91, 93]). Previous studies justify this effect by a pressure-dependent permeability that results in a higher upward fluid diffusivity. However, large permeability changes over the limited spatial scales around the injection point may be unrealistic. Besides, the presence of a strong thermal gradient in many sites where this phenomenon has been observed, indicates a relationship between higher upward flow rates and heat transport. Another possible cause for this phenomenon could be buoyancy due to salinity gradients, which have been neglected so far. In this section, the effects of temperature and salinity as well as pressure-dependent permeability have been investigated in detail by simulating pressure diffusion in a vertical saturated profile with hydrostatic pressure, while fluid is injected in the middle.

To analyze the impact of stress, a nonlinear flow in absence of thermal and salinity gradients is modeled assuming a widely used pressure-dependent porosity and permeability relationship. The results show a clear higher upward diffusion over 6 months of injection. The difference between up- and downward diffusion however, shows a reduction after about three months. To study temperature effects, fluid flow in a homogeneous medium with a thermal gradient is simulated solving pressure diffusion and temperature advection-diffusion equations. Fluid viscosity and density are both temperature-dependent and play adverse roles in pressure diffusion. Due to the initial conditions, viscosity decreases with depth, causing a higher downward diffusivity in the first place. This changes as temperature spreads in the system and buoyancy driven upward flow overcomes the downward flow. The time in which density effect exceeds viscosity, depends on temperature and pressure profiles. Salinity influence is studied by assuming different salt concentrations for injected fluid and system. Buoyancy effect caused in this case, is small compared to the stress and temperature impacts.

The study goes further by coupling these effects in one scenario and model a case where fluid with higher temperature is injected to a system with temperature, porosity and permeability gradients. The simulation results show a steadily asymmetric fluid pressure with a strong tendency to diffuse upward. Up to this point, it is shown that coupling stress and thermal effects in subsurface fluid flow is much more complex than predicted before.

Fluid flow in fractured porous media is described by a non-linear pressure diffusion equation. Modeling heat flow in porous media is more complicated not only because of its convective nature, but since fluid and rock temperatures are not necessarily the same despite their direct interactions. That means two partial differential equations have to be solved which are coupled with a heat exchange term between fluid and solid phases. In order to simplify implementation and reduce computational costs, it is common to assume that both phases are in thermal equilibrium and therefore, heat flow can be modeled by solving a single equation. Thermal properties like conductivity and heat capacity are then weighted with porosity. Many of the state-of-the-art solvers and studies are based on this assumption but recent studies show that this simplification may not be accurate in some cases ([52, 30, 111]).

The impact of local thermal equilibrium (LTE) assumption on simulations in continuum mechanics, is still not fully understood. In the second manuscript in this work, the LTE assumption is examined and compared to the local thermal thermal non-equilibrium (LTNE) model in different scenarios to make a better understanding of the circumstances under which this simplification is acceptable.

A two-dimensional code is developed for coupled fluid flow and heat transport in the LTE and the LTNE models. In order to validate the code, either experimental data or analytical solutions has been used. The heat exchange term in LTNE model is parametrized using fluid-to-solid Nusselt number. In spite of good agreement with analytical solutions, the LTE module is not able to reproduce the laboratory data of Zhao and Tso [81]. Therefore, a simple set-up similar to the one used in their experiments, consisting of a host rock with an embedded layer in the middle, is used to perform various numerical sensitivity tests on the LTE and LTNE models in detail.

It is shown that temperature predicted by the LTE is not sensitive to porosity, although the LTNE predicted fluid temperature changes due to porosity modifications. Numerical experiments on different permeabilities show a higher LTE-LTNE divergence in less permeable rocks where fluid velocity is lower. Even though this divergence grows over 5 %, it is still not clear whether the LTE is valid in larger spatial and time scales. To scrutinize these conditions, a hypothetical geothermal system under both LTE and LTNE assumptions is simulated during 40 years of production. The output fluid temperatures predicted by the LTNE model are lower than those using the LTE and the difference between the two models grows over 7 % in low permeable zones. According to Richards et al. [120], a Hot Dry Rock system may not have significant temperature fall after 20 years of production. Hence, a 7 % divergence in production temperature estimation, can decide about economical feasibility of a project. Moreover, the LTNE model provides a lower limit for fluid temperature here,

which is of great advantage regarding long-term production estimation of a geothermal power plant.

Knowing that LTE-LTNE difference increases in low permeable zones, suggests that it may be best to apply the LTNE model in deep reservoirs which are of great interest in industrial applications where precise evaluation of investment risks is critical. As explained above, this model is based on two coupled differential equations for fluid and solid phases. The coupling term however, is a major problem in numerical implementation and is defined as constant for limited geometries in previous works ([125, 124]).

The last part of this work focuses on heat transfer between rock walls and a flowing fluid. Zhao recently derived an analytical solution for heat transfer coefficient h, which is based on a set of experiments done by Zhao and Tso, where water is injected into a rock specimen with a single fracture in between [81, 82]. Inflow velocity and temperature are known and the rock is heated at the top and bottom which leads to a steady state case. Assuming a constant h, he can calculate the outflow temperature at the steady state. Despite good agreement with the measurements, his model cannot describe the spatial and temporal dynamics of the heat transport. His solution is not applicable in the absence of a steady state. Moreover, similar to the previous parametrization, his method neglects heterogeneities of the system and therefore can not be utilized in deep reservoir simulations. Here a dynamic h is derived based on the same experiments and is dependent on flow velocity, fracture aperture and thermal parameters. The dynamic h is extremely variable in time and space and declines strongly along the fracture.

This model intrinsically adjusts to temporal flow and thermal changes as well as spatial heterogeneities of the system. Hence, an extended version of this approach is derived and applied successfully to a simulation of a fractured geothermal system. For simplicity, fractured cells of the grid in this scenario are assumed to include only one single, plane fracture. The simulation scales well and outflow temperature shows similar dynamics as in the study of Shaik et al. [30]. Computed dynamic h near the injection area is much higher than previous common static values. This value has a significant influence on the temperature distribution along fractures, from which no measurements are available and therefore it is an essential factor in modeling reservoir dynamics. This approach can be further improved by including surface roughness parameters and adapting other fracture geometries.

Concluding, this thesis underlines the importance of coupled fluid and heat flow and the wide spectra of natural and industrial phenomena that can be described through this coupling. It shows the scenarios in which the state of the art THC simulators with the local thermal equilibrium approach may overestimate fluid pressure and temperature. These scenarios are particularly interesting for geothermal systems that require an accurate prediction of the thermal field for assessing financial feasibility of a project. So far, a major weak spot of the alternative model of local thermal non-equilibrium was the heat exchange term between fluid and solid. This can now be resolved by a dynamic heat transfer coefficient which is introduced in this work and can be implemented conveniently in the existing solvers. With the presented work, it is now possible to study coupled heat and fluid flow in field scale using

complex models in a dynamic environment. The developed model will improve the state of the art simulations for natural phenomena and industrial applications.

The next step in model development of industrial applications are the inclusion of reactive flow coupled to the LTNE model. This will strengthen the coupling as heat is generated during chemical reactions and porosity and permeability will be altered by the erosion and deposition of material. The developed code is able to solve Richards equation and therefore has the potential to model two-phase fluid flow. However, Richards approximation is not valid in deep reservoirs. A further improvement is modeling multiphase flow without this approximation. It needs more EOS for fluids that will also increase the possible scenarios and applications to study, e.g. considering (supercritical CO_2). Though, this will increase computational complexity by several magnitudes due to the possible phase change and mixing with other fluids, like in water solved CO_2. However, experimental data is rare on heat transfer between host rock and non-water liquids. For benchmarking and model development further laboratory tests are required.

The fully coupled numerical code can be applied to model two-dimensional fluid flow, mass and heat transport using LTE or LTNE in laboratory as well as field scale. Upgrading to three-dimensions would be a great improvement, then the anisotropic nature of the continuum representation, can be implemented in a permeability tensor. Moreover, the heat transfer coefficient model, can be extended for fractures with diverse geometries. One drawback of this model is the small time-step and long simulation time due to FDM that can be overcome using graphics processing units (GPU) as computational platform [130]. Another way to overcome the time-step problem is using implicit methods, though it requires more computational power. A combination of implicit and explicit methods is still open to try. In addition, coupling to rock mechanics simulators is possible due to the modular structure of the code. This allows studying thermal plasticity effects which are an important part of the fluid-rock interactions specifically where temperature difference between rock and fluid is high, which is the case in geothermal systems and underground storage of carbon dioxide.

A. Appendix

Table A.1.: Experimental results and model predictions for water flow through a single fracture. All temperatures given in [°C]. Experimental data by [81], Model 1 by [82].

Nr.	T_{rock}[°C]	b [µm]	$\mathbf{v}$[mm s^{-1}]	T_{in}	$T_{\text{out}}^{\text{exp}}$	$T_{\text{out}}^{\text{Model 1}}$	$T_{\text{out}}^{h_{\text{stat}}}$	$T_{\text{out}}^{h_{\text{dyn}}}$
1	90	19.17	10.63	42	87	90	87.14	89.96
2			15.31	42	87	90	87.08	89.94
3			20.52	41	87	90	87.01	89.91
4			25.54	40	87	90	86.95	89.88
5			30.08	39	87	90	86.96	89.83
6			50.26	37	87	89.95	86.59	89.47
7			76.46	34	87	89.42	86.17	88.48
8			97.75	31	86	88.35	84.92	87.16
9		24.66	23.06	41	88	90	87.8	89.84
10			28.22	40	88	90	87.7	89.75
11			35.21	38	88	90	87.55	89.58
12			49.21	36	88	90	87.25	89.05
13		26.56	7.18	44	88	90	88.07	89.97
14			10.41	43	88	90	88.01	89.95
15			12.1	42	88	90	87.98	89.94
16			14.43	41	88	90	87.93	89.92
17			18.59	40	88	90	87.84	89.87
18		30.52	4.44	44	88	90	88.11	89.97
19			6.25	44	88	90	88.07	89.97
20			8.2	43	88	90	88.02	89.95
21			9.41	43	88	90	88	89.95
22			10.96	42	88	90	87.95	89.93
23			11.74	41	88	90	87.94	89.92
24	100	15.85	42.25	65	96	100	96.02	99.84

Table A.1.: continued on the following page

Table A.1.: Experimental results and model predictions (continued)

25			60.86	64	96	99.97	96.07	99.64
26			82.3	62	96	99.78	95.75	99.23
27			102.57	60	96	99.35	95.58	98.64
28			128.2	59	95	98.48	94.52	97.55
29		16.44	40.3	62	95	100	95.07	99.83
30			60.02	59	95	99.95	94.91	99.57
31			66.09	59	95	99.91	94.87	99.46
32			78.6	58	95	99.76	94.77	99.16
33		16.98	25.88	61	97	100	97.04	99.92
34			53.73	57	96	99.97	95.85	99.62
35			59.46	57	96	99.94	95.8	99.52
36			70.24	56	96	99.84	95.7	99.28
37			78.62	55	96	99.7	95.61	99.03
38		21.16	22.4	54	94	100	94.16	99.89
39			32.78	54	94	100	94.05	99.78
40			42.03	53	94	99.97	93.95	99.6
41			63.5	50	94	99.66	93.68	98.89
42			77.45	46	93	99.09	92.53	98.09
43	120	11.95	63.38	71	117	119.99	116.8	119.72
44			83	67	117	199.94	116.6	119.44
45			106.21	64	117	119.71	116.37	118.95
46			129.64	62	117	119.23	116.15	118.2
47			155.2	59	117	118.35	115.85	117.03
48		12.45	71.11	66	118	119.95	117.96	119.57
49			102.42	62	118	119.55	117.6	118.9
50			140.8	58	117	118.2	116.43	117.5
51			167.6	56	117	116.72	0	116.04
52			203.72	55	117	114.36	0	114.01
53		16.72	63.8	61	118	119.89	117.32	119.26
54			84.17	57	117	119.46	116.94	118.47
55			119.71	64	117	118.03	115.8	116.82
56	140	14.5	51.25	84	131	139.99	131.14	139.69

Table A.1.: continued on the following page

Table A.1.: Experimental results and model predictions (continued)

57		71.17	81	131	139.91	130.97	139.32
58		95.48	80	131	139.52	130.77	138.6
59		118.95	79	131	138.74	130.61	137.61
60	15.5	69.42	78	130	139.88	129.97	139.21
61		93.92	74	130	139.34	129.71	138.26
62		114.37	73	129	138.47	129.53	137.18
63		135.77	71	128	137.14	129.32	135.73
64	16.54	8.47	78	137	140	137.21	139.97
65		14.53	75	134	140	134.27	139.94
66		23.83	72	131	140	131.31	139.89
67		36.1	69	126	140	126.37	139.75
68		45.75	67	124	139.99	124.33	139.58
69	18.09	32.11	81	128	140	128.32	139.8
70		44.12	79	128	139.98	128.21	139.6
71		55.29	75	128	139.89	128.08	139.3
72		72.14	72	128	139.5	127.88	138.62
73		85.11	70	128	138.91	127.71	137.86
74	19.72	24.54	79	131	140	131.26	139.85
75		36.8	75	131	139.99	131.09	139.66
76		44.4	72	128	139.97	128.12	139.45
77		75.71	66	127	139.17	126.74	137.89
78		89.09	63	127	138.3	126.71	136.78

List of acronyms

ATES Aquifer Thermal Energy Storage

BTES Bore-hole Thermal Energy Storage

BHE Bore-hole Heat Exchanger

CCS Carbon Capture and Sequestration

CTES Cavern or mine Thermal Energy Storage

DFN Discrete Fracture Network

EGS Enhanced Geothermal System

EOS Equation-Of-State

FEM Finite Element Method

FVM Finite Volume Method

FDM Finite Differences Method

FTCS Forward-Time Central-Space

GPU Graphics Processing Unit

GUI Graphical-User-Interface

IFD Integral Finite Differences

LTE Local Thermal Equilibrium

LTNE Local Thermal Non-Equilibrium

OGS OpenGeoSys

PDE Partial Differential Equation

PETSc Portable, Extensible Toolkit for Scientific Computation

REV Representative Elementary Volume

STES Seasonal Thermal Energy Storage

THMC Thermo-Hydro-Mechanical-Chemical process

List of figures

List of tables

Bibliography

[1] S. A. Miller, C. Collettini, L. Chiaraluce, M. Cocco, M. Barchi, and B. J. P. Kaus. "Aftershocks driven by a high-pressure CO_2 source at depth". *Nature* 427 (2004), pp. 724–727. DOI: 10/bnbk2h (cit. on pp. 1, 3, 17, 36, 46).

[2] F. Waldhauser, D. P. Schaff, T. Diehl, and E. R. Engdahl. "Splay faults imaged by fluid-driven aftershocks of the 2004 Mw 9.2 Sumatra-Andaman earthquake". *Geology* 40.3 (2012), pp. 243–246. ISSN: 0091-7613. DOI: 10/fxz54q (cit. on p. 1).

[3] D. R. Shelly, D. P. Hill, F. Massin, J. Farrell, R. B. Smith, and T. Taira. "A fluid-driven earthquake swarm on the margin of the Yellowstone caldera". *Journal of Geophysical Research: Solid Earth* 118.9 (2013), pp. 4872–4886. ISSN: 2169-9356. DOI: 10/cc83 (cit. on pp. 1, 34).

[4] M. O. Häring, U. Schanz, F. Ladner, and B. C. Dyer. "Characterisation of the Basel 1 enhanced geothermal system". *Geothermics* 37.5 (Oct. 2008), pp. 469–495. ISSN: 03756505. DOI: 10/dp2vcq (cit. on pp. 1, 5, 34, 87).

[5] M. Chijimatsu, T. S. Nguyen, L. Jing, J. De Jonge, M. Kohlmeier, A. Millard, A. Rejeb, J. Rutqvist, M. Souley, and Y. Sugita. "Numerical study of the THM effects on the near-field safety of a hypothetical nuclear waste repository - BMT1 of the DECOVALEX III project. Part 1: Conceptualization and characterization of the problems and summary of results". *International Journal of Rock Mechanics and Mining Sciences* 42.5-6 SPEC. ISS. (2005), pp. 720–730. DOI: 10/cz93j2 (cit. on p. 1).

[6] M. Chijimatsu, T. S. Nguyen, L. Jing, J. De Jonge, M. Kohlmeier, A. Millard, A. Rejeb, J. Rutqvist, M. Souley, and Y. Sugita. "Numerical study of the THM effects on the near-field safety of a hypothetical nuclear waste repository - BMT1 of the DECOVALEX III project. Part 2: Effects of THM coupling in continuous and homogeneous rocks". *International Journal of Rock Mechanics and Mining Sciences* 42.5-6 SPEC. ISS. (2005), pp. 720–730. DOI: 10/cz93j2 (cit. on p. 1).

[7] K. B. Min, J. Rutqvist, C. F. Tsang, and L. Jing. "Thermally induced mechanical and permeability changes around a nuclear waste repository—a far-field study based on equivalent properties determined by a discrete approach". *International Journal of Rock Mechanics and Mining Sciences* 42.5-6 (2005), pp. 765–780. DOI: 10/d5c2w4 (cit. on p. 1).

[8] M. Lupi. "High-resolution simulation of fluid flow in active hydrothermal systems: Applications to the Tjörnes Fracture Zone and Asklja Volcanic complex in Iceland". PhD thesis. Heriot-Watt University, 2010 (cit. on p. 1).

[9] L. M. Cathles. "Scales and Effects of Fluid Flow in the Upper Crust". *Science* 248.4953 (1990), pp. 323–329. ISSN: 0036-8075. DOI: 10/c4pfhh (cit. on p. 1).

[10] M. Bloemendal, T. Olsthoorn, and F. van de Ven. "Combining climatic and geo-hydrological preconditions as a method to determine world potential for aquifer thermal energy storage". *Science of The Total Environment* 538 (2015), pp. 621–633. ISSN: 0048-9697. DOI: 10/f7vwrc (cit. on p. 1).

[11] R. Bertani. "World geothermal power generation in the period 2001–2005". *Geothermics* 34.6 (2005), pp. 651–690. ISSN: 0375-6505. DOI: 10/bmd6b6 (cit. on p. 2).

[12] G. Jansen and S. A. Miller. "On the Role of Thermal Stresses during Hydraulic Stimulation of Geothermal Reservoirs". *Geogluids* 2017 (2017). Article ID 4653278. DOI: 10/gbnnzx (cit. on p. 2).

[13] S. Emmanuel and B. Berkowitz. "An experimental analogue for convection and phase separation in hydrothermal systems". *Journal of Geophysical Research: Solid Earth* 111.B9 (2006). ISSN: 2156-2202. DOI: 10/bqpjk8 (cit. on p. 2).

[14] C. H. Sondergeld and D. L. Turcotte. "An experimental study of two-phase convection in a porous medium with applications to geological problems". *Journal of Geophysical Research* 82.14 (1977), pp. 2045–2053. ISSN: 2156-2202. DOI: 10/dtxw8s (cit. on p. 2).

[15] K. Roth. *Soil Physics Lecture Notes, V2.2.* 2012 (cit. on pp. 3, 11).

[16] J. Rutqvist and C. F. Tsang. "A study of caprock hydromechanical changes associated with CO2-injection into a brine formation". *Environmental Geology* 42.2-3 (2002), pp. 296–305. DOI: 10/fdjhs4 (cit. on pp. 3, 17, 36, 55, 65).

[17] W. F. Brace, J. B. Walsh, and W. T. Frangos. "Permeability of granite under high pressure". *Journal of Geophysical Research* 73.6 (1968), pp. 2225–2236. ISSN: 2156-2202. DOI: 10/d942rm (cit. on p. 4).

[18] Y. Bernabe. "The effective pressure law for permeability during pore pressure and confining pressure cycling of several crystalline rocks". *Journal of Geophysical Research: Solid Earth* 92.B1 (1987), pp. 649–657. ISSN: 2156-2202. DOI: 10/d7rbhj (cit. on p. 4).

[19] T. Heinze, B. Galvan, and S. A. Miller. "Modeling porous rock fracturing induced by fluid injection". *International Journal of Rock Mechanics and Mining Sciences* 77 (2015), pp. 133–141. ISSN: 1365-1609. DOI: 10/f7f6zr (cit. on pp. 4, 55).

[20] S. A. Miller. "Modeling enhanced geothermal systems and the essential nature of large-scale changes in permeability at the onset of slip". *Geofluids* 15.1-2 (2015), pp. 338–349. DOI: 10/f6xxjp (cit. on pp. 4, 34, 66, 86).

[21] S. Wang, Z. Huang, Y. Wu, P.H. Winterfeld, and L.E. Zerpa. "A semi-analytical correlation of thermal-hydraulic-mechanical behavior of fractures and its application to modeling reservoir scale cold water injection problems in enhanced geothermal reservoirs". *Geothermics* 64 (2016), pp. 81–95. ISSN: 0375-6505. DOI: 10/f9btfm (cit. on p. 4).

[22] H. H. Gerke and M. Th. van Genuchten. "A dual-porosity model for simulating the preferential movement of water and solutes in structured porous media". *Water Resources Research* 29.2 (1993), pp. 305–319. ISSN: 1944-7973. DOI: 10/dfg2vf (cit. on p. 4).

[23] H. H. Gerke and M. Th. van Genuchten. "Evaluation of a first-order water transfer term for variably saturated dual-porosity flow models". *Water Resources Research* 29.4 (1993), pp. 1225–1238. ISSN: 1944-7973. DOI: 10/dbjk8q (cit. on p. 4).

[24] C. E. Feehley, C. Zheng, and F. J. Molz. "A dual-domain mass transfer approach for modeling solute transport in heterogeneous aquifers: Application to the Macrodispersion Experiment (MADE) site". *Water Resources Research* 36.9 (2000), pp. 2501–2515. ISSN: 1944-7973. DOI: 10/d7fpt2 (cit. on p. 4).

[25] T. Heinze and S. Hamidi. "Heat transfer and parameterization in local thermal non-equilibrium for dual porosity continua". *Applied Thermal Engineering* 114 (2017), pp. 645–652. ISSN: 1359-4311. DOI: 10/f9xp2f (cit. on pp. 4, 52).

[26] F. Jiang, L. Luo, and J. Chen. "A novel three-dimensional transient model for subsurface heat exchange in enhanced geothermal systems". *International Communications in Heat and Mass Transfer* 41 (2013), pp. 57–62. ISSN: 0735-1933. DOI: 10/f4n9jk (cit. on p. 4).

[27] C. Xu and P. Dowd. "A new computer code for discrete fracture network modelling". *Computers & Geosciences* 36.3 (2010), pp. 292–301. ISSN: 0098-3004. DOI: 10/dz85h5 (cit. on p. 5).

[28] Q. Lei, J. P. Latham, and C. F. Tsang. "The use of discrete fracture networks for modelling coupled geomechanical and hydrological behaviour of fractured rocks". *Computers and Geotechnics* 85 (2017), pp. 151–176. ISSN: 0266-352X. DOI: 10/f96kj2 (cit. on p. 5).

[29] P. Moonen, L. J. Sluys, and J. Carmeliet. "A continuous–discontinuous approach to simulate physical degradation processes in porous media". *International Journal for Numerical Methods in Engineering* 84.9 (2010), pp. 1009–1037. ISSN: 1097-0207. DOI: 10/d8vhjq (cit. on p. 5).

[30] A. R. Shaik, S. S. Rahman, N. H. Tran, and T. Tran. "Numerical simulation of Fluid-Rock coupling heat transfer in naturally fractured geothermal system". *Applied Thermal Engineering* 31 (2011), pp. 1600–1606. DOI: 10/ck67j7 (cit. on pp. 5, 7, 20, 52, 60, 76, 77, 84, 85, 88, 89).

[31] O. Kolditz, S. Bauer, L. Bilke, N. Böttcher, J. O. Delfs, T. Fischer, U. J. Görke, T. Kalbacher, G. Kosakowski, C. I. McDermott, C. H. Perk, F. Radu, K. Rink, H. Shao, H. B. Shao, F. Sun, Y. Y. Sun, A. K. Singh, J. Taron, M. Walther, W. Wang, N. Watanabe, Y. Wu, M. Xie, W. Xu, and B. Zehner. "OpenGeoSys: an open-source initiative for numerical simulation of thermo-hydro-mechanical/chemical (THM/C) processes in porous media". *Environmental Earth Sciences* 67 (2012), pp. 589–599. DOI: 10/fxwmd6 (cit. on pp. 6, 52, 56, 57, 76).

[32] W. Wang, O. Kolditz, and T. Nagel. "A Parallel FEM Scheme for the Simulation of Large Scale Thermochemical Energy Storage with Complex Geometries using PETSc Routines". *Energy Procedia* 75 (2015). Clean, Efficient and Affordable Energy for a Sustainable Future: The 7th International Conference on Applied Energy (ICAE2015), pp. 2080–2086. ISSN: 1876-6102. DOI: 10/cc88 (cit. on p. 6).

[33] S. Balay, S. Abhyankar, M. F. Adams, J. Brown, P. Brune, K. Buschelman, L. Dalcin, V. Eijkhout, W. D. Gropp, D. Kaushik, M. G. Knepley, L. Curfman McInnes, K. Rupp, B. F. Smith, S. Zampini, H. Zhang, and H. Zhang. *PETSc Web page*. 2016. URL: www.mcs.anl.gov/petsc (cit. on p. 6).

[34] K. Pruess, C. M. Oldenburg, and G. J. Moridis. "Tough2 User's Guide Version 2" (1999) (cit. on p. 6).

[35] K. Pruess. "Enhanced geothermal systems (EGS) using {CO2} as working fluid—A novel approach for generating renewable energy with simultaneous sequestration of carbon". *Geothermics* 35.4 (2006), pp. 351–367. DOI: 10/d78hm2 (cit. on pp. 6, 76).

[36] J. Rutqvist. "Status of the TOUGH-FLAC simulator and recent applications related to coupled fluid flow and crustal deformations". *Computers and Geociences* 37 (2011), pp. 739–750. DOI: 10/bqdsmz (cit. on p. 6).

[37] T. Xu, E. Sonnenthal, N. Spycher, and K. Pruess. "TOUGHREACT- A simulation program for non-isothermal multiphase reactive geochemical transport in variably saturated geologic media: Applications to geothermal injectivity and CO_2 geological sequestration". *Computers and Geosciences* 32.2 (2006), pp. 145–146. DOI: 10/c7j7bq (cit. on pp. 6, 52, 76).

[38] T. Xu, N. Spycher, E. Sonnenthal, G. Zhang, L. Zheng, and K. Pruess. "TOUGHREACT version 2.0: A simulator for subsurface reactive transport under non-isothermal multiphase flow conditions". *Computers and Geosciences* 37.6 (2011), pp. 763–774. DOI: 10/bbp9k8 (cit. on p. 6).

[39] G. E. Hammond, P. C. Lichtner, C. Lu, and Mills R. T. "PFLOTRAN: Reactive flow and transport code for use on laptops to leadership-class supercomputers". *Groundwater Reactive Transport Models*. Ed. by Fan Zhang, G.T. Yeh, and Jack C. Parker. Sharjah, UAE: Bentham Science Publishers, 2012, pp. 141–159. DOI: 10/cc8v (cit. on p. 6).

[40] P. C. Lichtner, G. E. Hammond, C. Lu, S. Karra, G. Bisht, B. Andre, R. T. Mills, J. Kumar, and J. M. Frederick. *PFLOTRAN Web page*. 2017. URL: www.pflotran.org (cit. on p. 6).

[41] P. C. Lichtner, G. E. Hammond, C. Lu, S. Karra, G. Bisht, B. Andre, R. T. Mills, J. Kumar, and J. M. Frederick. *PFLOTRAN User Manual*. Tech. rep. 2017. URL: www.documentation.pflotran.org (cit. on p. 6).

[42] B. Flemisch, M. Darcis, K. Erbertseder, B. Faigle, A. Lauser, K. Mosthaf, S. Müthing, P. Nuske, A. Tatomir, M. Wolff, and R. Helmig. "DuMux: DUNE for multi-phase,component,scale,physics,... flow and transport in porous media". *Advances in Water Resources* 34.9 (2011). New Computational Methods and Software Tools, pp. 1102–1112. ISSN: 0309-1708. DOI: 10/bg8vj5 (cit. on p. 6).

[43] K. L. Jr. Kipp, P. A. Hsieh, and S. R. Charlton. *Guide to the revised ground-water flow and heat transport simulator: HYDROTHERM — Version 3*. Book 6, Chapter A25. U.S. Geological Survey Techniques and Methods. 2008. 160 pp. (cit. on p. 6).

[44] C. D. Langevin, D. T. Jr. Thorne, A. M. Dausman, M. C. Sukop, and W. Guo. *SEAWAT Version 4: A Computer Program for Simulation of Multi-Species Solute and Heat Transport*. Book 6, Chapter A22. U.S. Geological Survey Techniques and Methods. 2008. 39 pp. (cit. on p. 6).

[45] S. E. Ingebritsen, S. Geiger, S. Hurwitz, and T. Driesner. "Numerical simuation of magmatic hydrothermal systems". *Reviews of Geophysics* 47.2009 (2010), pp. 1–33. DOI: 10/bwjgm6 (cit. on p. 7).

[46] T. Driesner and C. A. Heinrich. "The system H_2O–NaCl. Part I: Correlation formulae for phase relations in temperature–pressure–composition space from 0 to 1000 °C, 0 to 5000 bar, and 0 to 1 X_{NaCl}". *Geochimica et Cosmochimica Acta* 71.20 (2007), pp. 4880–4901. DOI: 10/bkmbdv (cit. on p. 7).

[47] T. Driesner. "The system H_2O–NaCl. Part II: Correlations for molar volume, enthalpy, and isobaric heat capacity from 0 to 1000 °C, 1 to 5000 bar, and 0 to 1 X_{NaCl}". *Geochimica et Cosmochimica Acta* 71.20 (2007), pp. 4902–4919. DOI: 10/cpvgm5 (cit. on p. 7).

[48] M. G. Trefry and C. Muffels. "FEFLOW: A Finite-Element Ground Water Flow and Transport Modeling Tool". *Ground Water* 45.5 (2007), pp. 525–528. ISSN: 1745-6584. DOI: 10/dqm9mg (cit. on p. 7).

[49] C. Yu and C. Zheng. "HYDRUS: Software for Flow and Transport Modeling in Variably Saturated Media". *Ground Water* 48.6 (2010), pp. 787–791. ISSN: 1745-6584. DOI: 10/cjvkwp (cit. on p. 7).

[50] A. Amiri and K. Vafai. "Analysis of dispersion effects and non-thermal equilibrium, non-Darcian, variable porosity incompressible flow through porous media". *International Journal of Heat and Mass Transfer* 37.6 (1994), pp. 939–954. DOI: 10/fr74n5 (cit. on pp. 7, 52, 60, 68).

[51] W. J. Minkowycz, A. Haji-Sheikh, and K. Vafai. "On departure from local thermal equilibrium in porous media due to a rapidly changing heat source: the Sparrow number". *International Journal of Heat and Mass Transfer* 42.18 (1999), pp. 3373–3385. ISSN: 0017-9310. DOI: 10/cnbsjb (cit. on pp. 7, 20, 52).

[52] G. F. Al-Sumaily, H. M. Hussen, and M. C. Thompson. "Validation of thermal equilibrium assumption in free convection flow over a cylinder embedded in a packed bed". *International Communications in Heat and Mass Transfer* 58 (2014), pp. 184–192. ISSN: 0735-1933. DOI: 10/f6qvhb (cit. on pp. 7, 52, 88).

[53] H. Lu-Wu and J. Zhi-He. "Effects of local thermal non-equilibrium on the pore pressure and thermal stresses around a spherical cavity in a porous medium". *International Journal of Engineering Science* 49.3 (2011), pp. 240–252. ISSN: 0020-7225. DOI: 10/bnbsc2 (cit. on pp. 7, 52).

[54] R. H. Brooks and A. T. Corey. "Hydraulic Properties of Porous Media". *Hydrology Papers, Colorado State University* March (1964) (cit. on p. 15).

[55] M. Th. van Genuchten. "A closed-form equation for predicting the hydraulic conductivity of unsaturated soils". *Soil Science Society of America Journal* 44.5 (1980), pp. 892–898. DOI: 10/fdc8mc (cit. on pp. 15, 48).

[56] A. Szymkiewicz. "Mathematical Models of Flow in Porous Media". *Modelling Water Flow in Unsaturated Porous Media: Accounting for Nonlinear Permeability and Material Heterogeneity*. Berlin, Heidelberg: Springer Berlin Heidelberg, 2013, pp. 9–36. ISBN: 978-3-642-23559-. DOI: 10/cc85 (cit. on pp. 15, 48).

[57] S. C. Cropper, E. Perfect, E. H. van den Berg, and M. A. Mayes. "Comparison of Average and Point Capillary Pressure–Saturation Functions Determined by Steady-State Centrifugation". *Soil Science Society of America journal* 75.1 (2011). DOI: 10/dj38tr (cit. on p. 15).

[58] M. Tuller and D. Or. "Water Retention and Soil Water Characteristics Curve". *Encyclopedia of Soils in the Environment*. Elsevier Science, 2005, pp. 278–284 (cit. on pp. 15, 16).

[59] S. A. Bradford, L. M. Abriola, and F. J. Leij. "Wettability effects on two- and three-fluid relative permeabilities". *Journal of Contaminant Hydrology* 28.1 (1997), pp. 171–191. ISSN: 0169-7722. DOI: 10/btpcbr (cit. on p. 16).

[60] Y. Mualem. "A new model for predicting the hydraulic conductivity of unsaturated porous media". *Water Resources Research* 12.3 (1976), pp. 513–522. ISSN: 1944-7973. DOI: 10/bb7g6c (cit. on p. 16).

[61] N. T. Burdine. "Relative Permeability Calculations From Pore Size Distribution Data". *Journal of Petroleum Technology* 5 (1953). DOI: 10/cc8n (cit. on p. 16).

[62] L. A. Richards. "Capillary conduction of liquids through porous mediums". *Physics* 1.5 (1931), pp. 318–318. DOI: 10/ccmx4x (cit. on pp. 17, 48).

[63] J. P. Latham, J. Xiang, M. Belayneh, M. N. Hamidreza, C. F. Tsang, and M. J. Blunt. "Modelling stress-dependent permeability in fractured rock including effects of propagating and bending fractures". *Int J Rock Mech Min Sci* 57 (2013), pp. 100–112. DOI: 10/f3s9x3 (cit. on p. 17).

[64] K. B. Min, J. Rutqvist, C. F. Tsang, and L. Jing. "Stress-dependent permeability of fractured rock masses: a numerical study". *Int J Rock Mech Min Sci* 41 (2004), pp. 1191–1210. DOI: 10/bvv4hn (cit. on p. 17).

[65] J. J. Dong, J. Y. Hsu, W. J. Wu, T. Shimamoto, J. H. Hung, E. C. Yeh, Y. H. Wu, and H. Sone. "Stress-dependence of the permeability and porosity of sandstone and shale from TCDP Hole-A". *International Journal of Rock Mechanics and Mining Sciences* 47.7 (2010), pp. 1141–1157. DOI: 10/dmc55j (cit. on pp. 17, 36).

[66] Y. Shi and C. Y. Wang. "Pore pressure generation in sedimentary basins: Overloading versus aquathermal". *Journal of Geophysical Research: Solid Earth* 91.B2 (1986), pp. 2153–2162. ISSN: 2156-2202. DOI: 10/b4rrvh (cit. on pp. 17, 36).

[67] C. David, T. Fong Wong, W. Zhu, and J. Zhang. "Laboratory measurement of compaction-induced permeability change in porous rocks: Implications for the generation and maintenance of pore pressure excess in the crust". *Pure and Applied Geophysics PAGEOPH* 143.1-3 (1994), pp. 425–456. DOI: 10/fvjwr5 (cit. on pp. 17, 36).

[68] M. Lupi, S. Geiger, and C. M. Graham. "Numerical simulations of seismicity-induced fluid flow in the Tjörnes Fracture Zone, Iceland". *Journal of Geophysical Research: Solid Earth* 116.B7 (2011). B07101, n/a–n/a. ISSN: 2156-2202. DOI: 10/ff3gh4 (cit. on pp. 17, 36).

[69] J. Rutqvist, D. Barr, R. Datta, A. Gens, A. Millard, S. Olivella, C. F. Tsang, and Y. Tsang. "Coupled thermal–hydrological–mechanical analyses of the Yucca Mountain Drift Scale Test—Comparison of field measurements to predictions of four different numerical models". *International Journal of Rock Mechanics and Mining Sciences* 42.5-6 (2005), pp. 680–697. DOI: 10/cvn47j (cit. on pp. 17, 36).

[70] B. Figueiredo, C. F. Tsang, J. Rutqvist, and A. Niemi. "A study of changes in deep fractured rock permeability due to coupled hydro-mechanical effects". *International Journal of Rock Mechanics and Mining Sciences* 79 (2015), pp. 70–85. DOI: 10/f3pbzx (cit. on pp. 17, 36).

[71] F. Cappa and J. Rutqvist. "Modeling of coupled deformation and permeability evolution during fault reactivation induced by deep underground injection of CO_2". *International Journal of Greenhouse Gas Control* 5.2 (2011), pp. 336–346. ISSN: 1750-5836. DOI: 10/cwgqkw (cit. on pp. 17, 36).

[72] E. Aharonov, M. Spiegelman, and P. Kelemen. "Three-dimensional flow and reaction in porous media: Implications for the Earth's mantle and sedimentary basins". *Journal of Geophysical Research: Solid Earth* 102.B7 (1997), pp. 14821–14833. ISSN: 2156-2202. DOI: 10/bgr8kk (cit. on p. 18).

[73] O. Kolditz. *Computational Methods in enviromental Fluid Mechanics*. 1st. Springer, 2002 (cit. on pp. 18, 54).

[74] D. A. Nield and A. Bejan. *Convection in porous media*. Springer Science & Business Media, 2006, pp. 36–39 (cit. on pp. 19, 54, 58).

[75] A. G. Dixon and D. L. Cresswell. "Theoretical prediction of effective heat transfer parameters in packed beds". *AIChE Journal* 25.4 (1979), pp. 663–676. DOI: 10/dndwm7 (cit. on pp. 19, 54, 58).

[76] W.H. Press, B.P. Flannery, S.A. Teukolsky, and W.T. Vetterling. *Numerical Recipes in C: The Art of Scientific Computing, Second Edition*. 2nd ed. Cambridge University Press, 1992. ISBN: 0521431085 (cit. on p. 21).

[77] T. W. Becker and B. J. P. Kaus. *Numerical Modeling of Earth Systems. An introduction to computational methods with focus on solid Earth applications of continuum mechanics*. University of Southern California. Lecture notes (215 pages). 2013 (cit. on pp. 21, 22, 24).

[78] T. V. Gerya and D. A. Yuen. "Characteristics-based marker-in-cell method with conservative finite-differences schemes for modeling geological flows with strongly variable transport properties". *Physics of the Earth and Planetary Interiors* 140 (Dec. 2003), pp. 293–318. DOI: 10/fxgm6s (cit. on pp. 22, 23).

[79] S. I. Mayr, S. Stanchits, C. Langenbruch, G. Dresen, and S. A. Shapiro. "Acoustic emission induced by pore-pressure changes in sandstone samples". *Geophysics* 76.3 (2011), MA21–MA21. DOI: 10/bn6x4b (cit. on pp. 26, 35, 55).

[80] S. Stanchits, S. Mayr, S. Shapiro, and G. Dresen. "Fracturing of porous rock induced by fluid injection". *Tectonophysics* 503 (2011), pp. 129–145. DOI: 10/cg7wg6 (cit. on pp. 26, 28, 35, 55).

[81] J. Zhao and C. P. Tso. "Heat transfer by water flow in rock fractures and the application to hot dry rock geothermal systems". *International Journal of Rock Mechanics and Mining Science & Geomechanics* 30.6 (1993), pp. 633–41. DOI: 10/fnwmzh (cit. on pp. 26, 29, 54–57, 71, 76, 77, 79–81, 88, 89, 91).

[82] Z. Zhao. "On the heat transfer coefficient between rock fracture walls and flowing fluid". *Computers and Geotechnics* 59 (2014), pp. 105–111. ISSN: 0266-352X. DOI: 10/f5574z (cit. on pp. 26, 29, 54–56, 76–79, 81, 83, 85, 89, 91).

[83] A. Ogata and R. B. Banks. "A solution of the differential equation of longitudinal dispersion in porous media". *Geological Survey* 411-A (1961) (cit. on pp. 26, 30, 35, 56).

[84] M. J. Simpson and T. P. Clement. "Improving the worthiness of the Henry problem as a benchmark for density-dependent groundwater flow models". *Water Resources Research* 40 (2004). DOI: 10/bqkxpq (cit. on p. 28).

[85] P. Ackerer, A. Younes, and R. Mose. "Modeling Variable Density Flow and Solute Transport in Porous Medium: 1. Numerical Model and Verification". *Transport in Porous Media* 35.3 (1999), pp. 345–373. ISSN: 1573-1634. DOI: 10/cwsf79 (cit. on pp. 28, 29, 36).

[86] H. R. Henry. "Interferences between salt water and fresh water in coastal aquifers". *U.S. Geological Survey Water-Supply Paper 1613-C, Sea Water in Coastal Aquifers: C35–C70.* (1964) (cit. on p. 28).

[87] O. Kolitz, U. J. Görke, H. Shao, and W. Wang. *Thermo-Hydro-Mechanical-Chemical Processes in Fractured Porous Media*. Springer, 2012 (cit. on pp. 30–32).

[88] H. Sun, R. Feistel, M. Koch, and A. Markoe. "New equations for density, entropy, heat capacity, and potential temperature of a saline thermal fluid". *Deep-Sea Res I* 55 (2008), pp. 1304–10. DOI: 10/ftjxmf (cit. on pp. 32, 56, 66, 79).

[89] S. Hainzl, T. Fischer, and T. Dahm. "Seismicity-based estimation of the driving fluid pressure in the case of swarm activity in Western Bohemia". *Geophys J Int* 191.1 (Oct. 2012), pp. 271–281. ISSN: 0956540X. DOI: 10/f39rx6 (cit. on p. 34).

[90] M. C. Fehler. "Stress control of seismicity patterns observed during hydraulic fracturing experiments at the Fenton Hill hot dry rock geothermal energy site, New Mexico". *International Journal of Rock Mechanics and Mining Sciences & Geomechanics Abstracts* 26.3 (1989), pp. 211–219. ISSN: 0148-9062. DOI: 10/d47n2t (cit. on p. 34).

[91] S. Baisch and H. P. Harjes. "A model for fluid-injection-induced seismicity at the KTB, Germany". *Geophysical Journal International* 152.1 (2003), pp. 160–170. ISSN: 1365-246X. DOI: 10/fxfzfm (cit. on pp. 34, 87).

[92] J. Schmittbuhl, H. Karabulut, O. Lengliné, and M. Bouchon. "Seismicity distribution and locking depth along the Main Marmara Fault, Turkey". *Geochemistry, Geophysics, Geosystems* 17.3 (2016), pp. 954–965. ISSN: 1525-2027. DOI: 10/f8kfnd (cit. on p. 34).

[93] M. Lindenfeld, G. Rümpker, K. Link, D. Koehn, and A. Batte. "Fluid-triggered earthquake swarms in the Rwenzori region, East African Rift-Evidence for rift initiation". *Tectonophysics* 566–567 (2012), pp. 95–104. ISSN: 0040-1951. DOI: 10/cc82 (cit. on pp. 34, 46, 87).

[94] A. E. Croucher and M. J. O'Sullivan. "The Henry Problem for Saltwater Intrusion". *Water Resources Research* 31.7 (1995), pp. 1809–1814. ISSN: 1944-7973. DOI: 10/bs575k (cit. on pp. 35, 44, 45).

[95] O. Kolditz. "Modelling flow and heat transfer in fractured rocks: Conceptual model of a 3-D deterministic fracture network". *Geothermics* 24.3 (1995), pp. 451–470. DOI: 10/bpnhkd (cit. on p. 35).

[96] J. R. Rice. "Fault Stress States, Pore Pressure Distributions, and the Weakness of the San Andreas Fault". *Fault Mechanics and Transport Properties in Rocks*. 1992, pp. 475–503. DOI: 10/cn76n3 (cit. on p. 36).

[97] S. A. Shapiro and C. Dinske. "Fluid-induced seismicity: Pressure diffusion and hydraulic fracturing". *Geophysical Prospecting* 57.2 (2009), pp. 301–310. DOI: 10/cfw5tn (cit. on p. 36).

[98] S. A. Shapiro and Carsten Dinske. "Scaling of seismicity induced by nonlinear fluid-rock interaction". *Journal of Geophysical Research* 114.B9 (2009), B09307–B09307. DOI: 10/ccfnk2 (cit. on p. 36).

[99] P. Huyakorn and G. F. Pinder. "A pressure-enthalpy finite element model for simulating hydrothermal reservoirs". *Mathematics and Computers in Simulation* 20.3 (1978), pp. 167–178. DOI: 10/b64v3x (cit. on pp. 38, 66).

[100] T. Fischer, J. Horálek, P. Hrubcová, V. Vavryčuk, K. Bräuer, and H. Kämpf. "Intra-continental earthquake swarms in West-Bohemia and Vogtland: A review". *Tectonophysics* 611 (2014), pp. 1–27. ISSN: 00401951. DOI: 10/f5qvpk (cit. on p. 40).

[101] G. Chiodini, F. Frondini, C. Cardellini, D. Granieri, L. Marini, and G. Ventura. "CO_2 degassing and energy release at Solfatara volcano, Campi Flegrei, Italy". *Journal of Geophysical Research: Solid Earth* 106.B8 (2001), pp. 16213–16221. ISSN: 2156-2202. DOI: 10/bbgr6k (cit. on p. 46).

[102] J. Heinicke, T. Fischer, R. Gaupp, J. Götze, U. Koch, H. Konietzky, and K. P. Stanek. "Hydrothermal alteration as a trigger mechanism for earthquake swarms: the Vogtland/NW Bohemia region as a case study". *Geophysical Journal International* 178.1 (2009), pp. 1–13. DOI: 10/dhbjpp (cit. on p. 46).

[103] T. Terakawa, A. Zoporowski, B. Galvan, and S. A. Miller. "High-pressure fluid at hypocentral depths in the L'Aquila region inferred from earthquake focal mechanisms". *Geology* 38.11 (2010), pp. 995–998. DOI: 10/dp583r (cit. on p. 46).

[104] H. Zhao. *CO_2 Calculator, A web computational tool*. [accessed 11-September-2016]. URL: www.energy.psu.edu/tools/CO2-EOS/index.php (cit. on p. 47).

[105] M. Dendys, B. Tomaszewska, and L. Pająk. "Numerical modelling in research on geothermal systems". *Bulletin of Geography*. Physical Geography Series 9 (2016), pp. 39–44. DOI: 10/cc8q (cit. on p. 52).

[106] K. Jahan Bakhsh, M. Nakagawa, M. Arshad, and L. Dunnington. "Modeling Thermal Breakthrough in Sedimentary Geothermal System, Using COMSOL Multiphysics". *41st Workshop on Geothermal Reservoir Engineering*. 2016. DOI: 10/cc8z (cit. on p. 52).

[107] O. Kolditz and C. Clauser. "Numerical simulation of flow and heat transfer in fractured crystalline rocks: Application to the Hot Dry Rock site in Rosemanowes (U.K.)" *Geothermics* 27.1 (1998), pp. 1–23. DOI: 10/d8rg6r (cit. on pp. 52, 76).

[108] D. Šijačić and P.A. Fokker. "Thermo-Hydro-Mechanical modeling of EGS using COMSOL Multiphysics". *Fourtieth Workshop on Geothermal Reservoir Engineering*. 2015 (cit. on p. 52).

[109] F. Wellmann, A. Croucher, and K. Regenauer-Lieb. "Python scripting libraries for subsurface fluid and heat flow simulations with TOUGH2 and SHEMAT". *Computers & Geosciences* 43 (2012), pp. 197–206. ISSN: 0098-3004. DOI: 10/bz9fc3 (cit. on p. 52).

[110] R. Gelet, B. Loret, and N. Khalili. "A thermo-hydro-mechanical coupled model in local thermal non-equilibrium for fractured HDR reservoir with double porosity". *Journal of Geophysical Research: Solid Earth* 117.B7 (2012). DOI: 10/cc8t (cit. on p. 52).

[111] R. Gelet, B. Loret, and N. Khalili. "Thermal recovery from a fractured medium in local thermal non-equilibrium". *International Journal for Numerical and Analytical Methods in Geomechanics* 37.15 (2013), pp. 2471–2501. ISSN: 1096-9853. DOI: 10/f5bjzn (cit. on pp. 52, 88).

[112] T. Heinze, S. Hamidi, and B. Galvan. "A dynamic heat transfer coefficient between fractured rock and flowing fluid". *Geothermics* (2017), pp. 10–16. DOI: 10/f9g653 (cit. on pp. 54, 72).

[113] J. Zhao. "Geothermal testing and measurements of rock and rock fractures". *Geothermics* 23.3 (1994), pp. 215–231. DOI: 10/bqtn9r (cit. on p. 56).

[114] J. H. Schön. *Physical Properties of Rocks: A Workbook*. Elsevier, 2011, p. 46. DOI: 10/bn3pwh (cit. on pp. 58, 60).

[115] A. Amiri and K. Vafai. "Transient analysis of incompressible flow through a packed bed". *International Journal of Heat and Mass Transfer* 41.24 (1998), pp. 4259–4279. ISSN: 0017-9310. DOI: 10/dxrp7p (cit. on p. 60).

[116] J. Xu, B. Zhang, G. Cao, and H. Zhang. "Method for calculating the fracture porosity of tight-fracture reservoirs". *Geophysics* 81 (2016), pp. 57–70. DOI: 10/f88xmn (cit. on p. 63).

[117] J. F. Vernoux, A. Genter, P. h. Razin, and C. Vinchon. *Geological and petrophysical parameters of a deep fractured sandstone formation as applied to geothermal exploitation: EPS-1 borehole, Soultz-sous-Forêts, France*. Tech. rep. R 38622. BRGM, 1995 (cit. on p. 63).

[118] K. Pruess. "Numerical simulation of 'multiphase tracer transport in fractured geothermal reservoirs". *Geothermics* 31.4 (2002), pp. 475–499. ISSN: 0375-6505. DOI: 10/fxg27z (cit. on pp. 65, 76).

[119] K. Pruess. "On production behavior of enhanced geothermal systems with CO2 as working fluid". *Energy Conversion and Management* 49.6 (2008), pp. 1446–1454. ISSN: 0196-8904. DOI: 10/cpm5b4 (cit. on p. 65).

[120] H. G. Richards, R. H. Parker, A. S. P. Green, R. H. Jones, J. D. M. Nicholls, D. A. C. Nicol, M. M. Randall, S. Richards, R. C. Stewart, and J. Willis-Richards. "The performance and characteristics of the experimental hot dry rock geothermal reservoir at Rosemanowes, Cornwall (1985–1988)". *Geothermics* 23.2 (1994), pp. 73–109. ISSN: 0375-6505. DOI: 10/c2vwhk (cit. on pp. 68, 88).

[121] J. Rutqvist, L. Börgesson, M. Chijimatsu, A. Kobayashi, L. Jing, T. S. Nguyen, J. Noorishad, and C. F. Tsang. "Thermohydromechanics of partially saturated geological media: governing equations and formulation of four finite element models". *International Journal of Rock Mechanics and Mining Sciences* 38.1 (2001), pp. 105–127. DOI: 10/dqcw48 (cit. on p. 76).

[122] G. F. Al-Sumaily and M. C. Thompson. "Forced convection from a circular cylinder in pulsating flow with and without the presence of porous media". *Int J Heat Mass Transf* 61 (2013), pp. 226–244. DOI: 10/f4v7v6 (cit. on p. 76).

[123] D. A. Nield and A. Bejan. "Heat Transfer Through a Porous Medium". *Convection in Porous Media*. Ed. by D. A. Nield and A. Bejan. 4th. Springer, 2013. Chap. 2. ISBN: 978-1-4614-5540-0 (cit. on pp. 76, 77).

[124] A. J. Chapman. *Heat Transfer*. 4th. New York: Macmilan Publishing Company, 1989 (cit. on pp. 76, 89).

[125] A. G. Dixon. "Wall and Particle-shape effects on heat transfer in packed beds". *Chem Eng Comm* 71 (1988), pp. 217–237 (cit. on pp. 76, 77, 89).

[126] A. Staniforth and J. Cote. "Semi-Lagrangian Integration Schemes for Atmospheric Models—A Review". *Monthly Weather Review* 119.9 (1991), pp. 2206–2223. DOI: 10/d5n284 (cit. on pp. 77, 79).

[127] A. Quarteroni and A. Valli. *Numerical approximation of partial differential equations*. Springer Verlag, 1994 (cit. on p. 79).

[128] R. E. Ewing and H. Wang. "A summary of numerical methods for time- dependent advection-dominated partial differential equations". *J Comput Appl Math* 128 (2001), pp. 425–445 (cit. on p. 79).

[129] S. Luo, Z. Zhao, H. Peng, and H. Pu. "The role of fracture surface roughness in macroscopic fluid flow and heat transfer in fractured rocks". *Int J Rock Mech Min Sci* 87 (2016), pp. 29–38. ISSN: 1365-1609. DOI: 10/f8xvjn (cit. on p. 86).

[130] B. Galvan. "Modeling the spatio-temporal evolution of fracture networks and fuid-rock interactions in GPU: Applications to lithospheric geodynamics". Ph.D. Thesis. University of Bonn, Germany, 2012 (cit. on p. 90).

Acknowledgements

First of all, I would like to express my gratitude to my supervisor Prof. Dr. Stephen Miller for the interesting research project, inspiration and his support during my work. I am also very thankful to Prof. Dr. Andreas Kemna for his encouragement, helpful ideas and the opportunity he gave me to continue the path I had began. I appreciate Prof. Dr. Barbara Reichert and P.D. Dr. Elizabeth Soergel for joining the examination committee.

Furthermore, I appreciate the fruitful discussions, good comments and the guidance of Dr. Boris Galvan helping me throughout the project. Many special thanks to Dr. Thomas Heinze for being the best colleague ever, who comes with great ideas, is always available for discussion, helping and new challenges. I am thankful for the technical support of Dr. Andreas Dreist and administrative helps of Ms. Lisa Takacs.

I owe the nice working atmosphere to all my colleagues in the Geodynamics/Geophysics group of University of Bonn, especially Dr. Shiva Pudasaini, Sabine Undorf, Gunnar Jansen, Dr. Maximilian Weigand, Dr. Anna Zoporowski, Dr. Florian Wagner, Klaus Haaken, Dr. Johannes Kenkel, Dr. Florian Fuchs, Shari van Treeck, Jonas Limbrock and Astrid Matejcek. I thank Anna for helping with Tutorials and sharing her experiences generously.

I am very grateful to Marius Arenz for his constant helps in LaTeX and TikZ, smart suggestions about my work and specially for opening the doors of Linux and open-source world to me. I would like to extend my thanks to Dr. Ghazal Alipour, Zeinab Shafiee, Lisa Deter and Charly Arenz who encouraged me with their kindness throughout this time.

Last but not least, I am thankful for the love, patience and support of my dear parents Akram Rassaie and Hodjat Hamidi, my brother Hamed and my dear grandma Sayareh Heidari Saznaghi whom I have admired my whole life and to whom I owe who I am today.